LATVIAN JOURNAL of PHYSICS and TECHNICAL SCIENCES

ISSN 0868 - 8257

6

(Vol. 60)

2023

CONTENTS

LATVIAN JOURNAL of PHYSICS and TECHNICAL SCIENCES

LATVIJAS FIZIKAS un TEHNISKO ZINĀTŅU ŽURNĀLS

ЛАТВИЙСКИЙ ФИЗИКО-ТЕХНИЧЕСКИЙ ЖУРНАЛ

Published six times a year since February 1964
Iznāk sešas reizes gadā kopš 1964. gada februāra
Выходит шесть раз в год с февраля 1964 года

6 (Vol. 60) • 2023

RĪGA

INDEXED (PUBLISHED) IN

www.scopus.com
www.sciendo.com
EBSCO (Academic Search Complete, www.epnet.com), INSPEC (www.iee.org.com).
VINITI (www.viniti.ru), Begell House Inc/ (EDC, www.edata-center.com).

Issuers: Institute of Physical Energetics,
Institute of Solid State Physics, University of Latvia
Registration Certificate Number: 000700221

Editorial Contacts:
14 Dzerbenes Street, Riga, LV-1006
LATVIA
tel: +371 26245896
M: +371 29363105
leo@lza.lv

sciendo

LATVIAN JOURNAL OF PHYSICS
AND TECHNICAL SCIENCES
2023, N 6

DOI: 10.2478/lpts-2023-0033

NANOPORE FORMATION AT THE JUNCTIONS OF THE POLYCRYSTAL INTERGRANULAR BOUNDARY UNDER PLASTIC DEFORMATION

Y. Suchikova[1*], S. Kovachov[1], A. Lazarenko[1], I. Bohdanov[1], A. I. Popov[2*]

[1] Berdyansk State Pedagogical University,
71100 Berdyansk, UKRAINE
[2] Institute of Solid State Physics, University of Latvia,
8 Kengaraga Str., Riga, LV-1063, LATVIA
*e-mail: yanasuchikova@gmail.com, popov@latnet.lv

The article is devoted to the study of the mechanism of nanopore formation in the junctions of polycrystal grains under the plastic deformation of a polycrystal due to the conservative sliding of lattice dislocations. A mechanism for the formation of a stress concentrator at the junction of the polycrystal grain boundaries is proposed. The possibility of relaxation of the stress state due to the formation of a junction nanopore is considered in the paper.

Keywords: *Dislocation, grain boundaries, junction, nanopores, polycrystal, stress concentrators.*

1. INTRODUCTION

Porous semiconductors have been attracting the attention of researchers for more than half a century [1], [2]. They are widely used as: materials for solar panels [3], [4], sensors [5], [6], supercapacitors [7], [8]. Recently, interest in such semiconductors has increased due to the prospect of applying a porous layer as a buffer for growing thin films on a single-crystal substrate [9], [10]. Such a layer serves as a "soft cushion", allowing to reduce the stresses resulting from the inconsistency of the crystal lattices [11]. Porous layers are grown on the surface of single-crystal silicon [12], [13]. Thus, it was shown that the electrochemical treatment of single-crystal silicon in a solution of hydrofluoric acid makes it possible to form an array of cylindrical mutually parallel pores [14]. Often, A3B5 group semiconductors (InP, GaAs, GaP) serve as the basis for creating nanoporous layers [15]–[17]. The study [18]

presents a mechanism for the formation of domain pores on the surface of indium phosphide as a result of anode etching of a semiconductor. It is exhibited that the sliding of the pores can be caused by the crystal-lattice orientation of the surface. The authors of the work [19] have demonstrated the possibility of obtaining a developed porous morphology on InP p-type by vapour-phase etching with two halogen acids (HF and HCl). As a result, it was found that halogen acid vapours (especially HCl) affect the thermal properties of the semiconductor. In the research [20], the correlations between the current density of the semiconductors anodizing and the morphological characteristics of the formed nanostructures were investigated. It was concluded that various semiconductors under the same conditions of electrochemical processing demonstrated different pore formation abilities. For the formation of such porous surfaces, as a rule, high-quality single-crystalline material is used [21], [22]. Among the most common methods for forming porous layers are electrochemical etching [23], photoelectrochemical etching [24], and photolithography [25]. All these methods are aimed at artificially creating pores in a homogeneous material [26]. Such modified surfaces and volumes acquire a number of non-standard properties distinguishing porous layers from their crystalline counterparts. First, there is a fundamental increase in the effective surface area, which can be successfully used in photovoltaics (PV) [27]. Secondly, there is a change in the indexes of reflection and absorption of light, which has found its application in photovoltaic energy converters [28]. In addition, the fact of reducing the mass of the crystalline material is interesting and may contribute to the creation of lightweight crystals [29]. In addition to these features, it is also necessary to acknowledge the reduction of internal stresses of the material due to the release of dislocations through an open pore [30], [31].

Apart from the artificial introduction of pores into a crystalline material, a spontaneous pore formation may take place [32], [33]. In particular, pores can form at the junctions of polycrystal grains [34], [35]. This sphere of study is quite interesting from the point of view of using cheaper analogues of porous single crystals. It is commonly known that growing a single crystal with subsequent surface modification is a very high-tech technology requiring huge resources, modern equipment and high costs [36]. Polycrystalline materials are much easier to grow [37]. To optimize the mechanical properties of alloys, grain size and texture are often manipulated by thermomechanical processing, including deformation and annealing [38]. The question of the mechanisms of pore self-organization in the volume of such semiconductors, their concentration and size remains not fully resolved. The proposed study focuses on modelling the process of the appearance of the pores in places of stress concentration at the junctions of the polycrystal grain boundaries.

2. PROBLEM STATEMENT

The main feature of the polycrystal structure in comparison with single crystals and amorphous solids is the presence of two-dimensional defects, namely, grain boundaries. Grain boundaries are the surfaces on which the differences in the orientation of the crystal planes of adjacent single-crystal grains of polycrystals are matched. In most polycrystalline structures, excluding “bamboo” polycrystals, grain boundaries intersect

to form triple junctions (TJs). TJs are linear defects along which the differences of the grain boundaries are consistent.

This alignment occurs mainly due to local transformations or violations of the ideal crystal structure and the redistribution of such dynamic defects as vacancies and dislocations under the influence of various external factors (temperature gradients, force fields, mechanical loads).

One of the most important consequences of the matching processes occurring at the grain boundaries and junctions is the formation of stress concentrators of various types. Among them, we can distinguish concentrators of a diffusive, dislocation, and disclination nature [39], [40]. A dislocation-type concentrator is a dislocation that takes place at the junction of grain boundaries. The junction dislocation is an analogue of the lattice dislocation, but it is considered not as a part of the crystal lattice of an individual grain, but in conditional (virtual) constructs: the lattice of grain boundary shifts, the complete lattice of overlaps, and the lattice of coincident nodes of crystal grains forming the junction [41], [42]. Such concentrators play a defining role in the further evolution of the polycrystal, being responsible for local accommodation processes. In the junctions of the grain boundaries, the processes of plastic deformation of polycrystals are coordinated. If it is impossible to relax the dislocation-type junction stress concentrator, the plastic deformation process slows down or undergoes qualitative changes. The relaxation of the junction concentrator can be carried out due to local accommodation in the near-junction region of the polycrystal, or due to the pore formation.

A dislocation-type concentrator, as a rule, occurs in junctions formed by special grain boundaries as a result of the interaction of dislocations entering the junction along the grain boundaries.

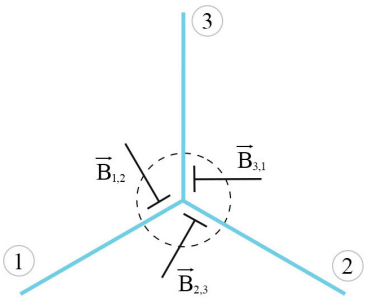

Fig. 1. A model of a junction dislocation with the Burgers vector $\vec{B} = \vec{B}_{1,2} + \vec{B}_{1,3} + \vec{B}_{3,2}$, formed as a result of matching grain boundary shifts $\vec{B}_{1,2}; \vec{B}_{1,3}; \vec{B}_{3,2}$ - Burgers vectors of grain boundary dislocations.

The operating conditions of polycrystalline materials imply the inevitable occurrence of internal stresses, both due to purely mechanical loading and as a result of the influence of temperature gradients and external force fields. Let us consider the most basic case of mechanical loading, which, in general, does not limit the comprehensiveness of the result.

If an external mechanical load is applied to a polycrystal, ensuring that the Peierls barrier is overcome by lattice dislocations (LD), then a conservative movement (sliding) of dislocations becomes possible in the grain volume. Obviously, this sliding is limited by the volume of the grain itself and stops at its boundaries.

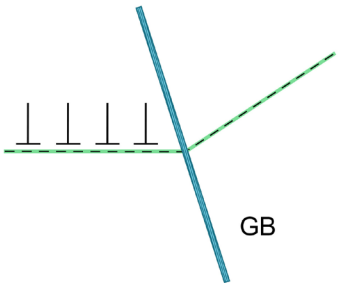

Fig. 2. Formation of a cluster of parallel dislocations inhibited by the boundary of polycrystal grains in the sliding plane.

The lattice dislocation slows down before the grain boundaries and stops moving. However, there might be several LD in this sliding plane meaning that there is a Frank-Reed type dislocation source. It is a segment of the dislocation line, the ends of which are fixed to any obstacles to the conservative sliding of the dislocation, for example, inclusions, complexes of point defects, a grid of dislocations, pores. Under the influence of an external force, the segment continues to slide conservatively, remaining fixed at the ends. As a result, dislocation loops are formed. The peculiarity of the Frank-Reed source is that it is not disposable – after the formation of a loop, it restores its original form and is triggered again. A cluster of identical dislocations (with the same Burgers vectors and the same line directions) is formed in front of the grain boundaries (GB). These dislocations repel each other in the sliding plane. In the equilibrium distribution (stationary position) they are held by an external mechanical load.

The parameters of the equilibrium distribution of dislocations in the continuum approximation depend on the Burgers vector of dislocations, the elastic modules of the sample, and are determined by the dependencies [44]:

$$\rho(\chi) = \frac{\sigma_0}{\pi D}\sqrt{\frac{1-\chi}{\chi}} \; ; \quad l = \frac{2BD}{\sigma_0} \; , \qquad (1)$$

where $\rho(\chi)$ – the linear dislocation density $\rho(\chi)d\chi$ is the sum of the Burgers vectors of dislocations that fall on the linear differential spatial interval $d\chi$;

σ_0 – a flat uniform field of mechanical stresses of external origin caused by an external force (displacement, compression, tension) applied to the outer surface of a polycrystal;

l – the length of the interval of arrangement of clusters of lattice dislocations;

χ – the distance from the grain boundary in the plane of conservative dislocation plane;

B – the sum of the Burgers vectors of all dislocations in the cluster;

$D = \frac{\mu}{2\pi(1-\nu)}$ – an index implemented for the convenience of writing formulas;

μ – the displacement modulus of the sample material;

ν – Poisson's ratio of the sample material.

In this case, before the dislocation, which has gone into the grain boundary, mechanical stresses are concentrated according to the law:

$$\sigma(\chi) = \sigma_0\sqrt{\frac{l}{\chi}} \, . \qquad (2)$$

Given that the distance to the next dislocation is equal to the width of the grain boundary $\chi = \delta$, and using (1) and (2), it becomes possible to estimate the stress concentration directly beyond the grain boundary:

$$\sigma(\delta) = \left(2\sigma_0 D\frac{B}{\delta}\right)^{\frac{1}{2}} \, , \qquad (3)$$

where δ – the width of the grain boundary.

The displacement modulus μ, (respectively, and the index D) far exceed the value of their own mechanical load σ_0. The total Burgers vector of cluster B is at least equal to the width of the grain boundary δ. Accordingly, the stress concentration (3) will be sufficient for the dislocation shift to pass through the boundary into the adjacent grain. In this case, a dislocation of the orientation mismatch (DOM) is formed at the grain boundary (Fig. 3).

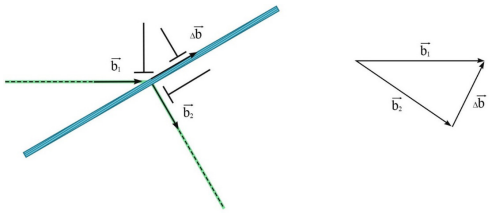

Fig. 3. The scheme of the lattice dislocation passing through the grain boundary with the formation of an orientation mismatch dislocation.

The Burgers vector is determined based on the condition of preserving the total Burgers vector in dislocation reactions:

$$\overline{b}_1 = \overline{b}_2 + \Delta\overline{b}\,;\ \Delta b = \overline{b}_1 - \overline{b}_2\ , \qquad (4)$$

where $\overrightarrow{b_1}$ – the Burgers vector of the LD in the first grain (before passing through the grain boundary);

$\overrightarrow{b_2}$ – the Burgers vector of the LD in the second grain (after passing through the grain boundary);

$\Delta\vec{b}$ – the Burgers vector at the dislocation of the orientation mismatch.

It can be concluded that the concentration of stresses from the accumulation of parallel lattice dislocations, inhibited by the boundary of adjacent grains in the sliding plane, is able to ensure the propagation of the dislocation shift from one grain of a polycrystal to the adjacent one. In this case, the sliding planes of dislocations in adjacent grains should not be parallel. Matching the transition of the lattice dislocation from one sliding plane to another leads to the formation of a grain-boundary dislocation of the orientation mismatch.

3. MECHANISM OF PORE FORMATION IN THIN POLYCRYSTALS

Consider a situation where the structure of the grain boundary is ordered. Also, let us assume that the movement of the dislocation of the orientation mismatch in the grain boundary plane occurs mainly due to sliding. The assumption seems reasonable due to the fact that the propagation of the dislocation shift into the adjacent grain will preferably occur through such a grain boundary, where the rapid departure of the dislocation of the orientation mismatch from the place of agreement of the dislocation shifts will ensure a decrease in the stress concentration.

For a fine-grained polycrystal with a "parquet" structure, the grain boundary can be considered flat. Figure 4 allows determining the directions of the sliding planes in adjacent grains, which provide the possibility of conservative sliding of the dislocation of the orientation mismatch. In this case, the dislocation line and its Burgers vector lie in the grain boundary plane.

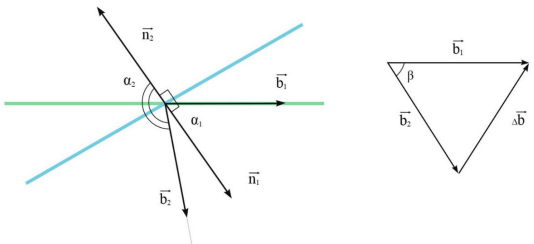

Fig. 4. Scheme for calculating the Burgers vector at dislocation of the orientation mismatch $\Delta\vec{b}$: $\overrightarrow{n_1}$ – unit normal to the grain surface 1; $\overrightarrow{n_2}$ – unit normal to the grain surface 2; α_1 – the angle between the vectors $\vec{b}_1$ and $\overrightarrow{n_1}$; α_1 – the angle between the vectors $\vec{b}_2$ and $\overrightarrow{n_2}$; β – the angle between the vectors $\vec{b}_1$ and $\overrightarrow{b_2}$ i.

Respectively, in Fig. 4, the angle between the Burgers vectors of dislocations in the first and second grain is equal to:

$$\beta = \begin{cases} \pi - (\alpha_2 - \alpha_1), & \text{if } \vec{b}_1 \text{ i } \vec{b}_2 \text{ located on different sides of the normals line;} \\ \pi - (\alpha_2 + \alpha_1), & \text{if } \vec{b}_1 \text{ i } \vec{b}_2 \text{ located on the dislocation of the orientation} \\ & \text{mismatch side of the normals line;} \end{cases} \quad (5)$$

where β – the angle between the vectors $\vec{b}_1$ and $\vec{b}_2$;
α_1 – the angle between the vectors $\vec{b_1}$ and the unit normal to the grain boundary 1;
α_2 – the angle between the vectors $\vec{b_2}$ and the unit normal to the grain boundary 2.

It should be taken into account that the normal has an external direction in relation to the grain volume. It also follows from Fig. 4 that the Burgers vector at dislocation of the orientation mismatch lies in the plane of the grain boundary if the angle between it and the Burgers vector LD of the first grain is equal to $(\pi/2 - a_1)$ or $(\pi/2 + a_1)$. This condition is met if:

$$\cos(\overline{b_1}^{\wedge}, \Delta\bar{b}) = \begin{cases} \cos(\frac{\pi}{2} - \alpha_1) \\ \cos(\frac{\pi}{2} + \alpha_2) \end{cases} = \begin{cases} \sin\alpha_1 \\ -\sin\alpha_1 \end{cases}, \quad (6)$$

$$\cos\beta = \begin{cases} \cos(\pi - (\alpha_2 - \alpha_1)) = -\cos(\alpha_2 - \alpha_1) \\ \cos(\pi - (\alpha_2 + \alpha_1)) = -\cos(\alpha_2 + \alpha_1) \end{cases}, \quad (7)$$

$$\Delta b = (b_1^2 + b_2^2 - 2b_1 b_2 \cos\beta)^{\frac{1}{2}}. \quad (8)$$

The obtained relations (9) are geometric criteria. When one of them is met, the dislocation of the orientation mismatch line and its Burgers vector lie in the grain boundary plane. Such placement will provide the possibility of conservative sliding of the dislocation of the orientation mismatch in the plane of the grain boundary.

A more detailed analysis of the conditions (9) is quite complex. It requires a rigorous description of the crystal structure, along with the use of statistical and probabilistic approaches. However, for a general understanding of the process of matching dislocation shifts in the grain boundary, it is sufficient for each specific set of values of the Burgers vectors and angles to check whether at least one of these equalities is true or not.

As an example of the application of the obtained conditions, we can consider the simplest case when the modules of the Burgers vectors of both lattice dislocations and dislocation of the orientation mismatch coincide. This means that the triangle in Fig. 2 will be equilateral. Then, according

to (7), either the sum or the difference α_1 and α_2 must be equal to $2\pi/3$.

Thus, if the dislocation reaction (4) satisfies one of the equalities (9), a dislocation of the orientation mismatch is formed at the grain boundary, which is capable of conservative movement along the grain boundary.

The dislocation reaction (4), the passage of the LD through the grain boundary, and the formation of the dislocation of the orientation mismatch occur due to the concentration of stresses from the accumulation of parallel LD, inhibited in the same sliding plane in front of the grain boundary. The source that supplies the dislocations for the cluster continues to operate. As a result, the level of stress concentration in the head of the cluster is restored. The dislocation that has passed the grain boundary moves away from it deeper into the volume, and the dislocation of the orientation mismatch moves away from the place of its formation along the grain boundary at their junction.

The dislocation reaction (4) is repeated periodically, and a "torch" of the LD is formed in the adjacent grain, which spreads from the grain boundary. Inside the grain boundary itself, a cluster of dislocation of the orientation mismatch is formed, the movement of which is limited by the triple junction (TJ) of the grain boundary.

The triple junction of the grain boundaries of polycrystals is formed as a result of the intersection of three-grain boundary planes along a specific linear defect - the TJ grain boundary channel. Schematically, the TJ is shown in Fig. 5.

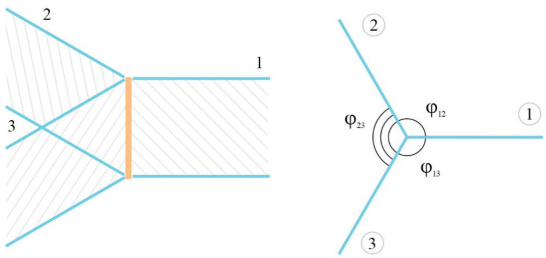

a) b)

Fig. 5. Schematic representation of the triple junction of grain boundaries: a) a spatial view for the case of a "parquet" polycrystal; b) a top view; φ_{12} φ_{13} φ_{23} angles between the grain boundary planes.

When the conditions (8) are met, dislocation of the orientation mismatch appears in the boundaries that form the junction. They can move conservatively along the grain boundary planes. When they reach the TJ, dislocation of the orientation mismatch interacts and forms a junction dislocation. This junction dislocation becomes a stress concentrator as the dislocation of the orientation mismatch accumulates at the grain boundaries.

It is possible that the Burgers vectors do not correspond to the condition:

$$\Delta\overline{b_1} + \Delta\overline{b_2} + \Delta\overline{b_3} = 0\,, \qquad (9)$$

where $\Delta\vec{b_1}$ $\Delta\vec{b_2}$ $\Delta\vec{b_3}$ - the Burgers vectors of dislocation of the orientation mismatch are located in the boundaries 1, 2, 3, respectively.

The vector condition (10) can be written as two scalar conditions (Fig. 3b):

$$\pm\Delta b_1 \pm \Delta b_2 \cos\varphi_{12} \pm \Delta b_3 \cos\varphi_{13} = 0\,;\ \pm\Delta b_2 \sin\varphi_{12} - (\pm\Delta b_3 \sin\varphi_{13}) = 0\,. \qquad (10)$$

The "+" sign before the module of the Burgers vector is selected if this vector is directed to the junction; the "–" sign is selected if the Burgers vector of dislocation of the orientation mismatch is directed from the junction.

Junctions that simultaneously meet the conditions (8) and (9) or (10) manifest themselves as effective dislocation of the orientation mismatch drains. Stress concentrators do not form in them. Junctions of this type could play a special role in the processes of plastic deformation of polycrystals, and a polycrystal with an increased density of junction drains for the dislocation of the orientation mismatch should have plastic properties that differ from the average ones. However, in a natural polycrystal, the relative amount of dislocation of the orientation mismatch of junction drains will be negligible.

From the most general considerations, based on Newton's third law, it can be understood that the maximum level of stress concentration in the junction concentrator cannot exceed the maximum level of concentration in the head of the dislocation cluster, which is inhibited by the grain boundary. When the stress concentration levels in the junction and the head of the dislocation cluster are equalized, the process of dislocation shift passing from grain to grain will stop. The resumption of this process will be possible only after the relaxation of the junction stress concentrator.

The relaxation of the junction concentrator can be carried out due to various mechanisms of local plastic deformation, such as: formation of "torches" of dislocation loops, plastic rotations, local migration, etc. [45].

Let us consider the possibility of relaxation of the junction dislocation concentrator due to the formation of a junction pore.

The components of the stress tensor caused by the junction dislocation concentrator for the case of a "parquet" polycrystal are defined as [44]:

$$\sigma_{\rho\rho} = \sigma_{\varphi\varphi} = -\Delta BD\frac{\sin\varphi}{\rho}\ ;\ \sigma_{\rho\varphi} = \Delta BD\frac{\cos\varphi}{\rho}\ , \qquad (11)$$

where ΔB – Burgers vector of junction dislocation; $D = \dfrac{\mu}{2\pi(1-\nu)}$; μ – shift of material; ν – Poisson's ratio of the substance; (ρ,φ) - polar coordinates with the pole at the grain junction.

The value ΔB it can be estimated using the condition of equality of the stress concentration in the head of the dislocation cluster at the grain boundary and the stress concentration in the junction concentrator using expressions (3) and (11).

$$\frac{\Delta BD}{\delta} \approx \pm\left(2\sigma_0 D\frac{B}{\delta}\right)^{\frac{1}{2}};\ \ \Delta B \approx \pm\left(2\delta B\frac{\sigma_0}{D}\right)^{\frac{1}{2}}. \qquad (12)$$

If we take $l \approx d$, where d is the characteristic grain size of a polycrystal (the case of a fine-grained crystal):

$$B = \frac{1}{2}\frac{\sigma_0}{D} d \,. \tag{13}$$

Substituting (12) in (13) we get:

$$\Delta B \approx \pm \frac{\sigma_0}{D} (\delta d)^{\frac{1}{2}} \,. \tag{14}$$

Substituting (14) in (11) we get:

$$\sigma_{\rho\rho} = \sigma_{\varphi\varphi} \approx \pm \sigma_0 (\delta d)^{\frac{1}{2}} \frac{\sin\varphi}{\rho};$$

$$\sigma_{\rho\varphi} \approx \sigma_0 (\delta d)^{\frac{1}{2}} \frac{\cos\varphi}{\rho}. \tag{15}$$

According to (16), a junction dislocation with a positive Burgers vector ΔB (which corresponds to an excessive extra plane) causes mechanical compression stresses in the direction perpendicular to the grain boundaries. This leads to a negative oversaturation of vacancies in the local areas of grain boundaries near their TJ [46]:

$$c = c_0 \exp\left(\frac{\sigma_{nn}\omega_0}{kT}\right), \tag{16}$$

where $\sigma_{nn} = \sigma_{ik} n_i n_k$ – the normal mechanical stresses at the grain boundaries; σ_{ik} – components of the stress tensor; n_i, n_k – the components of the vector of the external normal to the surface; c_0 – the equilibrium concentration of vacancies in the grain boundary at the absolute temperature T; k – the Boltzmann constant; ω_0 – the vacancy volume.

In the approximation of small loads ($\sigma_0 \ll \mu$):

$$c(\rho,\varphi) = c_0 \left(1 - \frac{\sigma_0 (\delta d)^{\frac{1}{2}} \omega_0}{kT} \frac{\sin\varphi}{\rho}\right). \tag{17}$$

The nonequilibrium distribution of the vacancy concentration will cause a diffuse outflow of the substance from the TJ channel:

$$\frac{\Delta V}{\Delta t} = -I \delta d b^3 \,, \tag{18}$$

where I – the flow of vacancies to the TJ; δ – grain boundary width; d – characteristic grain size of a polycrystal; b^3 –volume of the atom; ΔV– the volume of the substance removed from the TJ channel during the time Δt.

The vacancy flow I is calculated according to the diffusion equation:

$$I = -D_{M3} grad(c), \tag{19}$$

where D_{M3} – the diffusion coefficient across the grain boundaries.

Estimating the gradient of the vacancy concentration as the difference between its values at a distance from the junction and near it, we obtain:

$$I \approx -D_{M3} \frac{1}{d} c_0 \frac{\sigma_0 \omega_0}{kT} \left[\left(\frac{d}{\delta}\right)^{\frac{1}{2}} - \left(\frac{\delta}{d}\right)^{\frac{1}{2}} \right]. \tag{20}$$

Since the width of the grain, boundary δ is much smaller than the characteristic grain size d, and the vacancy size is close to the atomic volume b^3, the expression (20) can be written in a simplified form:

$$\frac{\Delta V}{\Delta t} \approx D_{M3} c_0 b^3 (\delta d)^{\frac{1}{2}} \frac{\sigma_0 b^3}{kT} \,. \tag{21}$$

Thus, diffusive mass transfer across grain boundaries can provide the formation of a junction pore if it provides partial or complete relaxation of the junction concentrator.

Partial relaxation of the junction stress concentrator will occur if the energy associated with the pore is less than the energy of the dislocation concentrator.

The energy of a dislocation concentrator is the energy of its stress fields. It can be estimated by the expression (6), which takes into account the contribution of the energy of the dislocation core:

$$W_D = d\frac{\mu\Delta B^2}{4\pi(1-\nu)}\ln\frac{4d}{\Delta B}. \qquad (22)$$

Given that $D = \frac{\mu}{2\pi(1-\nu)}$, we get:

$$W_D = \frac{\delta(d\sigma_0)^2}{2D}\ln\left(4\frac{D}{\sigma_0}\left(\frac{d}{\delta}\right)^{\frac{1}{2}}\right). \qquad (23)$$

We will estimate the pore energy as a function of its radius. The pore energy consists of the elastic strain energy due to the pore and the surface energy of the pore itself.

The junction pore in the first approximation is a hole in the form of a round cylinder, which leads to a geometric stress concentration in its vicinity. The corresponding components of the stress and strain tensors in solving the plane problem of the theory of elasticity ("parquet" polycrystal) in polar coordinates according to [44] have the form:

$$\sigma_{\rho\rho} = \frac{1}{2}\sigma_0\left(1-\frac{\alpha^2}{\rho^2}\right)+\frac{1}{2}\sigma_0\left(1-4\frac{\alpha^2}{\rho^2}+3\frac{\alpha^4}{\rho^4}\right)\cos 2\varphi,$$

$$\sigma_{\varphi\varphi} = \frac{1}{2}\sigma_0\left(1+\frac{\alpha^2}{\rho^2}\right)-\frac{1}{2}\sigma_0\left(1+3\frac{\alpha^4}{\rho^4}\right)\cos 2\varphi,$$

$$\sigma_{\rho\varphi} = -\frac{1}{2}\sigma_0\left(1+2\frac{\alpha^2}{\rho^2}-3\frac{\alpha^4}{\rho^4}\right)\sin 2\varphi,$$

where a – the radius of the pore.

To obtain the components of the strain tensor, we use the relation:

$$U_{ik} = \frac{1}{9K}\delta_{ik}\sigma_{ll}+\frac{1}{2\mu}\left(\sigma_{ik}-\frac{1}{3}\delta_{ik}\sigma_{ll}\right), \qquad (24)$$

where $\boldsymbol{K}$ – is the all-round compression modulus; $\boldsymbol{\mu}$ is the displacement modulus; $\delta_{ik} = \begin{cases}1, i = k\\ 0, i \neq k\end{cases}$

Using the relation between $\boldsymbol{K}$ and the Lame coefficients $\boldsymbol{\lambda}$, $\boldsymbol{\mu}$, we simplify the expression (24)

$$U_k = \frac{1}{2\mu}\left(\sigma_{ik}-\frac{2-5\nu}{9(1+\nu)}\delta_{ik}\sigma_{ll}\right). \qquad (25)$$

We will find σ_{ll}:

$$\sigma_{ll} = \sigma_{\rho\rho}+\sigma_{\varphi\varphi} = \sigma_0 - 2\sigma_0\frac{a^2}{\rho^2}\cos 2\varphi$$

Then the components of the strain tensor U_{ik}:

$$U_{\rho\rho} = \frac{1}{4}\frac{\sigma_0}{\mu}\left[\frac{5-\nu}{9(1+\nu)}-\frac{\alpha^2}{\rho^2}+\left(1-\frac{4(7+4\nu)}{9(1+\nu)}\frac{\alpha^2}{\rho^2}+3\frac{\alpha^4}{\rho^4}\right)\cos 2\varphi\right],$$

$$U_{\varphi\varphi} = \frac{1}{4}\frac{\sigma_0}{\mu}\left[\frac{5-\nu}{9(1+\nu)} + \frac{\alpha^2}{\rho^2} - \left(1 - \frac{4(2+5\nu)}{9(1+\nu)}\frac{\alpha^2}{\rho^2} + 3\frac{\alpha^4}{\rho^4}\right)\cos 2\varphi\right],$$

$$U_{\rho\varphi} = U_{\varphi\rho} = -\frac{1}{4}\frac{\sigma_0}{\mu}\left(1 + 2\frac{\alpha^2}{\rho^2} - 3\frac{\alpha^4}{\rho^4}\right)\sin 2\varphi\,. \qquad (26)$$

The volume density of the free energy of a deformed body is defined as [44]:

$$F = \frac{\sigma_{ik}u_{ik}}{2}, \qquad (27)$$

Here, Einstein's rule of addition over even indices is used.

Substituting (27) and (30) in (31) we get:

$$F = \frac{1}{8}\frac{\sigma^2{}_0}{\mu}\left[1 - \frac{\alpha^2}{\rho^2} + \left(1 - 4\frac{a^2}{\rho^2} + 3\frac{\alpha^4}{\rho^4}\right)\cos 2\varphi\right]\cdot \qquad (28)$$

To obtain the energy of the deformed state, it is necessary to calculate the integral:

$$W = d\int_a^d\int_0^{2\pi} F(\rho,\varphi)\rho d\rho d\varphi\,. \qquad (29)$$

Accordingly, all the components of the expression for the free energy density F that have a multiplier of $\cos 2\varphi$, or $\sin 2\varphi$ after integration by $d\varphi$, in the range from 0 to 2π are zeroed. Therefore, to calculate the energy, we can use a much-simplified expression instead:

$$F^{"} = \frac{1}{4}\frac{\sigma_0^2}{\mu}\left[\frac{2(7+4\nu)}{9(1+\nu)} + \frac{55+43\nu}{9(1+\nu)}\frac{\alpha^4}{\rho^4} - 12\frac{\alpha^6}{\rho^6} + 9\frac{\alpha^8}{\rho^8}\right]. \qquad (30)$$

Taking $a \approx d$, we simplify:

$$W_1 = \frac{\pi}{2}\frac{\sigma_0^2}{\mu}d\frac{7+4\nu}{9(1+\nu)}\left(d^2 + a^2\right). \qquad (31)$$

The surface energy of the pore can be calculated as:

$$W_2 = \gamma S\,, \qquad (32)$$

where γ – the surface energy density; S – the free surface area of the junction pore $S = 2\pi ad$.

Accordingly, to [47] $\gamma \approx 0{,}1\mu b$. Then we get: $W_2 \approx 0{,}2\mu\pi abd$

Thus, the excess energy of the polycrystal associated with the occurrence of the junction pore is estimated as:

$$W_{\check{I}} = W_1 + W_2\,,$$

$$W_{\check{I}} = 0{,}2\mu\pi abd\left[1 + \frac{\sigma_0^2}{\mu^2}\frac{d}{b}\frac{7+4\nu}{3{,}6(1+\nu)}\left(\frac{d}{a} + \frac{a}{d}\right)\right]. \qquad (33)$$

Comparing (26) and (39), we obtain a criterion for the occurrence of a junction pore instead of a dislocation-type junction stress concentrator, as a condition for reducing the energy of the deformed state:

$$W_{\ddot{I}} < W_{\ddot{A}},$$

$$0,2\mu\pi abd\left[1+\frac{\sigma_0^2}{\mu^2}\frac{d}{b}\frac{7+4\nu}{3,6(1+\nu)}\left(\frac{d}{a}+\frac{a}{d}\right)\right]\langle\frac{\delta(d\sigma_0)^2}{2D}\ln\left[4\frac{D}{\sigma_0}\left(\frac{d}{\delta}\right)^{\frac{1}{2}}\right],$$

given that $D=\frac{\mu}{2\pi(1-\nu)}$:

$$a\left[1+\frac{\sigma_0^2}{\mu^2}\frac{d}{b}\frac{7+4\nu}{3,6(1+\nu)}\left(\frac{d}{a}+\frac{a}{d}\right)\right]\langle 5(1-\nu)\delta\frac{d}{b}\frac{\sigma_0^2}{\mu^2}\ln\left[\frac{2}{\pi(1-\nu)}\frac{\mu}{\sigma_0}\left(\frac{d}{\delta}\right)^{\frac{1}{2}}\right]. \quad (34)$$

For the case of $\left(\frac{\sigma_0}{\mu}\right)^2\frac{d}{ab}\approx 1$, the gap resulting from the relaxation of a dislocation-type junction stress concentrator cannot exceed a certain critical size, which, in the continuum approximation, corresponds to its geometric radius:

$$a_{\hat{e}\delta}=5(1-\nu)\delta\frac{d}{b}\left(\frac{\sigma_0}{\mu}\right)^2\ln\left[\frac{2}{\pi(1-\nu)}\frac{\mu}{\sigma_0}\left(\frac{d}{\delta}\right)^{\frac{1}{2}}\right]. \quad (35)$$

The order of magnitude of the critical pore size is determined by the factor of the natural logarithm. Significant parameters for it are the size of the crystal grain of the polycrystal d, and the modulus of external mechanical stress σ_0. In general, the critical size exceeds the width of the grain boundary by one or two orders of magnitude.

The results obtained evoke ideas about the significance of stress concentrators in general, and junction stress concentrators, in particular, for the processes of plastic deformation of polycrystals. The described mechanism of formation of a junction pore can be used both for determining the optimal parameters for the use of polycrystalline samples and for designing polycrystalline materials and structures with specified properties. It should be noted that the application of the obtained results is limited to the case of fine-grained polycrystals with a "parquet" structure.

The prospects for further research suggest an in-depth study of the energy criteria of the process of matching dislocation shifts in the grain boundary, clarification of the diffusion mechanism of the formation of the junction pore, and extension of the result to the case of a three-dimensional polycrystal.

4. CONCLUSIONS

1. The article describes the mechanism of nanopore formation at the junction of the grain boundaries of a polycrystal with a "parquet structure". At the same time, the following stages of the complete process are studied: formation of a cluster of parallel lattice dislocations inhibited in their sliding plane by the polycrystal grain boundary; passage of a dislocation shift through the grain boundary with the formation of a grain boundary dislocation of an orientation mismatch; coordination of grain boundary shifts at the junction of polycrystal grains with the formation of a junction stress concentrator; relaxation of the stress state of the junction stress concentrator due to the formation of a junction nanopore.
2. A ratio is obtained that allows us to estimate the characteristic size of the nanopore depending on the characteristic grain size of the polycrystal and the value of the external force load.
3. Modeling of the processes leading to the formation of a junction nanopore is carried out in the continuum approximation, which takes into account the variety of possible misorientation of adjacent polycrystal grains.
4. Understanding and detailing the mechanism of the origin and formation of the junction pore will allow you to anticipate, eliminate, or implement this possibility in the processes, including technological ones, associated with the study and operation of polycrystals.

ACKNOWLEDGEMENTS

The study has been supported by the Ministry of Education and Science of Ukraine via Project No. 0122U000129 "The search for optimal conditions for nanostructure synthesis on the surface of A3B5, A2B6 semiconductors and silicon for photonics and solar energy", Project No. 0121U10942 "Theoretical and methodological bases of system fundamentalization of the future nanomaterials experts training for productive professional activity", and Project No. 0123U100110 "System of remote and mixed specialized training of future nanoengineers for the development of new dual-purpose nanomaterials". In addition, the research of A.I.P. and Y.S. has been partly supported by COST Action CA20129 "Multiscale irradiation and chemistry driven processes and related technologies" (MultiChem). A.I.P. thanks the Institute of Solid-State Physics, University of Latvia, ISSP UL as the Centre of Excellence, supported through the Framework Program for European Universities, Union Horizon 2020, H2020-WIDESPREAD-01–2016–2017-TeamingPhase2, under Grant Agreement No. 739508, CAMART2 project.

REFERENCES

1. Chazalviel, J. N., Wehrspohn, R. B., & Ozanam, F. (2000). Electrochemical Preparation of Porous Semiconductors: From Phenomenology to Understanding. *Materials Science and Engineering: B*, *69*, 1–10. doi: 10.1016/S0921-5107(99)00285-8

2. Bellet, D., & Canham, L. (1998). Controlled Drying: The Key to Better Quality Porous Semiconductors. *Advanced Materials*, *10* (6), 487–490.
3. Zhang, M., Cui, X., Wang, Y., Wang, B., Ye, M., Wang, W., ... & Lin, Z. (2020). Simple Route to Interconnected, Hierarchically Structured, Porous Zn2SnO4 Nanospheres as Electron Transport Layer for Efficient Perovskite Solar Cells. *Nano Energy, 71*, 104620. doi:/10.1016/j.nanoen.2020.104620
4. Zhang, X., Wang, B., Huang, L., Huang, W., Wang, Z., Zhu, W., ... & Marks, T. J. (2020). Breath Figure–Derived Porous Semiconducting Films for Organic Electronics. *Science Advances*, *6* (13), eaaz1042. doi: 10.1126/sciadv.aaz1042
5. Zhou, X., Cheng, X., Zhu, Y., Elzatahry, A. A., Alghamdi, A., Deng, Y., & Zhao, D. (2018). Ordered Porous Metal Oxide Semiconductors for Gas Sensing. *Chinese Chemical Letters*, *29* (3), 405–416. doi: 10.1016/j.cclet.2017.06.021
6. Naderi, N., & Moghaddam, M. (2020). Ultra-sensitive UV Sensors Based on Porous Silicon Carbide Thin Films on Silicon Substrate. *Ceramics International*, *46* (9), 13821–13826. doi: 10.1016/j.ceramint.2020.02.173
7. Cai, J., Lv, C., Hu, C., Luo, J., Liu, S., Song, J., ... & Watanabe, A. (2020). Laser Direct Writing of Heteroatom-Doped Porous Carbon for High-Performance Micro-Supercapacitors. *Energy Storage Materials*, *25*, 404–415. doi: 10.1016/j.ensm.2019.10.001
8. Vambol, S., Vambol, V., Suchikova, Y., & Deyneko, N. (2017) Analysis of the Ways to Provide Ecological Safety for the Products of Nanotechnologies throughout their Life Cycle. *Eastern-European Journal of Enterprise Technologies*, *1* (10–85), 27–3. doi 10.15587/1729-4061.2017.85847
9. Ramesh, C., Tyagi, P., Bhattacharyya, B., Husale, S., Maurya, K. K., Kumar, M. S., & Kushvaha, S. S. (2019). Laser Molecular Beam Epitaxy Growth of Porous GaN Nanocolumn and Nanowall Network on Sapphire (0001) for High Responsivity Ultraviolet Photodetectors. *Journal of Alloys and Compounds*, *770*, 572–581. doi: 10.1016/j.jallcom.2018.08.149
10. Gemmel, C., Hensen, J., Kajari-Schröder, S., & Brendel, R. (2017). 4.5 ms Effective Carrier Lifetime in Kerfless Epitaxial Silicon Wafers from the Porous Silicon Process. *IEEE Journal of Photovoltaics, 7* (2), 430–436. doi: /10.1109/JPHOTOV.2016.2642640
11. Suchikova, J.A. (2015). Synthesis of Indium Nitride Epitaxial Layers on a Substrate of Porous Indium Phosphide. *Journal of Nano- and Electronic Physics, 7* (3), 03017.
12. Sundarapura, P., Zhang, X. M., Yogai, R., Murakami, K., Fave, A., & Ihara, M. (2021). Nanostructure of Porous Si and Anodic SiO2 Surface Passivation for Improved Efficiency Porous Si Solar Cells. *Nanomaterials*, *11* (2), 459. doi:10.3390/nano11020459
13. Huang, X., Cen, D., Wei, R., Fan, H., & Bao, Z. (2019). Synthesis of Porous Si/C Composite Nanosheets from Vermiculite with a Hierarchical Structure as a High-Performance Anode for Lithium-Ion Battery. *ACS Applied Materials & Interfaces*, *11* (30), 26854–26862. doi: 10.1021/acsami.9b06976
14. Suchikova, Y. (2016) Provision of Environmental Safety through the Use of Porous Semiconductors for Solar Energy Sector. *Eastern-European Journal of Enterprise Technologies,* 6(5 (84), 26–33. https://doi.org/10.15587/1729-4061.2016.85848
15. Kou, X., Machness, A., Paluch, E., & Goorsky, M. (2018). Homoepitaxial Growth of InP on Electrochemical Etched Porous InP Surface. *ECS Journal of Solid State Science and Technology*, *7* (5), P269. doi/10.1149/2.0161805jss
16. Suchikova, J.A., Kidalov, V.V., & Sukach, G.A. (2009). Blue Shift of Photoluminescence Spectrum of Porous InP. *ECS Transactions*, *25* (24), 59–64. doi: 10.1149/1.3316113
17. Suchikova, Y.A., Kidalov, V.V., & Sukach, G.A. (2010). Influence of the Carrier Concentration of Indium Phosphide on the Porous Layer Formation. *Journal of Nano- and Electronic Physics*, *2* (4), 75–81.

18. Quill, N., Clancy, I., Nakahara, S., Belochapkine, S., O'Dwyer, C., Buckley, D. N., & Lynch, R. P. (2017). Process of Formation of Porous Layers in n-InP. *ECS Transactions,* 77 (4), 67. doi: /10.1149/07704.0067ecst

19. Hassen, M., Kallel, N., & Ezzaouia, H. (2019). Analysis of Morphological, Optical and Thermal Properties of Porous p-Type Indium Phosphide p-InP (100) Prepared by the Vapor Etching Method. *The European Physical Journal Plus*, *134* (7), 1–10. doi: 10.1140/epjp/i2019-12720-1

20. Sychikova, Y.O., Bogdanov, I.T., & Kovachov, S.S. (2019). Influence of Current Density of Anodizing on the Geometric Characteristics of Nanostructures Synthesized on the Surface of Semiconductors of A3B5 Group and Silicon. *Functional Materials, 27* (1), 29–34. doi:10.15407/fm27.01.29

21. Takizawa, T. T. T., Arai, S. A. S., & Nakahara, M. N. M. (1994). Fabrication of Vertical and Uniform-Size Porous InP Structure by Electrochemical Anodization. *Japanese Journal of Applied Physics, 33* (5A), L643. doi: 10.1143/JJAP.33.L643

22. Yana, S. (2016). Porous indium phosphide: Preparation and properties. In Yana, S. *Handbook of Nanoelectrochemistry: Electrochemical Synthesis Methods, Properties, and Characterization Techniques* (pp. 283–306 X). doi: 10.1007/978-3-319-15266-0_9

23. Yang, X., Xi, F., Chen, X., Li, S., Wan, X., Ma, W., ... & Chang, Y. (2021). Porous Silicon Fabrication and Surface Cracking Behavior Research Based on Anodic Electrochemical Etching. *Fuel Cells*, *21* (1), 52–57. DOI:10.1002/fuce.202000048

24. Suohikova, Y., Vambol, S., Vambol, V., Mozaffari, N., & Mozaffari, N. (2019) Justification of the Most Rational Method for the Nanostructures Synthesis on the Semiconductors Surface. *Journal of Achievements in Materials and Manufacturing Engineering*, *92* (1–2), 19–28. doi:10.5604/01.3001.0013.3184

25. Azuelos, P., Girault, P., Lorrain, N., Poffo, L., Guendouz, M., Thual, M., ... & Charrier, J. (2017). High Sensitivity Optical Biosensor Based on Polymer Materials and Using the Vernier Effect. *Optics Express*, *25* (24), 30799–30806. doi:10.1016/j.optmat.2017.07.005

26. Adams, K. J., DeBord, J. D., & Fernandez-Lima, F. (2018). Discovery and Targeted Monitoring of Biomarkers Using Liquid Chromatography, Ion Mobility Spectrometry, and Mass Spectrometry. *Vacuum Science & Technology B, Nanotechnology and Microelectronics: Materials, Processing, Measurement, and Phenomena, 34* (5), 051804, 91. doi:10.1116/6.0000203

27. Niu, J., Albero, J., Atienzar, P., & García, H. (2020). Porous Single-Crystal-Based Inorganic Semiconductor Photocatalysts for Energy Production and Environmental Remediation: Preparation, Modification, and Applications. *Advanced Functional Materials*, *30* (15), 1908984. doi: 10.1109/JPHOTOV.2019.2912069

28. Jafarov, M. A., Nasirov, E. F., Jahangirova, S. A., & Mammadov, R. (2019). Nanostructured Cu2ZnSnS4 Thin Films on Porous-Si Wafer. *Journal of Materials and Applications*, *8* (1), 28–33. doi:10.1134/S1063785019020342

29. Heinke, L., & Wöll, C. (2019). Surface-Mounted Metal–Organic Frameworks: Crystalline and Porous Molecular Assemblies for Fundamental Insights and Advanced Applications. *Advanced Materials*, *31* (26), 1806324. doi:10.1002/adma.201806324

30. Suchikova, Y.A., Kidalov, V.V., & Sukach, G.A. (2011). Influence of Dislocations on the Process of Pore Formation in n-InP (111) Single Crystals. *Semiconductors*, *45*, 121–124. doi:10.1134/S1063782611010192

31. Zimin, S., Vasin, V., Gorlachev, E., Naumov, V., Petrakov, A., & Shilov, S. (2011). Fabrication and Study of Porous PbTe Layers on Silicon Substrates. *Physica Status Solidi C*, *8* (6), 1801–1804. doi: 10.1002/pssc.201000025

32. Ulin, V. P., & Konnikov, S. G. (2007). Electrochemical Pore Formation Mechanism in III–V Crystals (Part I). *Semiconductors*, *41*, 832–844. doi:10.1134/S1063782607070111

33. Guarini, K. W., Black, C. T., Milkove, K. R., & Sandstrom, R. L. (2001). Nanoscale Patterning Using Self-Assembled Polymers for Semiconductor Applications. *Journal of Vacuum Science & Technology B: Microelectronics and Nanometer Structures Processing, Measurement, and Phenomena*, *19* (6), 2784–2788. doi: 10.1116/1.1421551
34. Rehn, V., Hötzer, J., Rheinheimer, W., Seiz, M., Serr, C., & Nestler, B. (2019). Phase-field Study of Grain Growth in Porous Polycrystals. *Acta Materialia*, *174*, 439–449. doi:10.1016/j.actamat.2019.05.059
35. Tikare, V., Miodownik, M. A., & Holm, E. A. (2001). Three-Dimensional Simulation of Grain Growth in the Presence of Mobile Pores. *Journal of the American Ceramic Society*, *84* (6), 1379–1385. doi:10.1111/j.1151-2916.2001.tb00845.x
36. Chen, C., Sun, S., Chou, M., & Xie, K. (2017). In situ Inward Epitaxial Growth of Bulk Macroporous Single Crystals. *Nature communications*, *8* (1), 1–8. doi:10.1038/s41467-017-02197-6
37. Ng, K. W., Ko, W. S., Chen, R., Tran, T. T. D., Lu, F., Chuang, L. C., ... & Chang-Hasnain, C. (2010). Nanolasers grown on polycrystalline silicon. In *2010 23rd Annual Meeting of the IEEE Photonics Society* (pp. 78-79). IEEE. doi:10.1109/PHOTONICS.2010.5698766
38. McDonald, S. A., Burnett, T. L., Donoghue, J., Gueninchault, N., Bale, H., Holzner, C., ... & Withers, P. J. (2021). Tracking Polycrystal Evolution Non-destructively in 3D by Laboratory X-ray Diffraction Contrast Tomography. *Materials Characterization*, *172*, 110814. doi: 10.1016/j.matchar.2020.110814
39. Lazarenko, A. S., Mikhailovskij, I. M., Rabukhin, V. B., & Velikodnaya, O. A. (1995). Nanotopography and Grain-Boundary Migration in the Vicinity of Triple Junctions. *Acta metallurgica et materialia*, 43 (2), 639–643. doi:10.1016/0956-7151(94)00228-A
40. Lazarenko, A.S., Rabukhin, V.B., & Slezov, V.V. (1991). Concerning the Formation of a Junction Disclination at a Triple Junction of Boundaries under Conditions of Low-Temperature Diffusion Creep. *Physics of Metals and Metallography*, *72* (3), 48.
41. Perevezentsev, V. N., Kirikov, S. V., & Svirina, Y. V. (2020). Conditions of Strain-Induced Facet Formation during Interaction between a Lattice Dislocation Pile-Up and a Grain Boundary. *Physics of Metals and Metallography, 121*, 935 doi: 10.1134/S0031918X20100087
42. Kirikov, S.V., & Perevezentsev, V.N. (2021). Analysis of the Conditions for the Existence of Stable Microcracks in an Elastic Stress Field from a Rotational-Shear Mesodefect. *Letters on Materials, 11* (1), 50–54. doi: 10.22226/2410-3535-2021-1-50-54
43. Perevezentsev, V. N., & Chuvil'deev, V. N. (1992). The Theory of Structural Superplasticity—II. Accumulation of Defects on the Intergranular and Interphase Boundaries. Accommodation of the Grain-Boundary Sliding. The Upper Bound of the Superplastic Strain Rate. *Acta metallurgica et materialia*, *40* (5), 895–905. doi:10.1016/0956-7151(92)90066-N
44. Landau, L. D., & Lifshitz, E. M. (2013). *Quantum mechanics: Non-relativistic theory* (Vol. 3). Elsevier.

sciendo

LATVIAN JOURNAL OF PHYSICS
AND TECHNICAL SCIENCES
2023, N 6

DOI: 10.2478/lpts-2023-0034

TRANSITIONING TO DECENTRALIZED RENEWABLE ENERGY IN LATVIA: A COMPREHENSIVE PAYBACK ANALYSIS

K. Gicevskis[1,*], O. Linkevics[1], K. Karlsons[2]

[1]Faculty of Electrical and Environmental Engineering,
Riga Technical University,
12/1 Azenes Str., Riga, LV-1010, LATVIA
[2]Latvenergo JSC,
12 Pulkveza Brieza Str., Riga, LV-1010, LATVIA
*e-mail: karlis.gicevskis@edu.rtu.lv

It is believed that the transition to renewable decentralized energy supply solutions (e.g., solar panels, storage of electricity in batteries) will help promote the decarbonization of the energy system. At the same time, it is expected to happen only when society is convinced of the environmental benefits and when there are enough economic incentives for it. This study analyses the economic feasibility of transitioning to decentralized renewable energy solutions, including solar panels and electricity storage, in Latvia. Our research explores potential savings of these solutions under various scenarios based on different factors, such as national NETO billing system, financial support scheme, electricity pricing, distribution network tariffs, energy storage options, as well as the impact of the battery energy storage system (BESS) discharging strategy. The results show that the potential savings can vary depending on these factors that are changing over time. Nevertheless, the rise in small-scale power generation at households shows that there is an increasingly rapid transition from centralized electricity supply to a decentralized supply system, which might indicate that society supports energy transition.

Keywords: *BESS economic feasibility, decentralized energy supply, NETO billing systems.*

1. INTRODUCTION

Decentralized power supply solutions, such as solar panels, electric vehicle (EV) charging stations, and electricity storage systems (batteries), are becoming increasingly more popular and widely recognized by numerous countries in their endeavours to promote environmentally friendly technologies. The adoption of these technologies is influenced not only by the national legislation, but also by other factors, such as high electricity prices, enhanced electricity reliability, and the desire to be more environmentally friendly.

For example, in Latvia, the swift adoption of solar panels in the past few years was most likely driven by two factors: firstly, the high electricity prices caused by geopolitical circumstances in neighbouring countries (see year 2022 in Figure 1) and, secondly, the support for renewable energy resources provided by the Latvian government. After the start of the Russia-Ukraine war, the average electricity price in Latvia increased to 226.01 EUR/MWh in 2022, in contrast to 46.28 EUR/MWh in 2019, or 34.05 EUR/MWh in 2020, and 88.78 EUR/MWh in 2021, respectively. In early 2023, however, the prices were slightly lower than those recorded in 2022 [1].

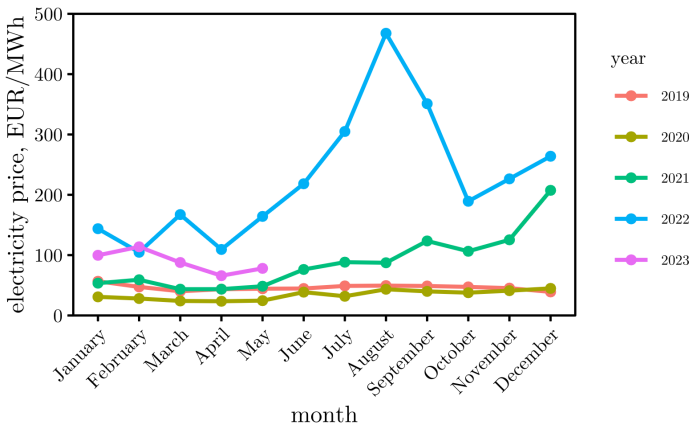

Fig. 1. Nord pool average day-ahead electricity price in the Latvian trade area [1].

By installing solar panels or small wind turbines, Latvian residents had the opportunity to receive financial support by means of the following two support programs:

- the support provided by the administered programme of ALTUM ranges from 700 to 4000 EUR, depending on the nominal power of the inverter.
- the support provided by the Emission Allowance Auction Instrument (EKII) also ranges from 700 to 4000 EUR, depending on the nominal power of the inverter.

Funding from the EKII support program is only available after the purchase and installation of the equipment. On the contrary, to receive the ALTUM support, one first needs to apply for the programme, await approval, and then commence the work. The EKII programme has a total funding of 40 million EUR, while ALTUM has a funding allocation of 3.66 million EUR [2].

These circumstances have led to a situation where, within a relatively short period, the total number of microgenerators (mostly

solar) has surpassed 15,000 units (Fig. 2), with their combined production capacity already exceeding 120 megawatts (MW).

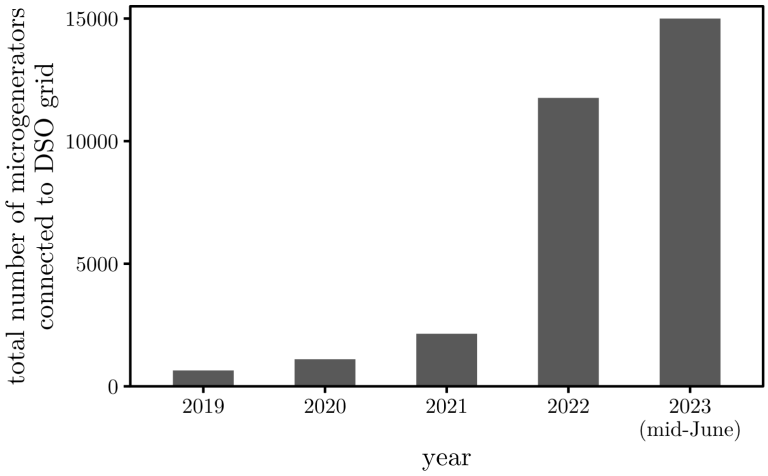

Fig. 2. Number of microgenerators connected to DSO (distribution system operator Sadales tīkls JSC) grid [3], [4].

The electricity generated by microgenerators is primarily directed towards enabling households to meet their own energy needs, including charging their EVs. EVs are widely recognized as one of the most promising solutions to mitigate environmental impact in the transportation sector and improve energy efficiency. When the electricity for EVs is sourced from a grid predominantly powered by fossil fuels, their life cycle emissions are comparable to vehicles with combustion engines. However, when renewable energy sources are predominant in the energy system, EVs emissions are slightly lower. To truly achieve sustainability in using EVs, it is required to shift the future of electricity towards renewable sources.

Among renewable energy resources, such as wind and solar power, solar energy is considered the most promising in the context of EV charging (see Table 1).

Table 1. Comparison of Charging EV from Wind or Solar Energy Source [5], [6]

Category	Wind energy	Solar energy
1	Onshore and offshore wind is far from where EVs can be charged	Close to where EVs can be charged. For example, rooftop photovoltaic (PV), so transmission is not needed
2	Different power scales: wind turbines in MW while EV chargers in kW. While on the other hand, with wind turbines it could be possible to charge several thousand EVs	Power scales are similar for rooftop PV and EV charger (both kW)
3	Generation is mostly in winter and night time	Generation is mostly in daytime and summer

In most scenarios, one advantage of solar energy as well as EV batteries is that those operate on direct current (DC) power. However, when it comes to grid integration,

the standard is alternating current (AC). This leads to the need for unnecessary DC-AC-DC conversions, which can result in energy losses. In contrast, utilizing DC power directly, without conversion, proves to be more efficient [5].

In addition to the support available for installing microgenerators in Latvian households, there is also financial support available for individuals purchasing EVs. A grant of 4,500 EUR is provided when purchasing a new electric car, while a grant of 2,250 EUR can be received when purchasing used electric cars and new externally chargeable hybrid cars. However, there is a purchase price limit of 60,000 EUR for low-emission and zero-emission vehicles in their basic configuration, as stipulated by regulations. Additionally, there is an extra 1,000 EUR support available for beneficiaries, who choose to write off their existing vehicle and hand it over to a processing company [7].

However, unlike microgenerators and electric cars, electricity storage systems (batteries) have not yet been widely adopted in Latvia, and the government has not provided financial support for such equipment. This could be related to the existing NETO accounting system for microgenerators. The NETO accounting system has traditionally allowed for the virtual storage of electric energy produced by microgenerators, enabling its later use, for example, during winter months [8]. Perhaps this is one of the reasons why batteries have not been so popular so far.

However, Latvia has recently made amendments to the Electricity Market Law, resulting in the introduction of a new and improved system, called NETO settlement system. The new NETO settlement system not only records the amount of electricity generated and consumed by customers, but also assigns monetary value to this energy. The advantages of the new system have been communicated and include:

- applicability to both households and legal entities (the previous system included only private consumers);
- conversion of electricity produced and transferred to the grid into monetary terms, allowing for savings that can be utilized towards future bill payments or applied to electricity costs in other connections of the same customer, as per the conditions of the chosen electricity service provider;
- the net savings period is not limited by law;
- the freedom to select the most suitable service provider and the flexibility to switch between providers;
- active participation in the electricity market, enabling cost control by tying the value of energy transferred and received to market prices and settlement conditions. Encouragement of consumption habits that maximize the profitability of electricity production and consumption. These changes aim to empower consumers by providing greater control over their electricity usage and promoting a more economically advantageous approach to energy consumption [9].

Although there is extensive information regarding the new rules of the NETO settlement system in Latvia, there is a lack of detailed explanation for general public regarding the potential economic implications for owners of decentralized energy supply solutions [10].

This publication proposes three hypotheses. Firstly, the introduction of the new NETO system will reduce the homeowners' interest in switching to solar panels. Secondly, the implementation of the new system has the potential to motivate homeowners to actively invest in and utilize stationary batteries. And, thirdly,

the smart BESS management system will determine the level of savings achievable by the storage. This publication could serve as a useful material for people and policy makers to evaluate new initiatives for the implementation of decentralized electricity supply solutions.

The publication compares the previous NETO accounting system with the new NETO settlement system. Such an analysis would allow for a more accurate assessment of the introduction of new technologies and prediction of the effect of regulatory enactments on the economic viability of different situations.

The second chapter examines changes in the NETO accounting and settlement systems in Latvia. The hypotheses are defined and possible directions for future research are discussed. Section 3 defines the methodology and assumptions used in the two case studies for mathematical calculations to evaluate the NETO accounting and settlement systems, as well as BESS discharging strategy. Section 4 presents the calculation results, while Section 5 discusses the results and summarises conclusions from this work.

2. THE OVERVIEW OF THE CURRENT SITUATION

2.1. NETO Accounting and Settlement System in Latvia

According to the amendments made to the Electricity Market Law on 16 February 2023, significant changes have been implemented concerning microgeneration producers in Latvia.

NETO accounting system (pre-existing system; Fig. 3): Previously, the law regulated the NETO electricity accounting system, which outlined the procedure for the distribution system operator to settle payments for electricity produced by users from renewable energy resources. This system applies to the cases when the produced electricity is not immediately consumed but transferred to the grid. If the amount of electrical energy transferred to the grid exceeds the energy received from the grid, the excess energy is carried forward to the next billing period within a NETO year (starts on 1 March and ends on the last day of February). "Energy storage" can only be utilized within the same property (for the specific system connection) where it was generated. At the beginning of a new NETO year, all savings are deleted. It is important to note that the NETO accounting system is currently limited to households and is automatically applied after receiving permission to connect the microgenerator (when the amendments to the law take effect, it will be possible to join the scheme until 31 December 2023).

NETO settlement system (new system; Fig. 4): The Amendments to the Electricity Market Law introduced a new NETO electricity settlement system. This system not only records the quantity of electricity produced and consumed by the customer, but also determines the monetary value of this energy. If the total value of the electricity produced, but not immediately consumed (and transferred to the distribution network) exceeds the value of the electricity received from the same network, the surplus value can be credited in the subsequent settlement period or used for electricity payments in another connection of the same customer. Both households and legal entities will be eligible to participate in the NETO settlement system.

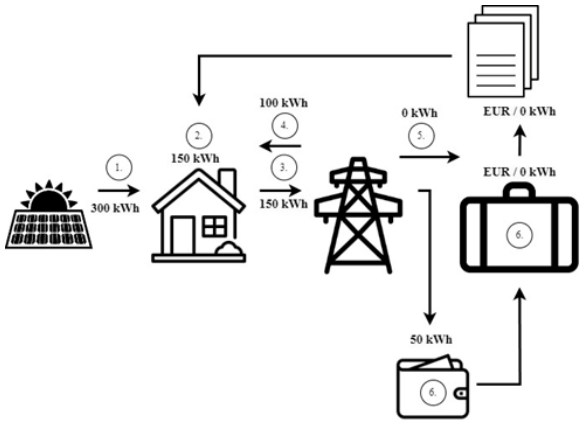

Fig. 3. Schematic representation of the NETO accounting system – the customer transferred 50 kWh more to the electricity network than he received from the network. The customer only has to pay the service fee of the distribution system operator this month, but does not have to pay for electricity [9].

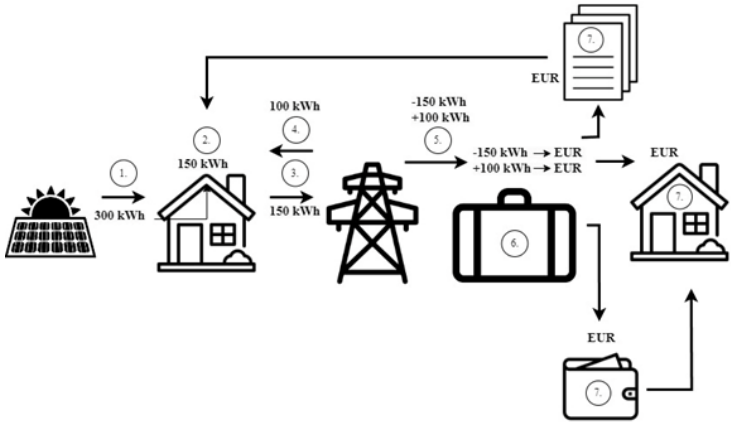

Fig. 4. Schematic representation of the NETO settlement system – the electricity trader determines the value of the electricity transferred to the common power grid and received from the common power grid [9].

The law mandates that electricity traders must include the NETO settlement system as part of their trading services. Currently, the Cabinet of Ministers is in the process of developing detailed operational guidelines for the NETO settlement system and determining the date when it will be made available to customers [9].

2.2. Definition of the Problem and Hypothesis

The authors propose three hypotheses regarding the impact of the new NETO settlement system:

- Hypothesis A: The introduction of the new NETO settlement system may reduce the economic viability of installing solar panels.
- Hypothesis B: The new NETO settlement system is expected to emphasize the importance of batteries in enhancing the profitability of investments in green technologies.

- Hypothesis C: The smart BESS management system will determine the level of savings achievable by the storage capacity.

2.3. Future Research Prospects

In the future, conducting research on the economic viability of various green technologies, particularly under scenarios such as energy arbitrage or their potential integration with energy communities, would offer significant advantages and insights. Currently, energy communities and the concept of electricity sharing have not gained significant popularity in Latvia. Moreover, there is a need for further exploration and understanding of the development and utilization of virtual power plants. By conducting additional studies in these areas, we can gain valuable insights into the potential benefits and feasibility of implementing decentralized energy solutions. This knowledge will play a vital role in facilitating the transition to a green economy in Latvia.

3. TWO CASE STUDY ASSUMPTIONS

The first case study considers a single household as an electricity consumer with access to an electric grid, solar panels, and an electricity storage system in various operating scenarios of the NETO accounting system and the NETO settlement system. Figure 5 shows a block scheme of the case study.

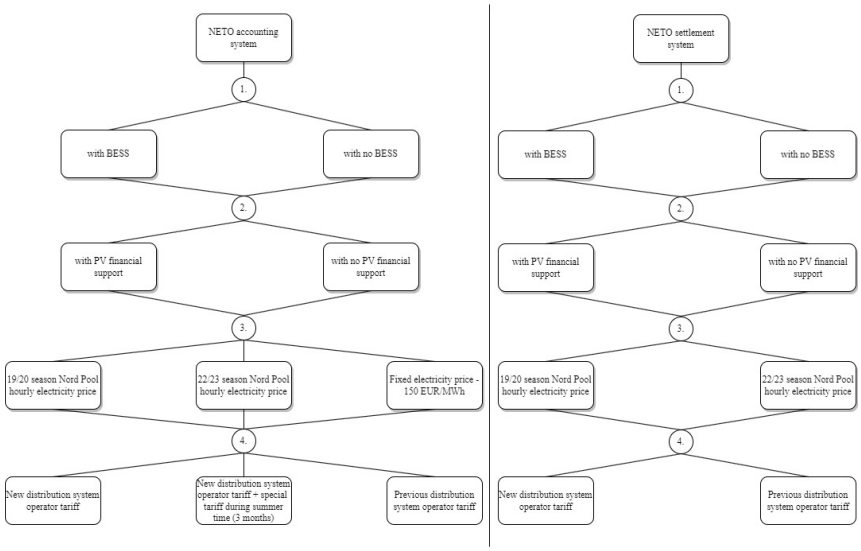

Fig. 5. Block scheme of the first case study which compares different operating scenarios of the NETO accounting system and the NETO settlement system.

The authors compare two NETO system alternatives to investigate how potential household savings change according to different scenarios, namely, with BESS, without BESS, with financial support for their PV system, and without financial support for their PV system.

A significant focus is placed on electricity prices, which have shown considerable volatility in recent years and play a crucial

role in determining the economic payback for the installed electricity supply solutions. The authors have thoroughly analysed potential savings, considering the impact of the new distribution system tariff, which affects all current customers connected to the grid of the Latvian distribution system operator. Additionally, the implications of the newly introduced special tariff, which is available free of charge to any user, have been explored.

To study the new NETO settlement system and to compare it with the NETO accounting system, the following annual data at a 1-hour resolution were obtained for one anonymous household from the Latvian distribution system operator Sadales tīkls JSC: date and time, electricity consumption, and electricity generation [11]. The yearly electricity demand of the household was 11.32 MWh, while solar energy injected to the grid reached 4.23 MWh on an annual basis. Unfortunately, information about the specific lifestyle and electricity consumption patterns in the household was not available, including the usage of various appliances. It must also be acknowledged that there is a lack of available data on electricity production, which households consume directly from solar panels (the so-called self-consumption). To ensure a higher economic benefit, households with solar panel systems should achieve the highest possible level of direct electricity consumption. According to [8], the level of direct consumption by households in Europe is 20–30 %.

Using input data described above (including Fig. 5), as well as in Table 2, the authors analysed all respective scenarios.

Table 2. Input Data and Assumptions of Household Power Supply System [8], [11], [12]

Characteristic	**Indicator or assumption**
Self-consumption	30 %
Solar system capacity and cost	5 kW, 1200 EUR/kw, which have a possibility to receive the financial support of 2500 EUR
Electricity storage systems (BESS) energy capacity, costs, and operation	10 kWh, 7000 EUR. Maximum discharge level – up to 2 kWh, maximum charging – up to 10 kWh. Roundtrip efficiency is considered 90 %
Current magnitude of the input protection apparatus (IAA) and phases for the electricity connection	three phases and 25 A
Previous distribution network tariff	• charge for electricity supply 0.04076 EUR/kWh • charge for IAA current magnitude 2.4 EUR/A/year
New distribution network tariff	• charge for electricity supply 0.03985 EUR/kWh • charge for IAA current magnitude 0.92 EUR/A/month
New special distribution network tariff	• charge for electricity supply 0.1594 EUR/kWh • charge for IAA current magnitude 0.37 EUR/A/month

While the second case study considers a farm as an electricity consumer that is registered as a legal entity with access to the electric grid and installed solar panels. In this case study, the electricity storage system is added and evaluated for various operating scenarios of the NETO settlement system. Figure 6 shows a block scheme of the second case study scenarios.

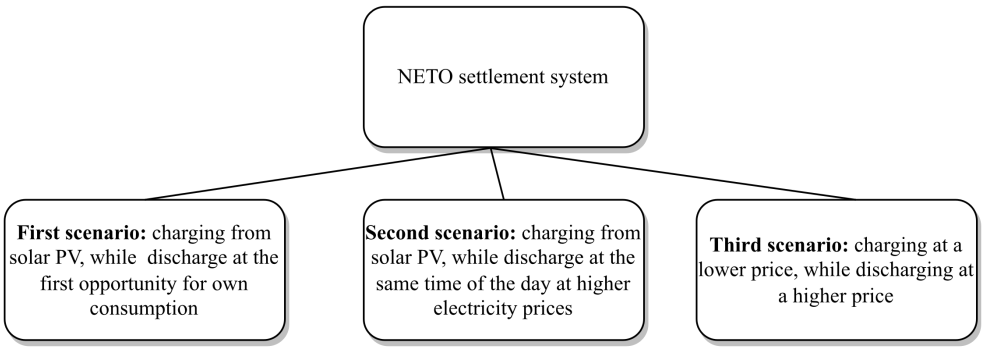

Fig. 6. Scheme of the second case study in which three scenarios of the NETO settlement system are investigated and compared using a farm with installed solar panels as an example.

In the second case study, the authors compare three alternatives to examine the best possible scenarios of BESS discharge possibilities and to evaluate savings that could be expected from the smart BESS system management. In all scenarios, annual data at a 1-hour resolution were obtained for one farm of an anonymous customer from Sadales tīkls JSC [11]. The yearly electricity demand of the farm was 8,279 MWh, while the solar energy injected to the grid reached 17,163 MWh on an annual basis (see Fig. 7). Unfortunately, like in the first case study, there is no information on the specific electricity consumption patterns at this facility, including information on a contract with an energy trader for the purchase of the produced electricity. As can be seen in Fig. 7, on average, the farm produced more than twice as much electricity as it consumed.

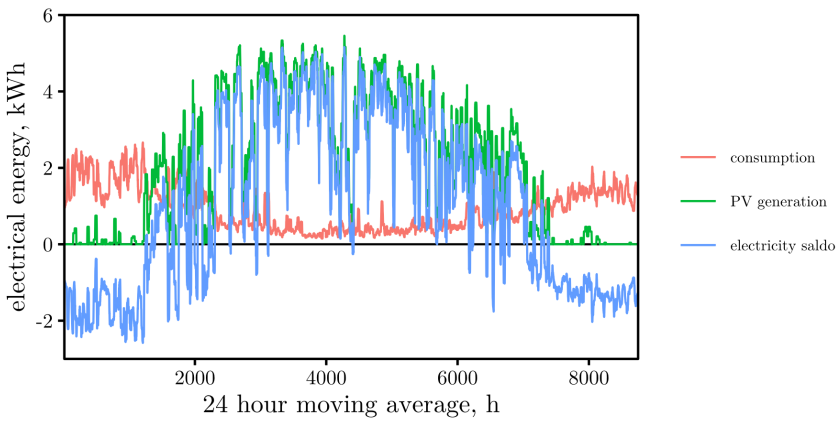

Fig. 7. Characteristics of electricity supply at the farm. 24 h moving average was plotted instead of the raw hourly data to improve the visual clarity of the plot [11].

Using data described above (including Fig. 6 and Fig. 7), as well as in Table 3, the authors have analysed all three scenarios.

Table 3. Input Data and Assumptions of the Farm Power Supply System [11], [12]

Characteristic	Indicator or assumption
Electricity storage systems (BESS) energy capacity, costs, and operation	Energy capacity 15-30-50 kWh, and 10 kW power capacity with capex 225 EUR/kW and 600 EUR/kWh accordingly. BESS charging and discharging efficiency – 95 %
BESS degradation	1.5 %
New distribution network tariff	• charge for electricity supply 0.03985 EUR/kWh • charge for IAA current magnitude 0.92 EUR/A/month
Electricity price	Three scenarios analysed with different electricity prices – the 2018 and 2022 season Nord pool exchange prices. Value added tax is not considered.

The significance of selecting the optimal operational mode and energy capacity for BESS is becoming a progressively more important topic for discussion. This analysis aims to approximate the advantages of installing a BESS in a power system that already incorporates solar panels.

4. ASSESSMENT RESULTS

4.1. The First Case Study – NETO Accounting System

In Figure 8, the potential savings from solar panels using the NETO accounting system are illustrated. The graph shows the savings based on the current distribution network tariffs and the new ones, as well as considering scenarios with different electricity prices – the 2019–2020 and 2022–2023 season Nord pool exchange prices, fixed electricity price (150 EUR/MWh) and a scenario with the DSO special tariff. Note that the "Special" tariff is intended for households with very small or seasonal electricity consumption. It is assumed that a special tariff is used for three months (June, July and August), leaving the basic tariff for the remaining months. The special tariff includes a smaller fixed part (capacity maintenance fee, EUR/month); however, it has a higher variable share (charge for electricity supply, EUR/kWh) compared to the basic tariff.

The calculation algorithm has been developed to assess potential savings when compared to a scenario where no solar panels are employed and with a relevant DSO tariff. In this case, BESS is not integrated into the system. This algorithm encompasses both the fixed component (averaged across the total annual consumption) and the variable part of the distribution network tariff, factoring in the per-consumed kilowatt-hour, when computing potential savings. Accumulated savings are represented by the bars, while the horizontal lines show the investment in the solar panel system with and without the financial support of the government (assumed to be 2500 EUR).

Figure 8 shows that the lowest potential savings are made in the scenario in which the 2019–2020 Nord pool electricity exchange prices are adopted (the lowest at the old DSO tariff). It can also be seen that with the Nord Pool prices of the 2022-2023 season and with the new DSO tariff, the savings could exceed the investments made already starting from the third year, in the case of receiving state support for the installation of solar panels. The significant

potential for savings arises from the Nord Pool prices during the 2022–2023 season. In all scenarios, it can be seen that the old tariff system would slow down the savings for the solar panel system, meaning that the new tariff system is more beneficial (as it is more expensive). While it is true that, in certain scenarios, the "special" tariff offers greater benefits when compared to the fixed electricity price with both old and new DSO tariffs, it is important to acknowledge that, overall, the electricity price remains the primary determinant in influencing the savings.

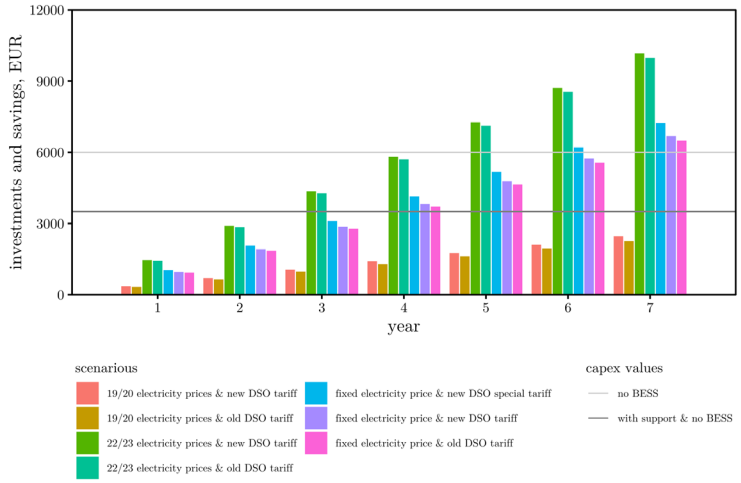

Fig. 8. Potential savings under NETO accounting system with no BESS in a 7-year period.

Figure 9 shows the potential savings when a BESS system is installed in parallel with solar panels. The algorithm assumes that electricity is consumed from the grid only when it has reached a discharge level of 2 kWh in the installed BESS system. Similar to the scenario shown in Fig. 8, it can also be observed here that the old tariffs and low electricity prices slow down the potential savings. At the same time, it is possible to achieve savings at the Capex level in the case of state financial support or high electricity prices for seven consecutive years.

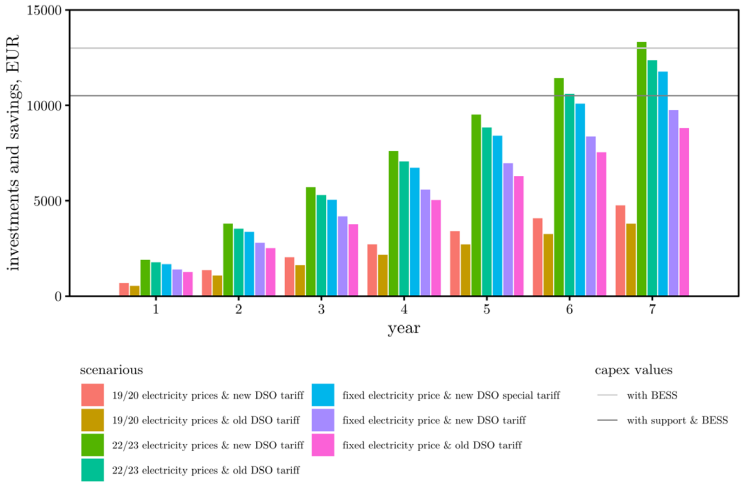

Fig. 9. Potential savings under the NETO accounting system with BESS in a 7-year period.

Unlike before, when there was no BESS system, having a BESS system and a fixed electricity price in this case does not lead to savings equal to the initial investment.

4.2. The First Case Study – NETO Settlement System

A similar algorithm has been created for the assessment of the NETO settlement system. In this case, it is assumed that excess electricity is sold to the electricity trader at a relevant Nord pool price. The potential savings of the NETO settlement system are shown in Fig. 10, where the bars represent accumulated savings, and the horizontal lines show the investment in the solar panel system with and without financial support. In Fig. 10, BESS is not integrated into the system. As can be seen, electricity prices have a significant impact on potential savings, i.e., at low market prices and even with subsidies, a solar panel system may not pay off during seven years. Conversely, at high electricity rates and the new DSO tariff, such a system would pay off at around the third year. It can be observed that the savings achieved with the new tariffs are slightly higher than those with the old tariffs.

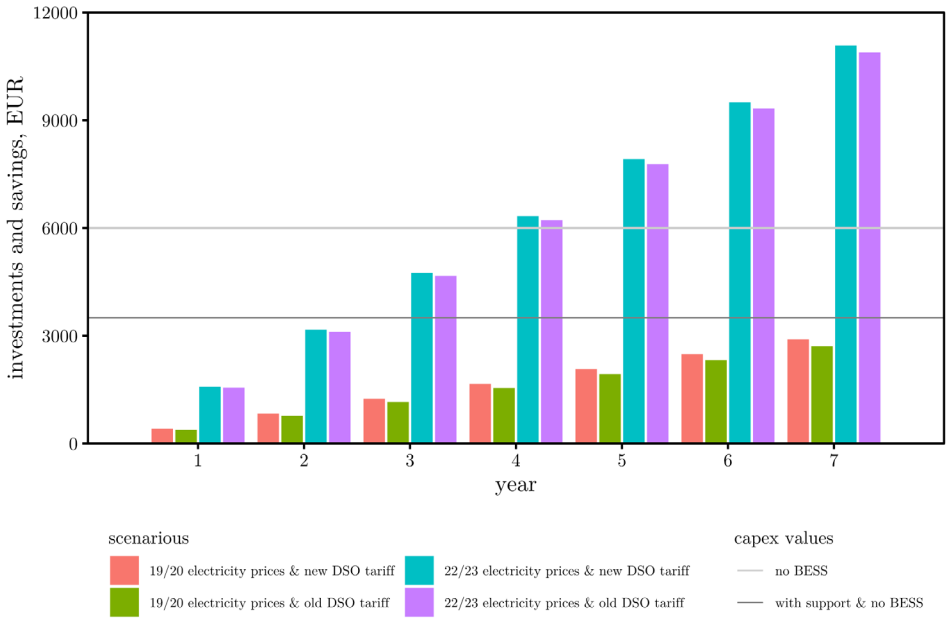

Fig. 10. Potential savings under the NETO settlement system with no BESS in a 7-year period.

Figure 11 shows the potential savings with BESS. Again, the algorithm assumes that electricity is consumed from the grid only when it has reached a discharge level of 2 kWh in the installed BESS. It can be observed that the new tariffs increase the potential savings also in this case. At the same time, it is possible to achieve savings at the Capex level only in the case of state financial support and with high electricity prices.

At low electricity prices, in this case, savings up to the Capex level can hardly be achieved. It could happen only at high electricity rates.

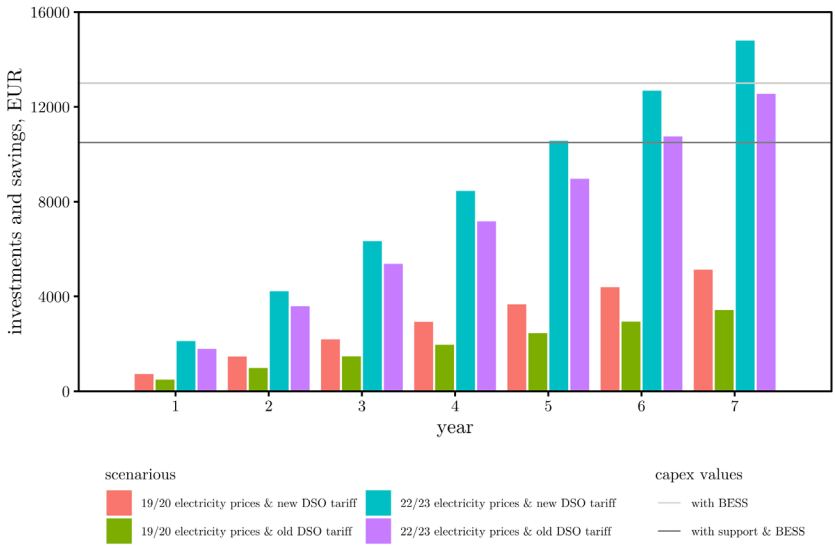

Fig. 11. Potential savings under the NETO settlement system with BESS in a 7-year period.

4.3. The Second Case Study – The BESS Management System

In the second case study, three algorithms have been developed to evaluate savings from different BESS discharge and charge management approaches. Energy storage capacities have been assumed and varied – 15, 30, and 50 kWh. This, the second case study, involves a farm operating under the NETO settlement system, equipped with a pre-existing solar panel system.

In the first scenario, the BESS is charged using solar PV, and discharge occurs as soon as there is an opportunity for self-consumption. The second scenario involves charging from solar PV but discharging during peak electricity pricing hours. In the third scenario, the BESS is charged at the lowest electricity rates and discharged when prices are higher.

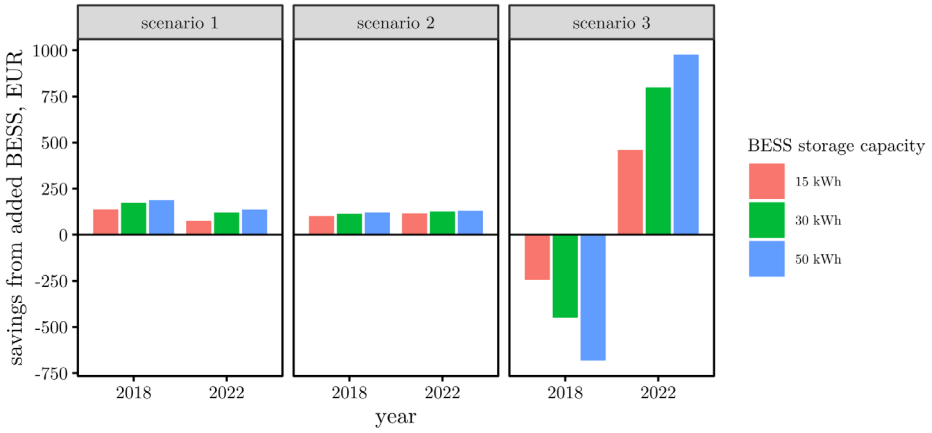

Fig. 12. Potential savings for three different scenarios with BESS. Years – 2018 and 2022 – represent different electricity prices based on which calculations have been made.

The analysis is conducted using the new tariffs of the DSO, as well as separately considering the 2018 and 2022 Nord Pool electricity exchange prices in the Latvian electricity trading area. Unlike the first case study, this analysis excludes the consideration of value-added tax. Figure 12 illustrates the potential savings of installing BESS across all three scenarios.

In the case of the first scenario, the results show that by creating an additional BESS system, marginally higher savings can be achieved in the case of a larger BESS capacity and lower electricity prices, which were lower in 2018 than in 2022 (the average price in 2018 was 49.89 EUR/MWh, while in 2022 it was 226.32 EUR/MWh).

When considering the second scenario, the results show that neither the BESS energy capacity nor the electricity prices of 2018 or 2022 lead to a significant difference in savings. Overall, the savings are very similar.

On the other hand, in the third scenario there is a significant discrepancy between savings made in 2018 and 2022, as a result of different electricity prices. At the prices of 2018, the savings were estimated to be negative, which could be related to the fact that in 2018 the changes in electricity prices during the day were relatively small, unlike in 2022. This scenario also highlights how the savings are affected by the choice of the energy capacity of the BESS system used; for example, in 2022, the difference in savings between the 15 and 50 kWh BESS is 500 EUR. In general, in 2022, the greater the installed BESS energy capacity was, the greater the savings were.

5. DISCUSSION AND CONCLUSIONS

Although the Cabinet of Ministers in Latvia is still in the process of developing detailed regulations (they have not yet come into effect) for the operation of the NETO settlement system, including the date at which the NETO settlement system will become available to customers, it is theoretically possible to predict how it will affect the potential savings from the use of decentralized electricity supply solutions.

When comparing yearly savings at the NETO accounting system without BESS to the NETO settlement system without BESS under the new DSO tariff, it is evident from the results that the difference in potential savings is not large and varies from +8 % to +15 % for the 2022/2023 and 2019/2020 electricity prices, respectively. For example, if we consider the 2022/2023 electricity prices, then in seven years one could save around 10 166 EUR and 11 079 EUR using the NETO accounting system and the NETO settlement system, respectively. Similarly, using the same approach, for the 2019/2020 electricity prices, the savings could be 2 459 EUR compared to 2 904 EUR. In the case of the NETO accounting system, it is worth considering a scenario with a fixed electricity price (150 EUR/MWh), which would result in potential savings of 6 690 EUR. Despite the significant potential for savings, the choice of the special tariff should be individually assessed with caution, as it offers benefits to the consumer only when their electricity consumption from the grid is exceptionally low.

The analysis has clearly shown that when electricity prices are higher, savings increase significantly. When this happens, there is less need for financial help from the government. Hence, it is reasonable to consider focusing the governmental support for cases when it is harder to make green solutions like BESS profitable, as this is

where the help would be most effective. In addition, it can also be concluded from Figs. 8–11 that distribution tariffs can affect the payback of solar panels, but on a much smaller scale. In the case of the new DSO tariffs, the savings of the solar panel system will be higher compared to the old DSO tariffs.

When we compare the NETO accounting system with BESS to the NETO settlement system with BESS at the new or old DSO tariff, it is clear that the difference in potential savings is not very large either. For example, if we consider the 2022/2023 electricity prices and the new DSO tariff under the NETO settlement system around 14 800 EUR could be saved in seven years, while under the NETO accounting system it might be possible to save approximately 13 324 EUR. Similarly, using the same approach for 2019/2020, the savings could reach 5 127 EUR compared to 4 759 EUR. Under the NETO accounting system and with a fixed electricity price (150 EUR/MWh), it could be possible to achieve potential savings of 9 759 EUR. While there are cases when the savings could eventually cover the initial BESS system investment, in most situations, buying BESS may not lead to a quick payoff.

To improve the battery payback, different BESS management strategies have been considered, and the savings directly generated by an installed BESS system have been calculated.

In the first two scenarios, where BESS discharging is allowed at the first opportunity or during periods of higher electricity prices on the exchange for the relevant day, savings of 74 to 188 EUR (excluding VAT) could be achieved annually. While, if this BESS is allowed to charge from the grid and discharge at higher prices (by doing arbitrage), then BESS savings could reach 460–977 EUR per year. However, at the same time, it must be recognized that with the 2018 electricity prices, such a strategy would not pay off. On the contrary, it could cause losses that might have arisen from a not too large price difference on the electricity market. The results (see Fig. 12) indicate that the payback of BESS can be affected by both the energy capacity of the battery and price changes in the electricity exchange.

Based on the findings presented in this publication, it can be concluded that the hypothesis A has been neither right nor wrong. The savings from solar panels will mainly depend on the electricity market price rather than the NETO billing system. The evidence shows that the new payment system might be a slightly better economically when it comes to installing solar panels. On the other hand, the results support the confirmation of the hypotheses B and C. The analysis has demonstrated cases where installing BESS can actually save enough money to justify the investment. In addition, if BESS operations are managed effectively, it can result in even better savings.

ACKNOWLEDGMENTS

The research has been supported by the European Social Fund within the Project No 8.2.2.0/20/I/008 “Strengthening of PhD Students and Academic Personnel of Riga Technical University and BA School of Business and Finance in the Strategic Fields of Specialization” of the Specific Objective 8.2.2 “To Strengthen Academic Staff of Higher Education Institutions in Strategic Specialization Areas” of the Operational Programme “Growth and Employment”.

REFERENCES

1. Nord Pool. (accessed June 12, 2023). *Nord Pool Market Data.* Available at https://www.nordpoolgroup.com/en/.
2. Emission Allowance Auction Instrument (EKII). (accessed June 22, 2023). *Atbalsta programmu iedzīvo-tājiem salīdzinājums*. Available at https://ekii.lv/index.php?page=programmu-salidzinajums.
3. Sadales tīkls. (accessed July 2, 2023). *Elektroapgādes apskats*. Available at https://sadalestikls.lv/lv/elektroapgades-apskats.
4. Sadales tīkls. (accessed June 26, 2023). *Elektrību pašražojošu mājsaimniecību skaits latvijā sasniedz 15 000*. Available at https://sadalestikls.lv/lv/aktuali/elektribu-pasrazojosu-majsaimniecibu-skaits-latvija-sasniedz-15-000.
5. Chandra Mouli, G.R., Bauer, P., & Zeman, M. (2020). System Design for a Solar Powered Electric Vehicle Charging Station for Workplaces. *Appl. Energy*, *168*, 434–443. doi: 10.1016/j.apenergy.2016.01.110.
6. Ram, G. (2021). *Charging EVs from Renewables*. Delft University of Technology and D-INCERT.
7. LV portals. (accessed July 2, 2023). *Stājas spēkā noteikumi valsts atbalstam elektroauto iegādei*. Available at https://lvportals.lv/skaidrojumi/336262-stajas-speka-noteikumi-valsts-atbalstam-elektroauto-iegadei-2021.
8. Zemīte, D., Sauhats, L., Petričenko, A., Kozadajevs, Ļ., & Bezrukovs, J. (2018). Elektroenerģijas NETO sistēmas izvērtējums un priekšlikumi sistēmas uzlabojumiem. Available at https://www.em.gov.lv/lv/neto-sistema-elektroenergijas-mikrogeneracijai/elis_neto_10.08.2018_nodevums1.pdf.
9. Sadales tīkls. (accessed August 2, 2023). *NETO uzskaite un NETO norēķini*. Available at https://sadalestikls.lv/lv/blog/post/neto-uzskaite-un-neto-norekini.
10. Linkevics, O., Gicevskis, K., & Groza, E. (2022). Jauni elektroenerģijas tirgus dalībnieki un tehnoloģijas – regulatīvie izaicinājumi. *Jurista vards*, 1247 (33). Available at https://juristavards.lv/doc/281778-jauni-elektroenergijas-tirgus-dalibnieki-un-tehnologijas-regulativie-izaicinajumi/.
11. Sadales tīkls. (accessed June 27, 2023). *Datu kopas inovāciju attīstībai*. Available at https://sadalestikls.lv/lv/inovacijas.
12. Sadales tīkls. (accessed August 23, 2023). *Sadales sistēmas pakalpojumu tarifi*. Available at https://sadalestikls.lv/lv/tarifi.

sciendo

LATVIAN JOURNAL OF PHYSICS
AND TECHNICAL SCIENCES
2023, N 6

DOI: 10.2478/lpts-2023-0035

SELECTIVE PATTERNED GROWTH OF ZnO NANONEEDLE ARRAYS

I. Mihailova[1,*], M. Krasovska[1], E. Sledevskis[1], V. Gerbreders[1], V. Mizers[1], A. Bulanovs[1], A. Ogurcovs[1,2]

[1] G. Liberts' Innovative Microscopy Centre, Department of Technology, Institute of Life Sciences and Technology, Daugavpils University, 1a Parades Str., Daugavpils, LV-5401, LATVIA
[2] Institute of Solid State Physics, University of Latvia, 8 Kengaraga Str. 8, Riga, LV-1063, LATVIA
*e-mail: irena.mihailova@du.lv

Nanostructured coatings are widely used to improve the sensitivity of various types of sensors by increasing the active surface area compared to smooth films. However, for certain applications (in some cases), it may be necessary to achieve selectivity in the coating process to ensure that nanostructures only form in specific areas leaving interelectrode spaces free of nanostructures. This article discusses several methods for creating intricate ZnO nanostructured patterns, including area selective application of Zn acetate seeds followed by hydrothermal growth, selective thermal decomposition of zinc acetate via laser irradiation followed by hydrothermal growth, and the electrochemical deposition method. These methods enable ZnO nanostructures to grow onto designated surface areas with customised, patterned shapes, and they are rapid, cost-effective, and environmentally benign.

The article examines the process of producing a nanostructured coating with a complex shape and discusses several factors that can impact the quality of the final product. These include the influence of the thermocapillary flows and the "coffee stain" effect on the deposition of a seed layer of zinc oxide from an ethanol solution of zinc acetate. Additionally, the study found that using a protective screen during the growth of nanostructures can reduce the occurrence of unintended parasitic structures in areas lacking a seed layer. Overall, the article presents various techniques and strategies to improve the quality of nanostructured coatings.

We have proven that the use of laser radiation to create a seed layer does not impact the final morphology of the resulting nanostructures. However, when combined with computer-controlled technology, this approach allows for the creation of intricate patterns made up of micrometre-sized lines which cannot be achieved by using other methods.

The article also demonstrates an electrochemical technique for obtaining zinc oxide nanostructures that can selectively coat metal electrodes without requiring a seed layer.

Keywords**:** *Hydrothermal synthesis, nanostructures, selective patterning, ZnO.*

1. INTRODUCTION

At present, nanostructured surfaces have a wide range of applications: solar energy [1], electronics [2], medicine [3], [4], etc. They are also widely used in the development of sensors, proving to be a very effective material for the production of gas sensors [5]–[7], biosensors [8]–[11], and chemical sensors [12], [13]. This is mainly due to the fact that surface nanostructuring significantly enhances sensitivity by increasing the active surface area. Furthermore, the development of nanostructured materials allows for the creation of enzyme-free sensors, which operate based on the direct interaction between analytes and nanostructures [14]–[17]. In a number of cases, this makes it possible to refuse additional functionalisation of the surface with complex organic molecules and enzymes without the loss of sensor sensitivity, which significantly reduces the cost of its production and increases the resistance to mechanical and thermal influences that the sensor is subjected to during production and operation.

There is a large number of physical and chemical methods for obtaining nanostructures, including physical dispersion [18], condensation from liquid [19], [20] and gas phases [21], combustion methods [22], plasma-chemical methods [23], synthesis of nanoparticles from solution [24], [25], sol-gel synthesis [26]–[28], and lithographic [29], [30] and probe methods [31].

Numerous nanostructured materials can be produced using the methods outlined above; however, metal oxide nanostructures, and in particular ZnO, have become widespread. Due to the combination of optical, electrical, and piezoelectric properties of ZnO, it is widely used in optoelectronics and electronic device fabrication [32], [33]. ZnO is biocompatible [34] and relatively stable at biological pH values [35], [36]. This allows for its use as biological markers and as a sensor platform for the detection of different kinds of biomolecules [37]. Hydrothermal synthesis is one of the most promising methods for obtaining metal oxide nanoparticles and epitaxial nanostructured coatings [25], [38]. Compared to other methods of obtaining ZnO nanostructures, hydrothermal synthesis offers a lot of advantages [25], [39]. This method of synthesis is environmentally friendly as it does not require the use of toxic raw materials nor does it generate toxic by-products during the process. Additionally, it is a cost-effective and straightforward approach that does not necessitate expensive raw materials or complex equipment, nor does it require special growing conditions like ultrahigh vacuum, ultrahigh or ultralow temperature and pressure. The synthesis occurs in an aqueous solution at temperatures that typically do not exceed 100 ˚C. The use of relatively low temperatures eliminates the limitations on the types of surfaces that can be coated with nanostructures. This method can be applied to coat any chemically inert surface with nanostructures, including those that are susceptible to high temperatures such as soft polymers, fabrics, and even paper. Hydrothermal synthesis surpasses other nanostructure synthesis techniques in terms of the diversity of morphologies that can be obtained. Our previous studies described in the publication [40] show that ZnO can be obtained in at least 10 different morphologies: nanoparticles, nanoneedles, nanorods, nanoplates, nanoflowers, etc. The standard sample preparation scheme includes the following steps:

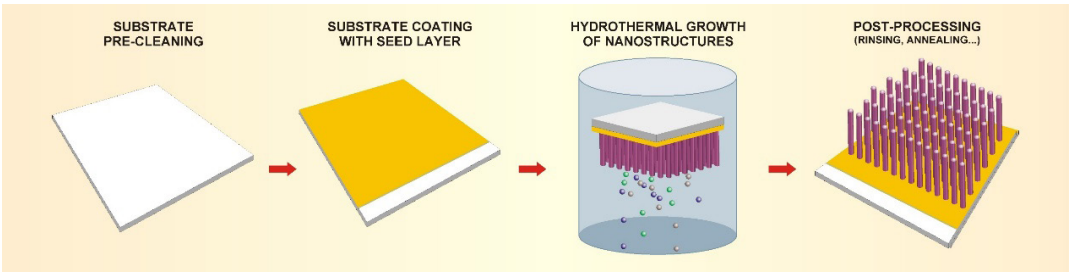

Fig. 1. Basic steps of hydrothermal synthesis.

Sample preparation involves the removal of dirt, grease, and other contaminants from substrate surfaces in order to improve the nanocoating adhesion. A seed layer is used to promote the oriented growth of nanostructures, homogenise the nanostructured coating and improve its adhesion to the surface. The seed layer can be obtained in different ways: magnetron sputtering, electrolytic deposition, etc. However, one of the most popular ways is to use a solution of zinc acetate $Zn(CH_3COOH)_2$ in ethanol which forms a gel-like substance that can be used to coat surfaces of any shape and size and after annealing due to baking to the surface has good adhesion. Equimolar aqueous solutions of zinc nitrate $Zn(NO_3)_2$ and hexamethylenetetramine (HMTA; $C_6H_{12}N_4$) are commonly utilized for the subsequent synthesis of ZnO nanostructures. In this method, $Zn(NO_3)_2$ acts as a source of Zn^{2+} ions, while water functions as a source of O^{2-} ions. HMTA, on the other hand, is a slow-decomposing weak base that produces a slightly alkaline environment in the solution, providing the necessary amount of OH^- ions. When a substrate is immersed in such a solution, the growth of the most prevalent ZnO nanostructure morphology, hexagonal nanorods, occurs.

The following chemical reactions take place during the growth process: [41]

$$C_6H_{12}N_4+6H_2O\rightarrow 6HCHO+4NH_3 \quad (1)$$

$$NH_3+H_2O\rightarrow NH_4^++OH^- \quad (2)$$

$$2OH^-+Zn^{2+}\leftrightarrow Zn(OH)_2 \quad (3)$$

$$Zn(OH)_2\leftrightarrow ZnO+H_2O \quad (4)$$

Other morphologies of ZnO nanostructures can be obtained by changing the composition of the solution and altering the synthesis parameters (growth temperature, time, solution concentration and pH). More details on the influence of various factors on the morphology of nanostructures can be found in our previous articles [42]–[44].

Sometimes the purpose of an experiment requires the surface not to be coated homogeneously over its entire area but rather selectively – maintaining some untreated substrate areas. This issue is especially relevant in the processes of manufacturing various electrodes and sensors.

Selective coatings can be achieved in different ways. First, this can be accomplished by applying the nanostructures only in the specified area using the microprinting method [45]–[48], contact rollers [49], [50], flexographic printing [51], [52] or various types of stamps [53]–[55] and soft moulds (micro-moulds) [56], [57].

In the second case, selective deposition of the seed layer occurs, followed by hydrothermal growth [25], [38], [41]. The publications mention two important factors that greatly affect the quality of selective area

growth that have to be taken into account: the effect of thermal convection in aqueous solutions and the "coffee stain" effect.

Thermal convection can be described as a vertically directed circular motion of a hot fluid that results from differences in density in different parts of the vessel caused by differences in temperature [58], [59]. A large number of ZnO nuclei are generated in the growth solution during the synthesis process. Some of them participate in the formation and growth process of nanostructures, which mostly take place on the pre-coated ZnO seed layer, which is an energetically favourable place. Particles that do not participate in the growth process fall into the precipitate and are drifted into the solution volume by convection flows. When the drifting particles reach the substrate, they can adhere to it and form chaotically oriented second-generation seeds, which cause nanostructure growth in unintended places. To avoid this effect, the sample position in the vessel is very important. The most favourable sample position is in the upper part of the vessel, with the seed-cowered side facing downward. In this case, the minimum contact of the working surface with the nanoparticles drifting in the solution is ensured, and the entire sediment, which cannot be avoided, settles on the non-working surface of the sample. Correspondingly, the most unpropitious position of the sample at the bottom of the vessel since the largest amount of sediment is concentrated there as it settles from the solution under the action of gravity [48]. It should be noted that the correct positioning of the sample reduces the negative effect of the convection flow, but it does not completely eliminate the growth of unwanted nanostructures, so an effective solution to this problem is the use of an additional protective barrier that separates the sample from drifting ZnO nanoparticles and homogenises the solution flow near the sample [47], [60].

The second effect that significantly affects the homogeneity of the nanostructured coating is the "coffee stain" effect [61], [62] and it can be explained as follows. When a drop of the solution reaches the substrate surface, it takes the form of a hemisphere. As there are also solid particles in the drop of solution during the synthesis process, the contact line is fixed, and the temperature in the lower part of the drop is higher than in the upper part. Due to the temperature gradient, the evaporation in some parts of the droplet becomes uneven, which leads to thermocapillary convection and the transfer of particles to the more intense evaporation regions. As a result, particles aggregate on the edge of the former droplet creating a ring-like pattern on the substrate surface [47], [63].

The "coffee stain" effect is observed not only in the case of the selective area growth but also in the case of uniform coating over the entire substrate surface. It occurs when the seeds produced by the acetate route are unevenly distributed over the surface and form annular lines with a high seed density delimiting areas with a low seed density. As a result, it leads to uneven distribution of hydrothermally grown ZnO nanostructures; both cluttered and almost empty areas of irregular shape are observed.

One of the most effective solutions for seed layer surface homogenisation is to use a pre-heated substrate or supply additional heat to the substrate during zinc acetate application. The increased substrate temperature increases the evaporation rate of the solution droplet, which at high values is capable of bypassing the flow of thermocapillary convection directed from the centre to the edge of the drop. Thus, the solution evaporates before the particles begin to collectively migrate towards the edges, allowing them to distribute evenly over the surface.

Another possibility to obtain a selective coating is to use a laser for the selective thermal decomposition of zinc acetate to obtain the seed layer, followed by hydrothermal synthesis of nanostructures. Laser radiation can be used as an effective source of local surface heating, replacing the thermal annealing of a whole sample and thus ensuring area-selective thermal decomposition of zinc acetate and the growth of zinc oxide precursors only in the required place [64], [65]. In some articles, laser irradiation is used not only for producing nanoparticle seeds but also for the nanostructure growth process, completely replacing standard hydrothermal synthesis in the furnace. In this case, the sample surface is irradiated through the working solution layer, and the synthesis of nanostructures takes place only in the heated area. This method ensures a high coating selectivity because in sample areas where the laser beam does not enter, neither the surface nor the solution is heated to the temperature required for hydrothermal synthesis, so the growth of undesirable nanostructures is not possible [66], [67]. The integration of the laser into a computer-controlled scanning system makes it possible to obtain area selective patterns of ZnO seeds and subsequently selective patterning of ZnO nanostructure arrays of any size and shape on the various surfaces.

Sometimes, especially in cases where it is necessary to coat different shapes of metallic electrodes with a nanostructured layer, leaving the space between the electrodes free of nanostructures, it is convenient to apply the electrochemical deposition method. The electrochemical deposition process combines hydrothermal synthesis at a low temperature (<90 °C) and an electrochemical process. The main difference of this method from hydrothermal synthesis is that nanostructures grow only on conductive surfaces where the electrical potential is applied, thus providing area selective deposition and the possibility of obtaining nanostructured electrodes of any shape with element sizes in the range of a few microns.

In the first stage, the precursors dissolve in water and form an electrolyte that contains zinc cations and various types of anions, the chemical composition of which depends on the chosen precursor. In the next step, the oxygen reduction process leads to the formation of hydroxide OH^- ions on the sample's surface, which further interact with the Zn^{2+} ions in solution and generate zinc hydroxide particles. The process ends with the conversion of zinc hydroxide into zinc oxide at an elevated temperature typical of hydrothermal growth.

Precursors based on zinc chloride [68], [69] and zinc nitrate [70], [71] are mainly used. Nitrate-based precursors have one significant advantage: they serve as a source of anions and cations. Nitrate-based precursor reactions can be written as follows.

$$NO_3^- + H_2O + 2e \rightarrow NO_2^- + 2OH^- \quad (5)$$

$$Zn^{2+} 2OH^- \leftrightarrow Zn(OH)_2 \quad (6)$$

$$Zn(OH)_2 \xrightarrow{\text{temperature}} ZnO + H_2O \quad (7)$$

The size and morphology of the resulting nanostructures can be controlled by different additives. For example, [72], [73] indicate that the addition of an electrolyte containing Cl- ions results in the growth of 2D ZnO nanoplates instead of ZnO nanorods. The effect can be explained by the fact that Cl^- ions are mostly adsorbed on the polar ZnO (0002) surfaces of nanowires, blocking growth in the vertical direction and stimulating radial growth in the $\{10\bar{1}0\}$ plane direction. A similar effect is achieved by adding SO_4^{2-} and CH_3COO^- ions to the electrolyte solution [68].

The addition of nitrate-containing support electrolytes (e.g., $NaNO_3$) helps to increase the concentration of OH^- ions without changing the concentration of Zn^{2+} ions and thus change the aspect ratio of the nanostructures, accelerating the growth process similar to hydrothermal growth at elevated pH.

In this article, several methods that allow obtaining area-selective patterns of a ZnO nanorod array are considered. The process of hydrothermal synthesis of rod-shaped nanostructures, as well as the phenomena that affect the uniformity and selectivity of the resulting coating, are considered in detail. The proposed synthesis methods can be used to obtain nanostructured patterns for various purposes. In particular, they can be relevant for the manufacture of electrodes of various shapes, as well as for applications in sensorics.

2. MATERIALS AND METHODS

2.1. Hydrothermal Growth of Patterned ZnO Nanostructure Arrays Based on Selectively Applied Zn Acetate Seeds

In order to investigate the peculiarities of selective growth of ZnO nanostructures, the following samples were prepared. Glass microscope slides (76 x 26 mm) were coated with a 120 nm thick Cr layer, and a 25 mM zinc acetate ethanol solution was applied dropwise to them using a sharp needle. The samples were then annealed for 30 min at 350 ºC and hydrothermally overgrown with ZnO nanoneedles. The composition of the growth solution was 0.025 M $Zn(NO_3)_2$ and 0.05 M HMTA. The growth process took place in a programmable Linn High Therm oven for 1.5 hours at 90 ºC.

In order to ensure additional cleanliness of the sample surface, the glass substrates and the working solution were heated to 90 ºC in an oven separately. This manipulation prevents the condensation of (growth) particles on a cold surface and their accumulation in non-seeded areas, thus preventing the growth of nanostructures in unintended places.

To study the "coffee stain" effect, two groups of samples were obtained. In the first case, an acetate solution was applied onto a substrate at a room temperature, and in the second case, it was applied to a preheated substrate. Furthermore, hydrothermal growth of nanostructures was performed based on the parameters mentioned above.

To evaluate the effect of the protective screen on the growth process of nanostructures, a series of samples were prepared. Some of them were grown as usual by orienting the seed layer facing down in the solution, and some of the samples were grown by enclosing the substrate from the bottom with another glass in such a way that a gap of 2–3 mm formed between the substrate and the screen glass.

2.2. Use of Laser for Area Selective Thermal Decomposition of Zinc Acetate Followed by Hydrothermal Growth

Area selective thermal decomposition of zinc acetate was performed using a Coherent Verdi V-6 532 nm laser integrated with a computer-controlled device with a

mechanised sample positioning platform, which allows control of the trajectory of the laser beam over the sample surface and provides fully automated sample exposure with an accuracy of ± 0.125 μm.

A standard microscope slide was used as a substrate. On top of the slide, a 160 nm thin Cr layer (an effective laser radiation absorbing layer that causes a local temperature increase in the photothermal process) was deposited by magnetron sputtering. Next, a solution of 5 mM Zn $Zn(CH_3COO)_2*2H_2O$ in ethanol was spin-coated on the Cr layer. After complete evaporation of ethanol in air, the sample was irradiated with a laser according to a given trajectory. Scanning was performed at a speed of 55 mm/min with a laser power of - 60 mW.

After irradiation, the samples were subjected to a hydrothermal ZnO growth process.

Samples were placed in equimolar 0.1M solutions of $Zn(NO_3)_2$ and HMTA for 3 h at 90 ºC. At the end of the growth, the samples were rinsed with distilled water. One of them was removed from the glass after rinsing and air-dried. The other was placed in a glass of distilled water and exposed to ultrasound for 2 min to remove unwanted nanostructures that appeared in unirradiated areas and were less bound to the surface compared to nanostructures obtained on ZnO seedlings.

2.3. Electrodeposition Method

Microscope slides were used as the base for a 120 nm thick Cr layer that was deposited by magnetron sputtering through a metal mask to obtain planar circular-shaped electrodes. The ZnO seed layer was produced from an electrolytically coated Zn layer (0.1 M $Zn(NO_3)_2$, j = 90 μA/cm^2, t = 5 min) with subsequent annealing at 350 ºC for 30 min in air, with the aim of oxidising zinc to zinc oxide.

The obtained sample was fixed in a holder, placed in a container containing a growth solution with a lid and connected to the negative pole of the power source. A glass plate covered with a thin Au layer of the same size was used as the cathode. It was fixed in the same holder at a distance of ≈ 1 cm from the anode. The container was placed in the furnace at temperature T = 80 ºC for 2.5 h. Current density, j = 90 μA/cm^2, and voltage, U = 2 V, were maintained during the growth process.

As a working solution, a 0.005 M $Zn(NO_3)_2$ + 0.1 M $NaNO_3$ aqueous solution was used to obtain ZnO nanoneedles and a 0.05 M $Zn(NO_3)_2$ + 0.1 M KCl aqueous solution to obtain ZnO nanoplates.

After the end of the growth process, samples coated with nanostructures were rinsed with distilled water and placed in a furnace at 90 ˚C for 1 h in order to get rid of the remaining solution.

The surface morphology of the processed samples was investigated using a scanning electron microscope (Tescan-Vega II LMU). The chemical composition of the samples was determined by an INCA x-act energy dispersive spectrometer (Oxford Instruments). To determine the structural and phase composition, the XRD spectra were recorded on a Cu Kα (λ = 1.543Å) diffractometer (Rigaku SmartLab) with parallel beam geometry using an additional Ge(220)×2 monochromator.

3. RESULTS AND DISCUSSION

3.1. Selective Application of Zn Acetate Seeds Followed by Hydrothermal Growth

Figure 2 shows the XRD and EDS results of the obtained nanostructures. The resulting nanostructures are well-ordered perpendicular to the substrate and have a high degree of crystallinity. No crystalline phases other than ZnO were detected. Microanalysis results also confirm that the samples are free of chemical impurities.

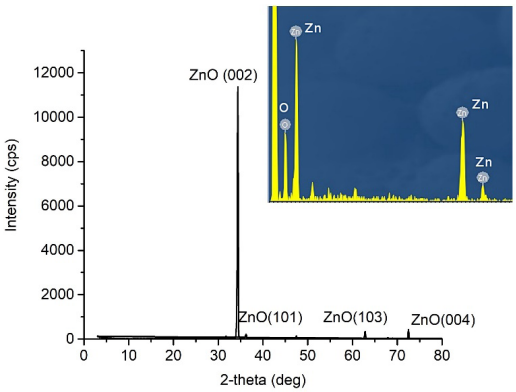

Fig. 2. XRD and EDS microanalysis results of hydrothermally synthesised ZnO nanostructures.

The deviation from the equimolarity of the solution to an excess of HMTA provides an increase in the pH of the solution due to the predominance of OH^- ions and, as a result, an increase in the reaction rate. This allows for reducing the growth time of nanostructures from the standard 3 h [51], to 1.5-2 h. Consequently, reducing the growth time also reduces the probability of unwanted nanostructures appearing.

The results of the analysis of the "coffee stain" effect are summarised in Fig. 3.

Application of zinc acetate solution onto a room temperature substrate leads to the appearance of a ring-shaped formation with a high density of seeds at the edges and sparse, chaotically located seed islets inside the spot. Such a distribution of seeds also determines the growth and distribution of future nanostructures. Figure 3a shows an overview of the droplet after the growth process has ended. As seen in Fig. 3b, the seeding compaction on the edge of the drop contributes to the appearance of densely spaced and vertically aligned ZnO nanoneedles. It should be noted that the width of these bands is relatively small, and when approaching the centre of the drop, the density of the nuclei decreases, and their distribution becomes more uneven. Reduced density of seeds leads to the centre of the droplet being filled with radially arranged 3D ZnO nano-urchins grown on islet formations of seeds (Fig. 3c).

A completely different situation is observed when zinc acetate solution is dropped onto a preheated substrate. Heating the substrate to 100 ºC leads to accelerated evaporation of ethanol compared to the previous case, as evidenced by a fourfold reduction in droplet diameter, thereby reducing the effect of thermocapillary convection. As shown in Fig. 3d, the hydrothermal growth results in a much more homogeneous coating consisting mostly of fine, vertically oriented nanoneedles (Fig. 3e) interrupted in rare areas by densely placed islands of nanoneedles.

The heating of the substrate is also relevant in cases where selectivity is not required, and growth takes place by applying zinc acetate as a continuous layer. In this case, the seed layer becomes more homogeneous, and the distribution of seeds is more even because the areas of compacted seeds, formed as a result of the flow of solution,

disappear. Consequently, the subsequently grown nanostructured coating is also homogeneous.

In Figure 3g, the upper horizontal row illustrates the process of liquid evaporation in a drop in the presence of convection flows. Arrows in the first figure indicate the directions of thermocapillary flows and the presence of areas of thermal inhomogeneities in the droplet. Thus, at the top of the drop, the temperature is lower than at its base, which causes a difference in liquid density and the formation of thermocapillary flows. The middle row illustrates the evaporation process at room temperature for the case when solid particles are present in solution. It can be seen that as the liquid evaporates, the particles are distributed unevenly in solution, forming characteristic dense areas along the edges and rarefied spots in the centre.

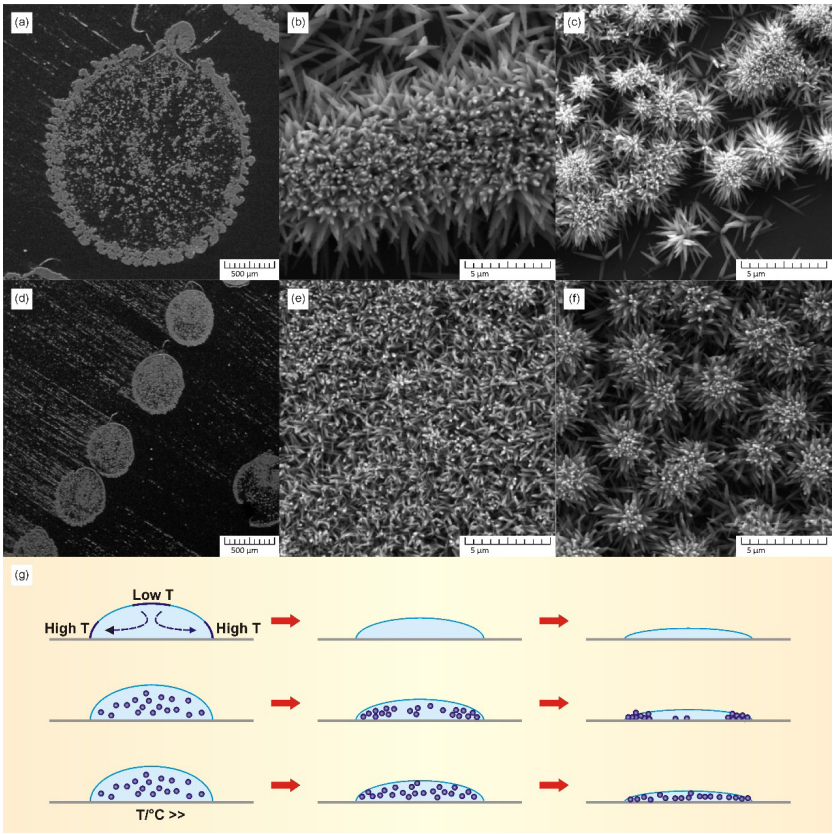

Fig. 3. Analysis of the "coffee stain" effect, where (a), (b), and (c) nanostructures were obtained by applying ZnO precursors on a room-temperature substrate, and (d), (e), and (f) on a pre-heated substrate. Hydrothermal synthesis was carried out in 0.025 M $Zn(NO_3)_2$ and 0.05 M HMTA aqueous solutions at 90 ºC for 1.5 h. (g) Graphic illustration of the coffee stain effect formation process [47].

The bottom row illustrates the evaporation process taking place at an elevated temperature compared to the previous case. In this case, the middle picture shows that the thermocapillary flows do not affect the movement of the particles and they are evenly distributed in the droplet. The results of the experiment using the protective screen are summarised in Fig. 4. As seen in Fig. 4a, if a screen is not used, the

growth of nanostructures occurs both on the seeds layer (droplet) and on the clean glass around the droplet. By placing an additional screen, the growth of nanostructures outside the zinc acetate droplets is suppressed and almost unobservable (Fig. 4b).

Repeating the experiment by changing synthesis parameters (temperature, time, pH of the solution), it was found that in all cases, the result with the application of the screen was many times better than without it.

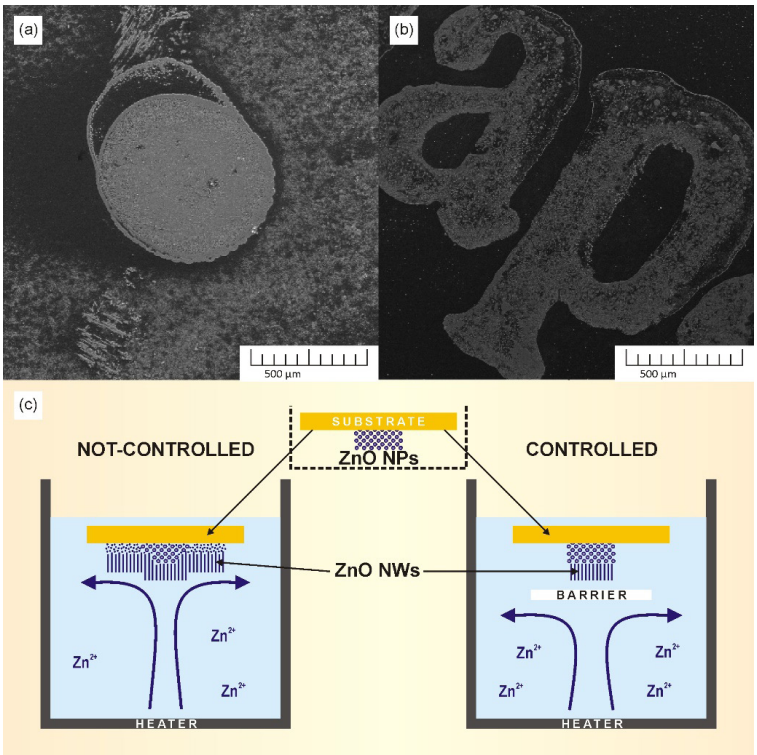

Fig. 4. The effect of the protective screen on the selective coating process, where (a) the growth of nanostructures occurred without and (b) with the protective screen, c) a graphical scheme of the process [60].

This experiment shows that the use of a screen does indeed restrict convection currents and homogenise the solution near the sample while limiting the contact of the sample with the suspension of unwanted sediment particles. This procedure significantly increases the selectivity of the coating and positively affects the quality of the sample.

3.2. Selective Laser Decomposition of Zinc Acetate Followed by Hydrothermal Growth

The stamping method used in the previous chapter to apply zinc acetate to form a nucleation layer is easy to use but has a number of disadvantages. This method is great for creating large patterns, but it is not accurate enough for sharp micron-sized lines. In this case, the laser annealing method proved to be very effective in obtaining a seed layer with a complex shape. Figure 5e shows the process of obtaining nanostructures. Zinc acetate was applied in a continuous layer on a substrate coated with a metal layer to

absorb the temperature. The sample was then irradiated with a laser. Accordingly, the temperature necessary for the thermal conversion of zinc acetate to zinc oxide was reached in places subjected to laser treatment, and a seed layer was formed. The remaining regions of the sample were not subjected to heating; therefore, the zinc acetate in them remained unannealed. Next, the growth of zinc oxide nanostructures occurs according to the standard protocol of hydrothermal synthesis. At the end of the synthesis, the sample is subjected to additional processing in an ultrasonic bath in order to remove parasitic microrods formed in the areas with non-irradiated acetate. As a result, after washing, a nanostructured pattern of a given shape is obtained corresponding to the trajectory of the laser movement.

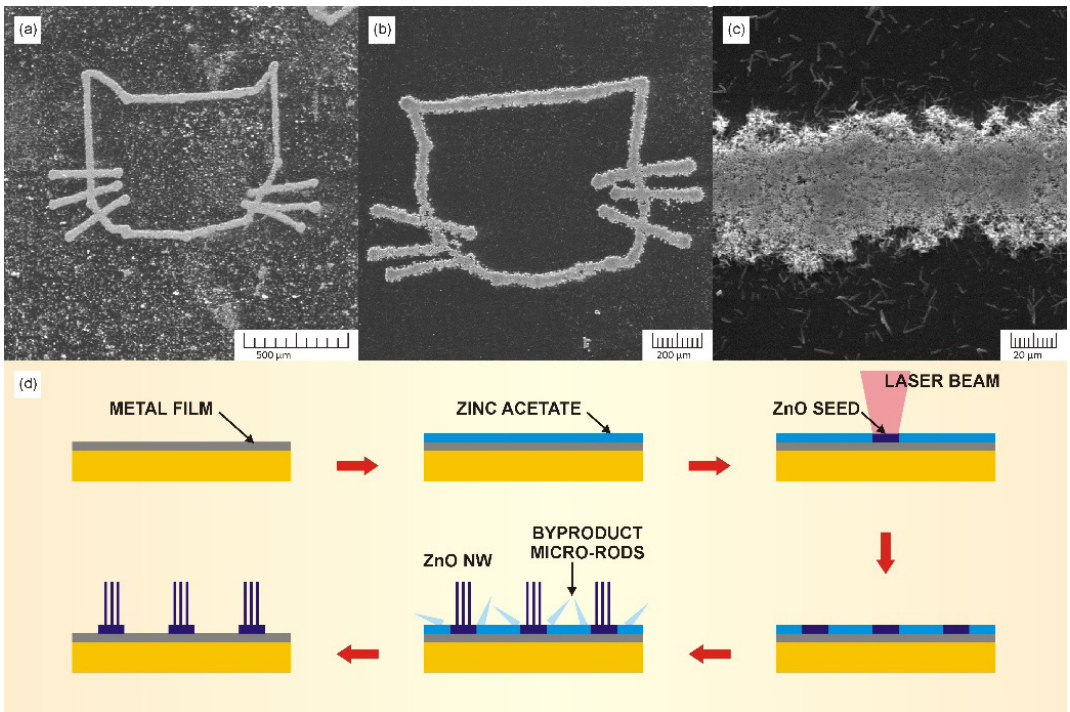

Fig. 5. ZnO nanostructures obtained on areas of selectively laser-assisted seeds with a subsequent hydrothermal growth process in an equimolar working solution (a-c), graphical scheme of the experiment (d) [64].

Most of the articles indicate that even if unwanted by-product microrods appear in places not irradiated with a laser during the nucleation process, their adhesion to the surface is very low since they grow in areas of thermally untreated zinc acetate, and zinc oxide seeds are necessary for the formation of stable adhesion. Such parasitic formations were removed by processing samples in an ultrasonic bath. All nanostructures that do not have sufficient adhesion to the surface are removed, leaving only a clear pattern formed at the site of laser exposure. However, in our case, the situation is different. Practice proves that the efficiency of the method is about 90%. After the ultrasonic bath, the sample's surface becomes significantly cleaner; however, individual unwanted needles can be observed on it. Most likely, the formation of these needles

is related to the good adhesion properties of the Cr thin film. In this case, Cr surface defects become crystallisation centres and induce the formation of nanostructures with adhesion comparable to that provided by the ZnO seed layer.

In order to reduce the number of undesirable nanostructures, a number of articles advise adhering to higher synthesis temperatures or increasing the pH level of the solution when choosing synthesis parameters. This makes it possible to obtain nanostructures of the desired size in a much shorter time, which contributes to a decrease in the density of nanostructures in places without nuclei since such growth is energetically unfavourable.

Our previous studies have shown that the pH level of the working solution and the growth rate of nanostructures can be increased by using a non-equimolar solution (by decreasing the amount of zinc nitrate and increasing the amount of HMTA).

Figure 6 shows the SEM results of a sample obtained in a non-equimolar working solution after subsequent rinsing in an ultrasonic bath after the growth process.

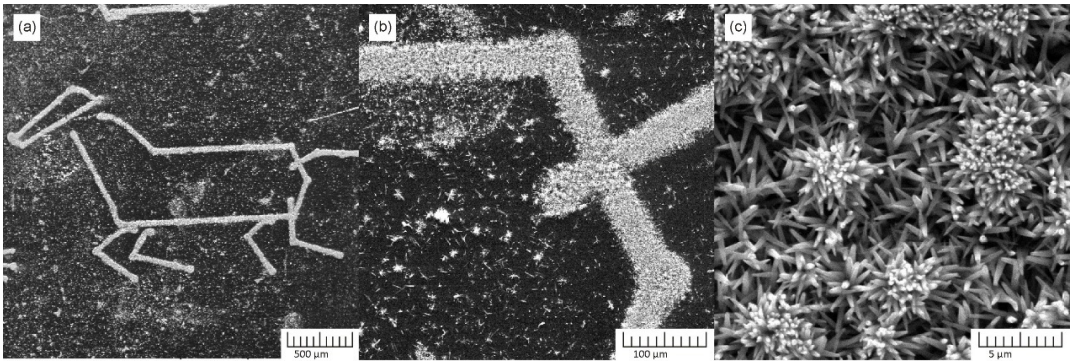

Fig. 6. ZnO nanostructures (at different magnifications) obtained on selectively laser-assisted seeds with the subsequent hydrothermal growth process in a working solution with an increased pH value.

As shown in Fig. 6a-c, in cases where nanostructures grow at increased pH, ultrasonic rinsing does not help to get rid of unwanted nanostructures. In this case, the contamination in the non-irradiated areas is much higher compared to the previous case, where growth took place in an equimolar working solution. Most likely, this is related to the stimulation and acceleration of the growth process of nanostructures. Under the influence of increased pH, the chemical reaction proceeds faster, and the required amount of OH ions is generated in a much shorter time. As the reaction speed increases, so does the speed of the nucleation process. A large number of ε-$Zn(OH)_2$ particles is massively generated in the volume of the solution. These particles form spherical aggregates with the aim of minimising the internal energy. As the number of surface nucleation bonds is small, a greater part of these aggregates fall into the sediment and form seeds which precipitate from solution and are fixed in arbitrary places, regardless of the presence of the seed layer. Comparing Fig. 6 and Fig. 5, it can be seen that in the case of an equimolar solution, the off-line space is much cleaner from contamination than a non-equimolar solution because the growth of nanostructures with a higher probability occurs only in energetically more favourable places (in this case on ZnO seeds).

Also, the change of other growth param-

eters (temperature, time) did not cause any significant external changes.

To completely get rid of the nanostructures formed outside the set line, a protective screen must be used during the growth process.

Within the framework of this experiment, we studied the effect of laser radiation power on the form of nuclei obtained from zinc acetate and, as a consequence, on the form of nanostructures obtained as a result of subsequent growth.

The experiment was repeated several times, changing the laser power in the range of 50-160 mW. After the end of the growth process, it could be concluded that the laser power increase leads to an increase in the width of the obtained line. The process is related to the heat transfer in metal, and with increasing the laser power, a larger area of zinc acetate is exposed to the temperature. No changes in the morphology and dimensions of the nanostructures were detected.

If we evaluate the results as a whole, the obtained ZnO nanostructures based on laser-obtained seeds do not differ in terms of morphology or size from the nanostructures obtained on zinc acetate seeds annealed in the furnace. It can be concluded that the parameters of the ZnO seeds are determined by the individual properties of the zinc acetate; the heat source is not important. The only necessary condition is exceeding the calcination temperature threshold (≈100-150 ºC); a further increase in temperature does not determine a change in the parameters of the seeds (obtainable nanostructures).

However, the use of a laser for the production of nuclei makes it possible to create unique and often very complex nanostructured patterns with elements several micrometres in size and clear lines with well-drawn boundaries, which is technically impossible to achieve when using the method of applying zinc acetate by dipping or stamping followed by thermal annealing.

3.3. Electrochemical Deposition

If it is necessary to coat metal electrodes with nanostructures, it is sometimes advisable to use the method of electrochemical deposition, which makes it possible to obtain a selective coating without the use of a seed layer.

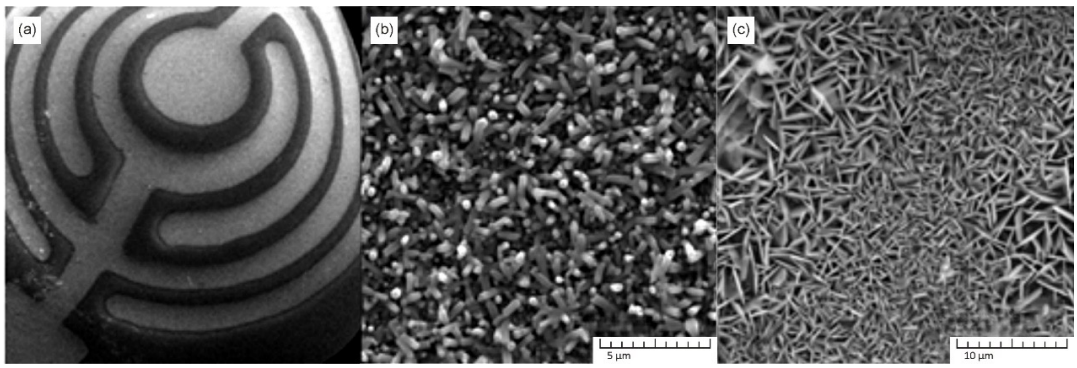

Fig. 7. ZnO nanostructures obtained by electrochemical deposition method. SEM overview of overgrown electrode (a), nanoneedles (b), nanoplates (c).

As shown in Fig. 7a, the growth of nanostructures is observed only on the electrodes: the interelectrode space is completely free of undesired nanostructures. The coating of both ZnO nanoneedles (Fig. 7b) and nanoplates (Fig. 7c) is dense and homoge-

neous. The crystallites of both morphologies are very similar in shape and size to those obtained by hydrothermal synthesis.

It should be noted that, unlike a classical hydrothermal synthesis, the electrochemical deposition method requires a definition of precise experimental conditions, such as potentials, reactants, concentrations, pH, deposition times, etc. Even the smallest deviation from the optimum growth process affects the quality of the sample surface (an amorphous layer can be formed instead of nanostructures). Very strict requirements are imposed on the electric conductivity of the electrode material, and the optimal growth parameters must be determined for each kind of substrate (unlike hydrothermal synthesis, where the result is predictable for all surface types and does not depend on the substrate material).

Another factor to consider is the electrochemical corrosion of the forced contacts. Although the contact area of the electrodes is not in direct contact with the working solution, they are exposed to water vapour for a long time because growth takes place at a relatively high temperature (80 ºC). However, despite all the complicating factors, the method proved to be very effective. In cases where it is necessary to cover small electrodes with nanostructures and keep the outside electrode space clean, this method is very useful, accurate, and fast. This method becomes especially relevant when, for a number of reasons, the deposition of nuclei is impossible or it is necessary to obtain oxides of different metals on one electrode.

4. CONCLUSIONS

All of the methods discussed in the article provide for a good selective area growth of nanostructures and allow the formation of intricately shaped nanostructured patterns on different types of surfaces.

Regardless of the method of obtaining the ZnO seeds, using an extra cover screen helps restrict the surface from the effects of convection flows of the solution and reduces the likelihood of nanostructures outside the patterned area.

For the selective patterning of the zinc oxide seed layer by using the stamping transfer process, it is recommended to apply zinc acetate on a preheated substrate to reduce the thermocapillary effect and homogenise the coating.

The morphology of the obtained ZnO nanostructures does not depend on the methods of obtaining seeds: decomposition of zinc acetate during annealing in a furnace or selective laser decomposition. The only condition required is that the calcination temperature threshold is exceeded (≈100–150 °C). A further increase in temperature does not determine the change of seed parameters (obtainable nanostructures). Thus, the heat source is not significant.

Of all the above-mentioned methods, the electrochemical synthesis method has the highest requirements for observing synthesis parameters and surface quality. It is sensitive to current and temperature changes during the synthesis process and can only be used for coating conductive surfaces. However, this method is optimal in cases where electrodes of various shapes have to be covered with nanostructures. It is fast because the growth takes place immediately over the entire area, and it is precise because it allows covering elements in the range of a few microns.

ACKNOWLEDGEMENTS

The research has been supported by ERDF project No. 1.1.1.2/VIAA/4/20/743 "Development of Nanomaterial-based Electrochemical Sensor for Detection of Hydrogen Peroxide".

REFERENCES

1. Santos, M. S., Marques Lameirinhas, R. A., N. Torres, J. P., P. Fernandes, J. F., & Correia V. Bernardo, C. P. (2023). Nanostructures for Solar Energy Harvesting. *Micromachines*, *14*, 364. doi:10.3390/mi14020364.
2. Sidorenko, A. S. (2020). Functional Nanostructures for Electronics, Spintronics and Sensors. *Beilstein J. Nanotechnol., 11*, 1704–1706. doi: 10.3762/bjnano.11.152.
3. Mitchell, M. J., Billingsley, M. M., Haley, R. M., Wechsler, M. E., Peppas, N. A., & Langer, R. (2021). Engineering Precision Nanoparticles for Drug Delivery. *Nat. Rev. Drug Discov., 20*, 101–124. doi: 10.1038/s41573-020-0090-8.
4. Arredondo-Ochoa, T., & Silva-Martínez, G. A. (2022). Microemulsion Based Nanostructures for Drug Delivery. *Front. Nanotechnol., 3,* 753947. doi: 10.3389/fnano.2021.753947.
5. Gautam, Y. K., Sharma, K., Tyagi, S., Ambedkar, A. K., Chaudhary, M., & Pal Singh, B. (2021). Nanostructured Metal Oxide Semiconductor-Based Sensors for Greenhouse Gas Detection: Progress and Challenges. *R. Soc. Open Sci., 8*, 201324. doi: 10.1098/rsos.201324.
6. Gorup, L. F., Sequinel, T., Akucevicius, G. W., Pinto, A. H., Biasotto, G., Ramesar, N., de Arruda, E., G., R., … & Camargo, E. R. (2021). Nanostructured Gas Sensors in Smart Manufacturing. *Nanosensors for Smart Manufacturing, Elsevier,* 445–485. doi.org/10.1016/B978-0-12-823358-0.00022-8.
7. Chowdhury, N. K., & Bhowmik, B. (2021). Micro/Nanostructured Gas Sensors: The Physics behind the Nanostructure Growth, Sensing and Selectivity Mechanisms. *Nanoscale Adv., 3,* 73–93. doi: 10.1039/d0na00552e.
8. Karabulut, G., Beköz Üllen, N., & Karakuş, S. (2022). Nanostructures in Biosensors: Development and Applications. *Biomedical Engineering. IntechOpen.* doi: 10.5772/intechopen.108508.
9. Varnakavi Naresh, V., & Lee, N. (2021). A Review on Biosensors and Recent Development of Nanostructured Materials-Enabled Biosensors. *Sensors (Basel), 21* (4), 1109. doi: 10.3390/s21041109.
10. Bertel, L., Miranda, D. A., & García-Martín, J. M. (2021). Nanostructured Titanium Dioxide Surfaces for Electrochemical Biosensing. *Sensors, 21*, 6167. doi: 10.3390/s21186167.
11. Nagal, V., Masrat, S., Khan, M., Alam, S., Ahmad, A.; Alshammari, M. B., ... & Ahmad, R. (2023). Highly Sensitive Electrochemical Non-Enzymatic Uric Acid Sensor Based on Cobalt Oxide Puffy Balls-like Nanostructure. *Biosensors, 13*, 375. doi: 10.3390/bios13030375.
12. Abdel-Karim, R., Reda, Y., & Abdel-Fattah, A. (2020). Review—Nanostructured Materials-Based Nanosensors. *J. Electrochem. Soc., 167*, 037554. doi: 10.1149/1945-7111/ab67aa.
13. Macagnano, A., & Avossa, J. (2020). Chapter 11 – Nanostructured composite materials for advanced chemical sensors. In *Advances in Nanostructured Materials and Nanopatterning Technologies: Applications for Healthcare, Environment and Energy*, *Elsevier,* (pp. 297–332). doi: 10.1016/b978-0-12-816865-3.00011-1.

14. Gerbreders, V., Krasovska, M., Mihailova, I., Ogurcovs, A., Sledevskis, E., Gerbreders, A., … & Plaksenkova, I. (2021). Nanostructure-Based Electrochemical Sensor: Glyphosate Detection and the Analysis of Genetic Changes in Rye DNA. *Surfaces and Interfaces, 26*, 101332. doi: 10.1016/j.surfin.2021.101332.
15. Nagal, V., Tuba, T., Kumar, V., Alam, S., Ahmad, A., Alshammari, M. B., … & Ahmad, R. (2022). A Non-enzymatic Electrochemical Sensor Composed of Nano-berry Shaped Cobalt Oxide Nanostructures on a Glassy Carbon Electrode for Uric Acid Detection. *New J. Chem., 46*, 12333–12341. doi: 10.1039/D2NJ01961B.
16. Fall, B., Sall, D. D., Hémadi, M., Diaw, A. K. D., Fall, M., Randriamahazaka, H., & Thomas, S. (2023). Highly Efficient Non-enzymatic Electrochemical Glucose Sensor Based on Carbon Nanotubes Functionalized by Molybdenum Disulfide and Decorated with Nickel Nanoparticles (GCE/CNT/MoS_2/NiNPs). *Sens. Actuat. Rep., 5*, 100136. doi: 10.1016/j.snr.2022.100136.
17. Singer, N., Pillai, R. G., Johnson, A. I. D., Harris, K. D., & Jemere, A. B. (2020). Nanostructured Nickel Oxide Electrodes for Non-enzymatic Electrochemical Glucose Sensing. *Microchimica Acta, 187* (4), 187–196. doi: 10.1007/s00604-020-4171-5.
18. Echarri-Giacchi, M., & Martín-Martínez J. M. (2022). Efficient Physical Mixing of Small Amounts of Nanosilica Dispersion and Waterborne Polyurethane by Using Mild Stirring Conditions. *Polymers, 14*(23), 5136. doi: 10.3390/polym14235136.
19. Liao, M.-J., & Duan, L.-Q. (2020). Dependencies of Surface Condensation on the Wettability and Nanostructure Size Differences. *Nanomaterials (Basel)., 10* (9), 1831. doi: 10.3390/nano10091831.
20. Shen, J.-F., Wu, C.-M., Mo, D.-M., & Lio, Y.-R. (2023). Molecular Investigation on the Formation and Transition of Condensation Mode on the Surface with Nanostructure. *J. Mol. Liq., 369*, 120848. doi: 10.1016/j.molliq.2022.120848.
21. Jinming Liu, J., He, S.- H., & Wang, J.- P. (2020). High-Yield Gas-Phase Condensation Synthesis of Nanoparticles to Enable a Wide Array of Applications. *ACS Appl. Nano Mater., 3* (8), 7942–7949. doi:10.1021/acsanm.0c01400.
22. Parauha, Y. R., Sahu, V., & Dhoble, S. J. (2021). Prospective of Combustion Method for Preparation of Nanomaterials: A Challenge. *Mater. Sci. Eng.: B, 267*, 115054. doi: 10.1016/j.mseb.2021.115054.
23. Wahyudiono, Kondo, H., Yamada, M., Takada, N., Machmudah, S., Kanda, H., & Goto, M. (2020). DC-Plasma over Aqueous Solution for the Synthesis of Titanium Dioxide Nanoparticles under Pressurized Argon. *ACS Omega, 5* (10), 5443–5451. doi: 10.1021/acsomega.0c00059.
24. Li, Z., Coll, M., Mundet, B., Chamorro, N., Vallès, F., Palau, A., Gazquez, J., ... & Obradors, X. (2019). Control of Nanostructure and Pinning Properties in Solution Deposited $YBa_2Cu_3O_{7-x}$ Nanocomposites with Preformed Perovskite Nanoparticles. *Sci. Rep., 9* (1)*,* 5828. doi: 10.1038/s41598-019-42291-x.
25. Gan, Y. X., Jayatissa, A. H., Yu, Z., Chen, X., & Li, M. (2020). Hydrothermal Synthesis of Nanomaterials. *J. Nanomater., 2020,* 8917013. doi: 10.1155/2020/8917013.
26. Bokov, D., Jalil, A. T., Chupradit, S., Suksatan, W., Ansari, M. J., Shewael, I. H., ... & Kianfar, E. (2021). Nanomaterial by Sol-Gel Method: Synthesis and Application. *Adv. Mater. Sci. Eng.*, *2021*, 5102014. doi: 10.1155/2021/5102014.
27. Navas, D., Fuentes, S., Castro-Alvarez, A., & Chavez-Angel, E. (2021). Review on Sol-Gel Synthesis of Perovskite and Oxide Nanomaterials. *Gels, 7*, 275. doi: 10.3390/gels7040275.
28. Yarbrough, R., Davis, K., Dawood, S., & Rathnayake, H. (2020). A Sol–Gel Synthesis to Prepare Size and Shape-Controlled Mesoporous Nanostructures of Binary (II–VI) Metal Oxides. *RSC Adv., 10*, 14134–14146. doi: 10.1039/D0RA01778G.
29. Domonkos, M., & Kromka, A. (2022). Nanosphere Lithography-Based Fabrication of Spherical Nanostructures and Verification of Their Hexagonal Symmetries by Image Analysis. *Symmetry, 14,* 2642. doi: 10.3390/sym14122642.

30. Jang, H.-I., Yoon, H.-S., Lee, T.-I., Lee, S., Kim, T.-S., Shim, J., & Park, J. H. (2020). Creation of Curved Nanostructures Using Soft-Materials-Derived Lithography. *Nanomaterials***,** *10 (12)*, 2414. doi: 10.3390/nano10122414.
31. Qu, J., Yang, W., Wu, T., Ren, W., Huang, J., Yu, H., … & CairneyJ. M. (2022). Atom Probe Specimen Preparation Methods for Nanoparticles. *Ultramicroscopy, 233*, 113420. doi: 10.1016/j.ultramic.2021.113420.
32. Shahzad, S., Javed, S., & Usman, M. (2021). A Review on Synthesis and Optoelectronic Applications of Nanostructured ZnO. *Front. Mater., 8*, 613825. doi: 10.3389/fmats.2021.613825.
33. Djurišić, A. B., Ng, A. M. C., & Chen, X. (2010). ZnO Nanostructures for Optoelectronics: Material Properties and Device Application. *Progress in Quantum Electronics, 34* (4), 191–259. doi:10.1016/j.pquantelec.2010.04.001.
34. Jiang, J., Pi, J., & Cai, J. (2018). The Advancing of Zinc Oxide Nanoparticles for Biomedical Applications. *Bioinorg. Chem. Appl., 2018,* 1062562. doi: 10.1155/2018/1062562.
35. Barman, A. (2015). Review on biocompatibility of ZnO nano particles. In Gupta, S., Bag, S., Ganguly, K., Sarkar, I., Biswas, P. (eds.) *Advancements of Medical Electronics. Lecture Notes in Bioengineering*. (pp. 343–352). Springer, New Delhi. doi: 10.1007/978-81-322-2256-9_32.
36. Oleshko, O., Husak, Y., Korniienko, V., Pshenychnyi, R., Varava, Y., Kalinkevich, O., ... & Pogorielov, M. (2020). Biocompatibility and Antibacterial Properties of ZnO-Incorporated Anodic Oxide Coatings on TiZrNb Alloy. *Nanomaterials (Basel), 10* (12), 2401. doi:10.3390/nano10122401.
37. Krishna, M. S., Sing, S., Batool, M., Fahmy, H. M., Seku, K., Shalan, A. E., … & Zafar, M. N. (2023). A Review on 2D-ZnO Nanostructure Based Biosensors: From Materials to Devices. *Mater. Adv., 4*, 320–354. doi: 10.1039/d2ma00878e.
38. Yang, G., & Park, S.-J. (2019). Conventional and Microwave Hydrothermal Synthesis and Application of Functional Materials: A Review. *Materials (Basel), 12* (7), 1177. doi:10.3390/ma12071177.
39. Adeleye, A. T., John, K. I., Adeleye, P. G., Akande, A. A., & Banjoko, O. O. (2021). One-dimensional Titanate Nanotube Materials: Heterogeneous Solid Catalysts for Sustainable Synthesis of Biofuel Precursors/Value-Added Chemicals – A Review. *J. Mater. Sci., 56* (5), 18391–18416. doi: 10.1007/s10853-021-06473-1.
40. Gerbreders, V., Krasovska, M., Sledevskis, E., Gerbreders, A., Mihailova, I., & Ogurcovs, A. (2020). Hydrothermal Synthesis of ZnO Nanostructures with Controllable Morphology Change. *CrystEngComm, 22*, 1346–1358. doi:10.1039/C9CE01556F.
41. Xu, S., Lao, C., Weintraub, B., & Wang, Z. L. (2008). Density-Controlled Growth of Aligned ZnO Nanowire Arrays by Seedless Chemical Approach on Smooth Surfaces. *J. Mater. Res., 23* (08)*,* 2072–2077*.* doi:10.1557/jmr.2008.0274.
42. Krasovska, M., Gerbreders, V., Paskevics, V., Ogurcovs, A., & Mihailova, I. (2015). Obtaining a Well-Aligned ZnO Nanotube Array Using the Hydrothermal Growth Method*. Latvian Journal of Physics and Technical Sciences, 52* (5)*,* 28–40*.* doi:10.1515/lpts-2015-0026.
43. Gerbreders, V., Krasovska, M., Mihailova, I., Sledevskis, E., Ogurcovs, A., Tamanis, E., … & Mizers, V. (2022). Morphology Influence on Wettability and Wetting Dynamics of ZnO Nanostructure Arrays. *Latvian Journal of Physics and Technical Sciences*, *59* (1), 30–43. doi: 10.2478/lpts-2022-0004.
44. Gerbreders, V., Krasovska, M., Mihailova, I., Ogurcovs, A., Sledevskis, E., Gerbreders, A., …& Plaksenkova, I. (2019). ZnO Nanostructure-Based Electrochemical Biosensor for Trichinella DNA Detection. *Sensing and Bio-Sensing Research, 23,* 100276*.* doi: 10.1016/j.sbsr.2019.100276.

45. Schürch, P., Osenberg, D., Testa, P., Bürki, G., Schwiedrzik, J., Michler, J., & Koelmans, W. W. (2023). Direct 3D Microprinting of Highly Conductive Gold Structures via Localized Electrodeposition. *Materials & Design*, *227*, 111780. doi: 10.1016/j.matdes.2023.111780.

46. Muldoon, K., Song, Y., Ahmad, Z., Chen, X., & Chang, M.-W. (2022). High Precision 3D Printing for Micro to Nano Scale Biomedical and Electronic Devices. *Micromachines (Basel), 13* (4), 642. doi: 10.3390/mi13040642.

47. Tsangarides, C. T., Ma, H., & Nathan, A. (2016). ZnO Nanowire Array Growth on Precisely Controlled Patterns of Inkjet-Printed Zinc Acetate at Low-Temperatures. *Nanoscale, 8*, 11760–11765. doi: 10.1039/c6nr02962k.

48. Wang, X., Sun, F., Huang, Y., Duan, Y., & Yin, Z. (2015). Patterned ZnO Nanorod Array/Gas Sensor by Mechanoelectrospinning-Assisted Selective Growth. *ChemComm, 51* (15), 3117–3120. doi:10.1039/c4cc08876j.

49. Lee, D., Tang, Y.-L., & Liu, S.-J. (2021). Fast Fabrication of Nanostructured Films Using Nanocolloid Lithography and UV Soft Mold Roller Embossing: Effects of Processing Parameters. *Polymers*, *13* (3), 405. doi:10.3390/polym13030405.

50. Lee, Y. H., Ke, K. C., Chang, N.W. & Yang, S. Y. (2018). Development of an UV Rolling System for Fabrication of Micro/Nano Structure on Polymeric Films Using a Gas-Roller-Sustained Seamless PDMS Mold. *Microsyst. Technol., 24* (7), 2941–2948. doi:10.1007/s00542-017-3683-3.

51. Fung, C. M., Lloyd, J. S., Samavat, S., Deganello, D., & Tenga, K. S. (2017). Facile Fabrication of Electrochemical ZnO Nanowire Glucose Biosensorusing Roll to Roll Printing Technique. *Sens. Actuat. B: Chem., 247*, 807–813. doi: 10.1016/j.snb.2017.03.105.

52. Kim, S., Sojoudi, H., Zhao, H., Mariappan, D., McKinley, G. H., Gleason, K. K., & Hart, A. J. (2016). Ultrathin High-Resolution Flexographic Printing Using Nanoporous Stamps. *Sci Adv., 2* (12), e1601660. doi: 10.1126/sciadv.1601660.

53. Kim, M., Oh, D., Kim, J., Jeong, M., Kim, H., Jung, C., ... & Ok, J. (2022). Facile Fabrication of Stretchable Photonic Ag Nanostructures by Soft-Contact Patterning of Ionic Ag Solution Coatings. *Nanophotonics*, *11* (11), 2693–2700. doi: 10.1515/nanoph-2021-0812.

54. Donie, Y. J., Yuan, Y., Allegro, I., Schackmar, F., Hossain, I. M., Huber, R., ... & Lemmer, U. (2022). A Self-Assembly Method for Tunable and Scalable Nano-Stamps: A Versatile Approach for Imprinting Nanostructures. *Adv. Mater. Technol., 7* (6), 2101008. doi: 10.1002/admt.202101008.

55. Taus, P., Prinz, A., Wanzenboeck, H. D., Schuller, P., Tsenov, A., Schinnerl, M., … & Muehlberger, M. (2021). Mastering of NIL Stamps with Undercut T-Shaped Features from Single Layer to Multilayer Stamps. *Nanomaterials*, *11*, 956. doi: 10.3390/nano11040956.

56. Liu, Z., Liu, N., & Schroers, J. (2022). Nanofabrication through Molding. *Progress Mater. Sci., 125,* 100891. doi: 10.1016/j.pmatsci.2021.100891.

57. Kang, H. W., Yeo, J., Hwang, J. O., Hong, S., Lee, P., Han, S. Y., … & Sung,H. J. (2011). Simple ZnO Nanowires Patterned Growth by Microcontact Printing for High Performance Field Emission Device. *J. Phys. Chem. C, 115* (23), 11435–11441. doi:10.1021/jp2019044.

58. Chakraborty, A., Orsini, A., Kar, J. P., Gatta, F., Khan, U., & Falconi, C. (2022). Ultra-efficient Thermo-convective Solution-Growth of Vertically Aligned ZnO Nanowires. *Nano Energy, 97*, 107167. doi: 10.1016/j.nanoen.2022.107167.

59. Simon Xia, S., Mostafavi, M., Alghazali, T., Sajad sadi, Guerrero, J. W. G., Suksatan, W., … & Khan, A. (2022). Numerical Investigation of Nanofluid Mixed Convection in a T-shaped Cavity by Considering a Thermal Barrier. *Alexandria Eng. J., 61* (9), 7393–7415. doi: 10.1016/j.aej.2022.01.009.

60. Ko, S. H., Lee, D., Hotz, N., Yeo, J., Hong, S., Nam, K. H., & Grigoropoulos, C. P. (2011). Digital Selective Growth of ZnO Nanowire Arrays from Inkjet-Printed Nanoparticle Seeds on a Flexible Substrate. *Langmuir, 28* (10), 4787–4792. doi:10.1021/la203781x.

61. Šimáková, P., Kočišová, E., & Procházka, M. (2021). “Coffee Ring” Effect of Ag Colloidal Nanoparticles Dried on Glass: Impact to Surface-Enhanced Raman Scattering (SERS). *J. Nanomater., 2021*, 4009352. doi: 10.1155/2021/4009352.
62. Sliz, R., Czajkowski, J., & Fabritius, T. (2020). Taming the Coffee Ring Effect – Enhanced Thermal Control as Method for Thin-Films Nanopatterning. *Langmuir, 36* (32), 9562–9570. doi:10.1021/acs.langmuir.0c01560.
63. Kwon, J., Hong, S., Lee, H., Yeo, J., Lee, S. S., & Ko, S. H. (2013). Direct Selective Growth of ZnO Nanowire Arrays from Inkjet-Printed Zinc Acetate Precursor on a Heated Substrate. *Nanoscale Res. Lett., 8* (1), 489. doi.: 10.1186/1556-276X-8-489.
64. Hong, S., Yeo, J., Manorotkul, W., Kang, H. W., Lee, J., Han, S., … & Ko, S. H. (2013). Digital Selective Growth of a ZnO Nanowire Array by Large Scale Laser Decomposition of Zinc Acetate. *Nanoscale, 5* (9)*,* 3698–3703. doi: 10.1039/c3nr34346d.
65. Guo, X. D., Pi, H. Y., Zhao, Q. Z., & Li, R. X. (2012). Controllable Growth of Flowerlike ZnO Nanostructures by Combining Laser Direct Writing and Hydrothermal Synthesis. *Mater. Lett., 66*, 377–381. doi: 10.1016/j.matlet.2011.09.008.
66. Hong, S., Yeo, J., Manorotkul, W., Kim, G., Kwon, J., An, K., & Ko, S. H. (2013). Low-Temperature Rapid Fabrication of ZnO Nanowire UV Sensor Array by Laser-Induced Local Hydrothermal Growth. J. *Nanomater., 2013*, 246328. doi:10.1155/2013/246328.
67. In, J. B., Kwon, H.-J., Lee, D., Ko, S. H., & Grigoropoulos, C. P. (2013). In Situ Monitoring of Laser-Assisted Hydrothermal Growth of ZnO Nanowires: Thermally Deactivating Growth Kinetics. *Small, 10* (4), 741–749. doi:10.1002/smll.201301599.
68. Liu, W. L., Chang, Y. C., Hsieh, S. H., & Chen,W. J. (2013). Effects of Anions in Electrodeposition Baths on Morphologies of Zinc Oxide Thin Films. *Int. J. Electrochem. Sci., 8* (1), 983–990. http://www.electrochemsci.org/papers/vol8/80100983.pdf
69. Jiangfeng, G., Zhaoming, D., Qingping, D., Yuan,X., & Weihua, Z. (2010). Controlled Synthesis of ZnO Nanostructures by Electrodeposition Method. *J. Nanomater., 2010*, 740628. doi: 10.1155/2010/740628.
70. Lin, Y., Yang, J., & Zhou, X. (2011). Controlled Synthesis of Oriented ZnO Nanorod Arrays by Seed-Layer-Free Electrochemical Deposition. *Appl. Surface Sci., 258* (4), 1491–1494. doi: 10.1016/j.apsusc.2011.09.113.
71. Sun, S., Jiao, S., Zhang, K., Wang, D., Gao, S., Li, H., … & Zhao, L. (2012). Nucleation Effect and Growth Mechanism of ZnO Nanostructures Electrodeposition from Aqueous Zinc Nitrate Baths. *J. Crystal Growth, 359*, 15–19. doi: 10.1016/j.jcrysgro.2012.08.016.
72. Xu, L., Guo, Y., Liao, Q., Zhang, J., & Xu, D. (2005). Morphological Control of ZnO Nanostructures by Electrodeposition. *J. Phys. Chem. B, 109* (28), 13519–13522. doi: 10.1021/jp051007b.
73. Skompska, M., & Zarębska, K. (2014). Electrodeposition of ZnO Nanorod Arrays on Transparent Conducting Substrates – A Review. *Electrochim. Acta, 127,* 467–488. doi: 10.1016/j.electacta.2014.02.049.

sciendo

LATVIAN JOURNAL OF PHYSICS
AND TECHNICAL SCIENCES
2023, N 6

DOI: 10.2478/lpts-2023-0036

USING PARTIAL SOLAR ECLIPSE FOR THE 14-METRE RADIO TELESCOPE CALIBRATION

J. Kallunki[1,2]

[1] Aalto University, Metsähovi Radio Observatory, Finland
[2] Metropolia University of Applied Science, Finland
E-mail: juha.kallunki@metropolia.fi

A partial solar eclipse occurred on 25 October 2022, in the central and northern parts of Europe. The partial solar eclipse was observed at Aalto University Metsähovi Radio Observatory, Finland at the radio wavelength of 8 mm (37 GHz). In Finland, the magnitude of the partial solar eclipse was 62.7 %. Solar radio maps at the time cadence of about 9 minutes were observed over the whole eclipse. The solar eclipse observations could be used for instrument calibration purposes. This paper investigates the solar brightness temperature, the limb brightening effect, the height of the chromosphere and the location of radio brightening using the aforementioned partial solar eclipse observations.

We got the confirmation that our earlier results are consistent, e.g., the solar brightness temperature matches with 8100 K ± 300 K. It was also possible to detect limb brightening effect. However, the prevailing solar activity might have distorted the final conclusions. The Moon should operate as a focusing element and the location of radio brightenings could be defined more carefully than in the normal conditions. We investigated this feature. Our results are in some parts unexpected and need further investigations.

Keywords: *Instrument calibration, partial solar eclipse, radio telescope, solar activity, solar radio observations.*

1. INTRODUCTION

Partial solar eclipses happen when the Moon comes between the Sun and Earth, but the Moon only partially covers the solar disk. In general, total solar eclipses and the sudden darkening of the sky are perhaps the most dramatic things any human can see. Partial eclipses are not so unique events than the total solar eclipse. Solar eclipses are also useful for the instrument calibration purposes. For instance, getting the Moon and the Sun in the same image helps in determining and calibrating the accuracy of the equipment. During a solar eclipse, we can also assess the size and shape of the

areas visible on the surface of the Sun with radio frequencies more accurately than is normally the case, as the edge of the Moon acts as a kind of timing mechanism. In addition, various Sun's coronal features could be studied during the eclipses.

The second partial solar eclipse of the year 2022 was on 25 October. It was visible from most of Europe, northern Africa, the Middle East, and the western parts of Asia. In Finland, the magnitude of the partial solar eclipse was 62.7 %, which is a relatively large coverage that is rarely observed. The greatest partial eclipse was in the northern Russia with a magnitude of 86.1 %.

The solar partial eclipse enables us to study some calibration issues: the definition of the quiet Sun level (QSL) brightness temperature, the limb brightening, the height of the solar chromosphere and a telescope's beam shape, for instance. In this study, we will investigate these issues using 14-metre radio telescope by Aalto University Metsähovi Radio Observatory, Finland. For instance, the quiet Sun level (QSL) brightness temperature can be defined more accurately since we can use a single background (cold sky) value as a base value. Normally, separate solar and lunar maps have to be made, which means that we have to assume that the base value is the same in both cases. This is not the most optimal way since the prevailing weather conditions may affect the results.

The solar limb has as a sharp edge in millimetre wavelengths, which is based on earlier eclipse observations. It has been reported that the depth of the chromosphere is about 8000 km at 3 mm [1]. The temperature range of the chromosphere is reported being between 6000 and 20 000 K [2] and, in recently, it has been measured to be 8100 K ± 300 K at 8 mm [3].

At the radio frequencies, total and partial eclipses have been studied by [4]–[6]. However, solar radio observations have been done with smaller telescopes, which could only record solar total intensity. The radio images from the Sun during the solar eclipse have rarely been made, only Nobeyama Radioheliograph in Japan has made some eclipse observations in the past, e.g., https://solar.nro.nao.ac.jp/120521Eclipse/index_e.html. However, any detailed analysis on the radio telescope properties during the eclipse has not been made.

A centre-to-limb brightening distribution in the millimetre wavelength has been studied earlier, *e.g.*, [2], [7]. The paper [7] reported smooth limb brightening in a scale of 0.5–2.0 % using radio solar maps from Aalto University Metsähovi Radio Observatory. There have been also discussions that limb brightening phenomena is mostly artificial effect caused by the observing instrument. The observations of limb brightenings have given varying and even contradictory results.

In Section 2, we will present our instrumentation and observations. The results are presented in Section 3. Finally, the conclusions are made in Section 4, including further investigation topics.

2. OBSERVATIONS

The RT–14 at Aalto University Metsähovi Radio Observatory (MRO), Finland (Helsinki region; E 24:23.35, N 60:13.04) is a Cassegrain type antenna with a diameter of 13.7 m. The usable wavelength range of the telescope is 13.0 cm–2.0 mm. In this work, we only used wavelength at 8 mm. During solar observations, the antenna can be used for solar mapping, partial solar mapping, and tracking of any

selected areas on the solar disk. We used only solar raster maps in this work. In Fig. 1, a millimetre raster scan map is shown as an example. The beam size of the telescope is 2.4 arc min at 8 mm.

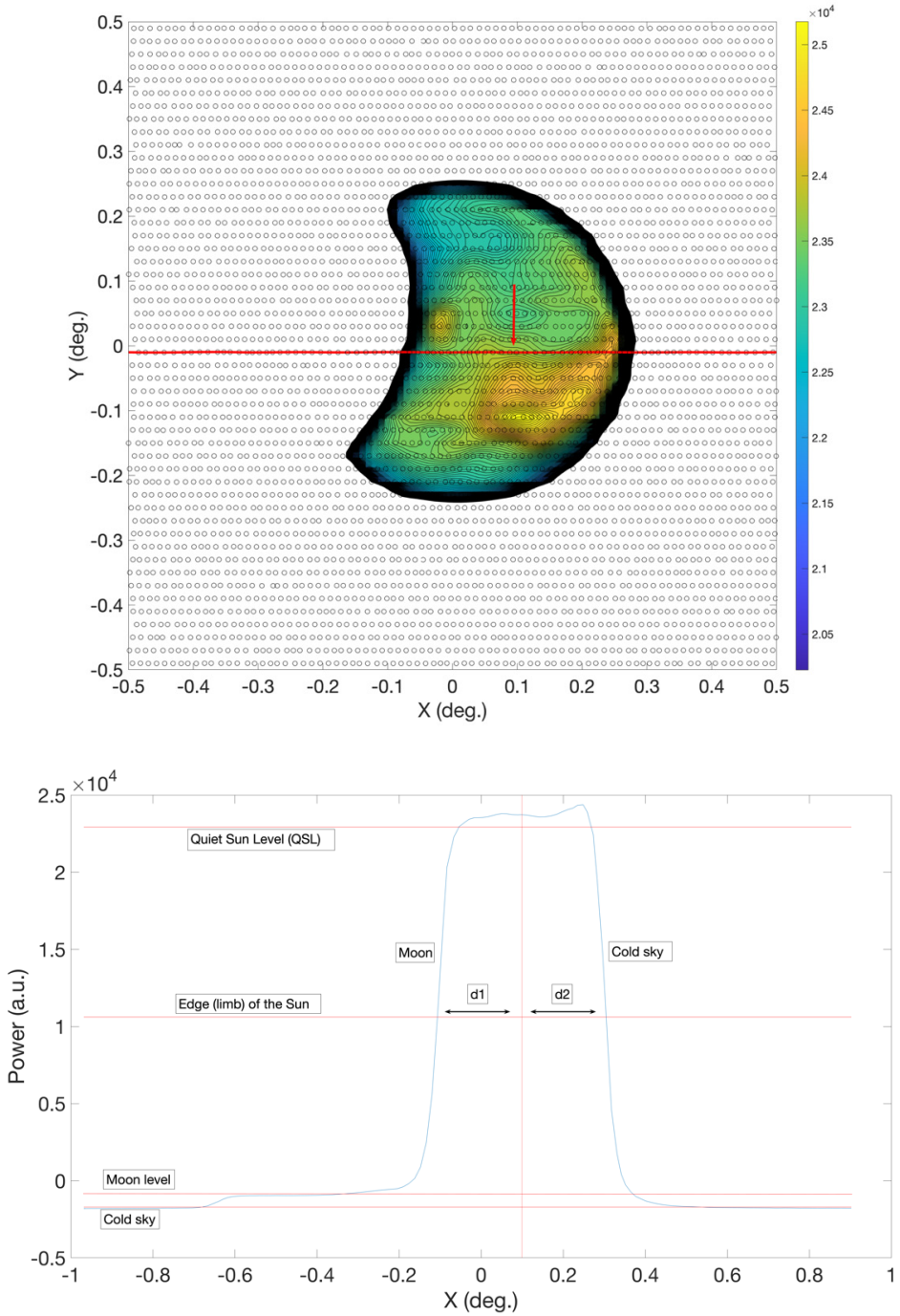

Fig. 1. On the upper panel, solar radio map at 8 mm during the partial solar eclipse. Black dots indicate single individual observation points. On the lower panel, a single sweep over solar disk is shown. The location of this sweep is shown in the upper panel, marked as a red line.

The receiver is Dicke-type radiometers. The noise temperature of the 8 mm receiver is approximately 280 K. It takes approximately 125 seconds to make one solar radio map, or even faster in 65 seconds with a slight low quality. In addition, the dynamic range of the system is wide enough that both solar and lunar observations could be made. In this study, we had to use a wider observing window that both the Sun and Moon could be observed simultaneously. Thus, a single solar (and lunar) took approximately nine minutes to make one solar radio map. The observational data are recorded in intensities. Because the measurements are always scaled relative to the QSL, the observations are comparable over the years. The brightness temperature of the QSL at 8 mm is 8100 K ± 300 K. The solar emission at 8 mm comes from the chromosphere [3], [8]. Taking into account the brightness temperature (8100 K ± 300 K), the emission comes from the low chromosphere.

Figure 1 (upper panel) shows the solar radio map during the later part of the partial eclipse. In the lower panel in Fig. 1, the single sweep is shown over the solar disk. The position of this sweep is marked as a red line in the upper panel. The black dots indicate single measurement points. Totally, 48 solar radio maps were observed on 25 October 2022 even if it was a late part of the year and the Sun culminated in rather low (< 20 deg.) elevation.

2. RESULTS

2.1. Defining the Brightness Temperature of the Sun at 8 mm

The brightness temperature of the Sun could be defined using the Moon brightness temperature, since the Moon brightness temperature could be estimated accurately. The eclipse observation is a unique opportunity to define the solar brightness temperature because the Sun and Moon could be observed simultaneously. For the calibration, the cold sky temperature is needed. In the eclipse observations, a common cold sky value could be used both solar and lunar value calibrations. Usually, the calibration will be done during the new moon, which means that we have to use two different values for the cold sky, and we have to assume that these values are the same. The solar brightness temperature could be defined as follows:

$$T_{Sun,qsl} = \frac{P_{Sun.qsl} - P_{sky}}{P_{moon,qsl} - P_{sky}} \times T_{moon,qsl},$$

where $P_{Sun,qsl}$ is marked with a text *Quiet Sun Level (QSL), $P_{moon,qsl}$* with a text *Moon level* and P_{sky} with a text *Cold sky* in Fig. 1 (lower panel). The more accurate definition of $P_{Sun,qsl}$ and P_{sky} can be found in [3].

By using values, shown in Fig. 1, the Sun-Moon power ratio is 32.55 and the mean brightness temperature of the Moon at 8 mm is 246.2 K during the New Moon [3]. Thus, the mean brightness temperature of the Sun is 8015 K at 8 mm. This value

confirms our previous results: 8100 ± 300 K [3]. However, it has been noticed that the prevailing weather conditions were rather unstable, and, in addition, some activity (active regions) was in the Sun during the partial eclipse. Those make a significant contribution to the results. It is really challenging to deduce what the total impact of the solar activity on the final results is.

2.2. Limb Brightening

On 25 October 2022, there was a strong solar activity. 4–5 solar active regions were in the Sun (see Fig. 2). The map, shown in Fig. 2 is observed with Solar Dynamic Observatory (SDO) satellite's Atmospheric Imaging Assembly (AIA) instrument EUV (Extreme Ultraviolet) 171 Å wavelength. Especially, active regions (AR13125, AR13126 and AR13131), which were located in the close to the solar limb, make a contribution to the calibration results. Ideally, the limb brightening investigation should be made in the period of low solar activity. Figure 3 presents two different limb sweep observations. In the upper panel, sweeps are recorded during the eclipse. The part of the Sun is partly covered by the Moon. In the lower panel, sweeps over the solar disk after the partial eclipse are shown. Each sweep is done close to the equator and as we can see in Fig. 2 there is an activity also close to the equator. In Figure 3, we can notice limb brightening effect, especially in the eastern part of a solar disk. The scale of the limb brightening is about 0.5–3 %, which matches with the results in [7]. It should be noted that we could not detect limb brightening phenomena in the western part of the solar disk. This could be referring to the instrumental effect or it could mean that solar activity was a major contributor to the limb brightening. However, final conclusions should not be made based solely on our observations.

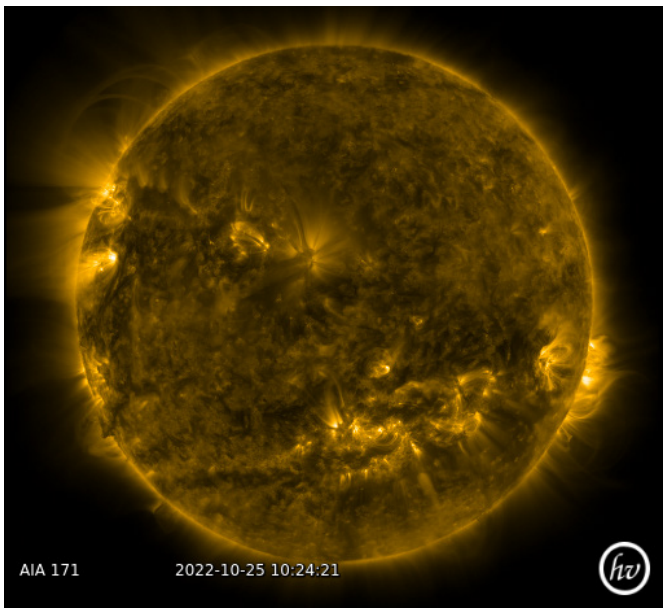

Fig. 2. SDO AIA 171 Å EUV map taken during solar eclipse. In the near of western limb, active region (AR) is existing. Two different active regions AR13125 and AR1312 are visible in the near of eastern limb. Unclassified, based on the Space Weather Prediction Centre (SWPC) by National Oceanic and Atmospheric Administration, (NOAA) active region is close to the middle of solar disk.

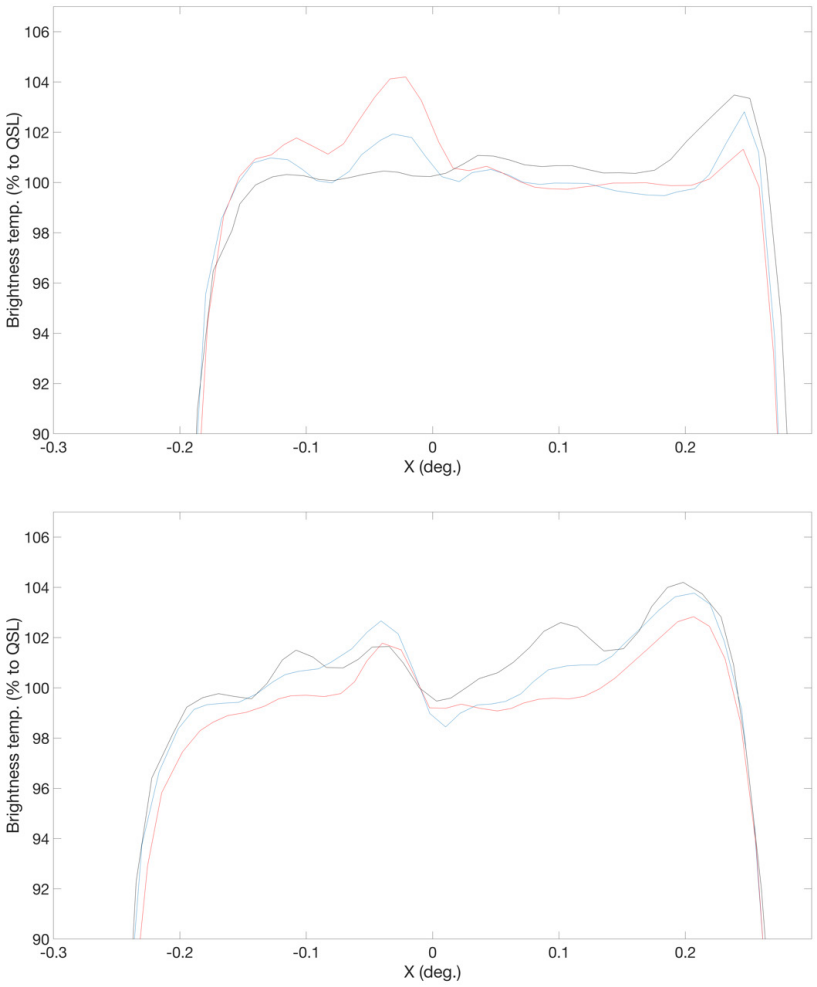

Fig. 3. On the upper panel, three different sweeps over the solar disk during the partial eclipse. The Moon has cut the left edge. Each sweep has to be made close to equator. On the lower panel, similar sweeps are shown, but after the partial solar eclipse and so the Moon does not affect these observations.

2.3. The Height of the Chromosphere

The chromosphere is a rather narrow solar atmospheric layer with a distance of 8000 km. In addition, the beam size of our radio telescope (MRO–14) is 2.4 arcmin (144 arcsec). It is large compared to the chromosphere depth or even solar disk size. The study [9] has shown that the solar radius varies between 979'' and 999'' at 8 mm using MRO–14 radio telescope over the solar cycle. On the lower panel in Fig. 1 a sweep is shown over the solar disk during the eclipse. The vertical red line indicates a centre point of the Sun during the eclipse (marked with an arrow on the upper panel in Fig. 1).

The horizontal red line in the middle of the right panel indicates the edge of the solar limb. We can notice that distances to both limb edges are equal (*d1=d2*, in lower panel of Fig. 1) and no differences can be noticed. This indicates that the depth of the chromosphere is narrow, but it equally means that the beam size of the radio telescope is too large to make any more detailed conclusions.

2.4. Location of the Active Region (Radio Brightening)

Finally, we investigated the location of the radio brightening during the eclipse. The left panel in Fig. 1 shows an unclassified active region near the western solar edge. The Moon has not cut it off and it is barely visible. In Fig. 4, overlapped solar radio maps are shown. On the left panel, we can notice that the location of the radio brightening maximum is not the same during the eclipse (red contour) and before the eclipse (black contour). The distance between these maxima is 0.006 deg. (x-direction) and 0.0148 deg. (y-direction). The raster scan map has been made so that the edge of the Moon cuts part of the active region. On the right panel, overlapped maps before and after the partial solar eclipse are shown. There the location of the radio brightening maximum is the same. This means that the Moon edge has some effect on the location of radio brightenings.

We used SDO's Helioseismic and Magnetic Imager (HMI) magnetogram as a reference source. The magnetogram maps show the solar magnetic field strength in the photosphere. The location of the magnetic field in the photosphere matches with the locations of the radio brightening [10], [11]. In Fig. 5, the magnetogram map is shown. The red arrow indicates the location of the magnetic field maximum. This position matches with the location of the radio brightening before and after the partial solar eclipse (Fig. 5, right panel). This result means that the Moon is not acting as a sharpening factor as it was expected. The result might be causing very unstable atmospheric conditions, which were during the partial solar eclipse. Also, a relatively large beam size of MRO–14 radio telescope (2.4 arcmin) probably causes some issues. Also, it might require a denser sweep interval. In current observations, it was roughly a beam width (40 mdeg.) divided by two. This result could also indicate that the location of the magnetic field in the photosphere did not match accurately with the locations of the radio brightening as it was reported earlier.

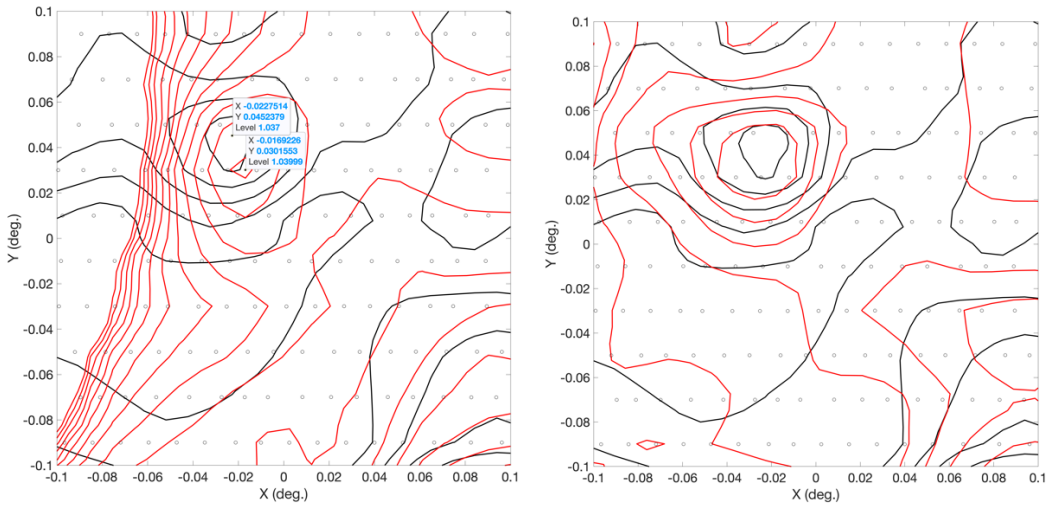

Fig. 4. On the left panel, two overlapped solar radio maps, one is made before the partial eclipse (black) and the second one during the eclipse (red). On the right panel, two overlapped solar radio maps, one is made before the partial eclipse and the second one after the eclipse.

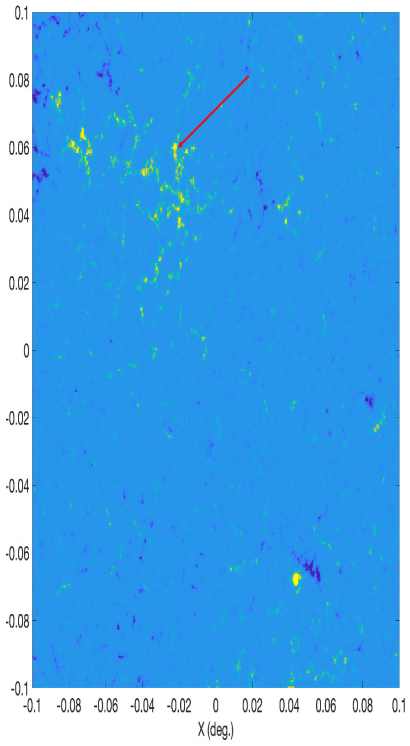

Fig. 5. SDO's Helioseismic and Magnetic Imager (HMI) magnetogram map on 25 October 2022, during the partial solar eclipse. The red arrow indicates the location of the magnetic field strength maximum.

3. CONCLUSIONS

Unfortunately, the prevailing weather conditions were rather poor with thick clouds and rain showers during the partial eclipse day. This meant that we could not observe faster solar radio maps. Wuth this method, we could have achieved less than a seven minute time resolution. In addition, the date of the partial eclipse was not the most favourable since the Sun culminated already in 20 degrees and longer solar observation run was not possible.

We showed that the partial solar eclipse enabled various radio telescope calibration observations. In addition, some scientific conclusions could be made. We also got the confirmation of our previous results, e.g., solar brightness temperature. The next partial solar eclipse in Finland will be in 2025. The period is close to the maximum of Solar Cycle 25. This has to be taken into account in the planning process. Hopefully, we could repeat our observations during the next partial solar eclipse with better prevailing weather conditions. Our results emphasize the significance of the prevailing weather conditions when doing ground-based observations for calibration purposes. This is also true in solar observations. In addition, we noticed that radio telescope beam size should be small enough that all calibration studies could be made properly. Moreover, we have to investigate whether is it possible to realize some of these calibration measurements also in some other form,

so that the solar eclipse observations are not always mandatory. We did not evaluate telescope side lobe (e.g., [2]) properties during this partial solar eclipse. This could be an interesting topic for further research.

ACKNOWLEDGEMENTS

The research has partly been conducted in a memory of Professor Jay Pasachoff who passed away soon after the partial eclipse. Courtesy of NASA/SDO and the AIA, EVE, and HMI science teams.

REFERENCES

1. White, S. M., & Kundu, M. R. (1994). Observations of the 1991 Eclipse at 3.5 MM Wavelength. *Infrared Solar Physics, 154,* 167.
2. Iwai, K. (2017). The Brightness Temperature of the Quiet Solar Chromosphere at 2.6 mm. *Solar Physics, 292* (1). doi:10.1007/s11207-016-1044-5.
3. Kallunki, J., & Tornikoski, M. (2018). Measurements of the Quiet-Sun Level Brightness Temperature at 8 mm. *Solar Physics, 293* (11). doi:10.1007/s11207-018-1380-8.
4. Leung, C. S., Fok, T. K. T., Hui, K. H. K., Ng, K. W., Lee, C. M., & Chang, S. H. (2022). Solar Eclipse Observations with Small Radio Telescope in Hong Kong in the 21 CM Radio Frequency Band. *Romanian Astronomical Journal, 32* (1), 35–52.
5. Shramko, A. D., & Guseva, S. A. (2018). Chromospheric and Coronal Radio Sources from Observations of the Partial Solar Eclipse of March 20, 2015, at the Mountain Astronomical Station of the Central Astronomical Observatory. *Geomagnetism and Aeronomy, 58* (4), 464–468. doi:10.1134/S0016793218040163.
6. Gireesh, G. V. S., Kathiravan, C., Barve, I. V., & Ramesh, R. (2021). Radio Interferometric Observations of the Sun Using Commercial Dish TV Antennas. *Solar Physics, 296* (8). doi:10.1007/s11207-021-01871-9.
7. Pohjolainen, S. (2000). On the Origin of Polar Radio Brightenings at Short Millimeter Wavelengths. *Astronomy and Astrophysics, 361*, 349–358.
8. Kallunki, J. (2018). Forty years of solar radio observations at Metsähovi Radio Observatory. *Astronomische Nachrichten, 339* (204), 204–211. doi:10.1002/asna.201813464.
9. Selhorst, C. L., Kallunki, J., Giménez de Castro, C. G., Valio, A., & Costa, J. E. R. (2019). The Solar Radius at 37 GHz through Cycles 22 to 24. *Solar Physics, 294* (12). doi:10.1007/s11207-019-1568-6.
10. Kallunki, K., Tornikoski, M., & Bezrukovs, D. (2021). Radio observations of solar active regions at 7.36 and 37 GHz. *Astronomical and Astrophysical Transactions, 32* (3), 241–248.
11. Smirnova, V. V., Solov'ev, A. A., Riehokainen, A., & Kallunki, J. (2015). Modulation of Radio Source Radiation at a Frequency of 37 GHz by Long-Period Oscillations of a Nearby Sunspot. *Geomagnetism and Astronomy, 55* (7), 991–994. doi:10.1134/S001679321507021X.

sciendo

LATVIAN JOURNAL OF PHYSICS
AND TECHNICAL SCIENCES
2023, N 6

DOI: 10.2478/lpts-2023-0037

NON-ENZYMATIC Co_3O_4 NANOSTRUCTURE-BASED ELECTROCHEMICAL SENSOR FOR H_2O_2 DETECTION

V. Mizers[1*], V. Gerbreders[1], M. Krasovska[1], E. Sledevskis[1],
I. Mihailova[1], A. Ogurcovs[1,2], A. Bulanovs[1], A. Gerbreders[2]

[1] G. Liberts' Innovative Microscopy Centre, Department of Technology,
Institute of Life Sciences and Technology, Daugavpils University,
1a Parades Str., Daugavpils, LV-5401, LATVIA
[2] Institute of Solid State Physics, University of Latvia,
8 Kengaraga Str., Riga, LV-1063, LATVIA
*e-mail: valdis.mizers@du.lv

This article describes the synthesis of nanostructured cobalt oxide on iron wires and its application for the detection of hydrogen peroxide as working electrode for non-enzymatic electrochemical sensor. Cobalt oxide was obtained by the hydrothermal synthesis method using chloride and acetate anions. The resulting nanostructured coating obtained from the chloride precursor is a uniform homogeneous porous network of long nanofibers assembled into regular honeycomb-like formations. In the case of an acetate precursor, instead of nanofibers, petal-like nanostructures assembled into honeycomb agglomerates are observed. The structure, surface, and composition of the obtained samples were studied using field-emission scanning electron microscopy along with energy-dispersive spectroscopy and X-ray diffractometry.

The resultant nanostructured specimens were utilized to detect H_2O_2 electrochemically through cyclic voltammetry, differential pulse voltammetry, and i-t measurements. A comparative research has demonstrated that the nanostructures produced from the chloride precursor exhibit greater sensitivity to H_2O_2 and have a more appropriate morphology for designing a nanostructured sensor. A substantial linear correlation between the peak current and H_2O_2 concentration within the 20 to 1300 μM range was established. The Co_3O_4 electrode obtained exhibits a sensitivity of 505.11 $\mu A \cdot mM^{-1}$, and the electroactive surface area is calculated to be 4.684 cm^2. Assuming a signal-to-noise ratio of 3, the calculated limit of detection is 1.05 μM. According to the interference study, the prevalent interfering agents, such as ascorbic acid, uric acid, NaCl, and glucose, do not influence the electrochemical reaction. The obtained results confirm that this sensor is suitable for working with complex analytes.The actual sample assessment demonstrated a recovery rate exceeding 95 %.

Keywords: *Electrochemical sensor, cobalt oxide, cyclic voltammetry, hydrogen peroxide, nanostructures.*

1. INTRODUCTION

Hydrogen peroxide is a strong oxidant and has found wide application in chemical industry, paper production, medicine and food industry. [1] Since hydrogen peroxide is considered relatively safe for humans [2]–[5] it has found wide application as a bleaching and disinfecting agent in various household chemicals, cosmetics and medical products. In a number of countries, hydrogen peroxide is used for water treatment [6]–[8] and preservation of food products (for example, milk) [9], [10].

In living organisms, hydrogen peroxide is formed as a result of incomplete reduction of oxygen during metabolism and is one of the most important reactive oxygen species, which are a by-product of many physiological and pathophysiological processes, such as metabolism, iron proliferation and homeostasis, antioxidant and anti-inflammatory response, response to DNA damage and many others. That is why various reactive oxygen species (and H_2O_2, in particular) are always present in living organisms in small concentrations [11].

However, when the antioxidant defense of the body fails and the concentration of reactive oxygen species exceeds natural values, an oxidative stress occurs. Oxidative stress leads to a damage of nucleic acids, proteins and lipids, which is the cause of various pathological conditions, such as accelerated aging of the body, neurodegeneration, and can also provoke the development of serious diseases such as atherosclerosis and diabetes [12]–[16].

An increase in the concentration of hydrogen peroxide can also be associated with cancer: it has been proven that malignant tumor cells contain up to 100 μM H_2O_2, while the concentration of H_2O_2 in normal cells usually does not exceed 20 nM [17]–[20]. For some types of cancer, such as lung cancer, an increase in the concentration of H_2O_2 in the exhalation is characteristic [18], as well as an increase in the concentration in the blood [21]–[23]. That is why the determination of the concentration of hydrogen peroxide in the blood and other biological fluids can serve as an additional method for diagnosing these diseases [24]–[26].

In various publications, the concentration of H_2O_2 in the blood plasma of a healthy person is indicated in a very wide range from 1 μM to 40 μM. The indicated maximum, although not fatal, is quite stressful and destructive for the cells. Probably, overestimated concentration values were obtained as a result of the peculiarities of the measurement protocol and under the influence of interfering substances that contribute to the obtained value. Since the level of hydrogen peroxide in living organisms is maintained by regulatory mechanisms, and in particular by peroxidase and catalase, the most probable concentration of peroxide in the blood of a healthy individual is in the range of 1–5 μM. However, the possibility of an increase in the concentration of hydrogen peroxide due to the presence of the aforementioned diseases should not be ruled out. Therefore, during the experiment it is very important to carefully study the influence of other substances on the accuracy of the measurement in order to exclude the possibility of the

influence of interferents and to distinguish a false increase in concentration due to the influence of foreign substances from an increase caused by a disease. In addition to medicine, rapid and accurate determination and control of the H_2O_2 concentration is an important task in many other areas, including pharmaceuticals [27], [28], food production [29]–[32], and environmental protection [33].

A number of conventional methods used for concentration measurements for various chemicals (such as titration [34], [35], chemiluminescence [36], [37], and spectrophotometry [38]–[40]) are not suitable for H_2O_2 determination. These methods have a list of disadvantages such as the need for complex equipment (as a result, the need to transport the sample to the laboratory), low sensitivity, significant measurement time, and the need for manual sample preparation. These factors can significantly affect the measurement accuracy due to degradation of samples and changes in the concentration of hydrogen peroxide due to its natural decomposition in the process of sample storage and preparation.

Therefore, at present, the method of electrochemical detection has become widespread [41]–[44]. This method is simple, fast, and accurate. The selectivity of this method allows to avoid a false increase in concentration and eliminating the influence of interfering substances [45], [46]. Based on this method, it has already become possible to create portable devices that allow measurements to be taken directly at the place of sampling without transportation. This can be relevant both in the field of medicine and in the field of environmental monitoring, in particular for monitoring the quality of wastewater.

Electrochemical measurements use working electrodes that can either be modified or unmodified. Modified electrodes are functionalized with redox-active enzymes to ensure accurate and selective measurements, such as the widely used horseradish peroxidase for detecting hydrogen peroxide [47]–[50]. However, using enzymes comes with significant drawbacks, such as increased production costs and reduced electrode stability due to their vulnerability to thermal and chemical damage. To overcome these drawbacks, non-enzymatic electrochemical sensors are becoming more popular, where H_2O_2 interacts directly with the electrode material, resulting in catalytic processes that produce an unambiguous electrochemical response [51]–[54].

Carbon materials [20], as well as thin films of metals [55], [56], and metal oxides [57], [58] are widely used as sensor materials. Utilizing these substances in the nanopowder and nanostructure configuration enables a substantial enhancement in sensor sensitivity by multiplying the active surface area of the functioning electrode[59].

Among the nanostructured materials used, cobalt oxide (Co_3O_4) is a promising candidate [60], [61].

Cobalt oxide is widely employed in supercapacitors and sensors for various applications, including glucose and hydrogen peroxide sensors. It exhibits diverse morphologies such as nanocubes, nanoplates, and nanowhiskers, which can be controlled by altering the precursor ions during hydrothermal synthesis (commonly chloride, nitrate, acetate, and cobalt sulfate) and incorporating structure-directing agents like ammonia, ethanol, and alkali solutions.

A commonly used method to apply

Co_3O_4 nanostructures onto electrodes involves obtaining them as a powder [62], followed by dipping or drop coating techniques with a porous substrate [63] or binder polymers [64]. However, this approach has drawbacks, such as uneven suspension distribution leading to variations in electrochemical properties, repeatability issues, poor adhesion, and low mechanical stability of the coating. These challenges can be overcome by utilizing a hydrothermal growth process, enabling the epitaxial growth of well-ordered nanostructured layers directly onto the wire electrode substrate, facilitated by specific anions or additives.

This technique results in the formation of nanostructures with a significant active surface area, facilitating an efficient electron charge transfer between Co_3O_4 nanostructures and the substrate due to high-density honeycomb-like nanostructured aggregates.

This article focuses on the preparation of nanostructured Co_3O_4 electrodes using the hydrothermal method and demonstrates the exceptional selectivity and sensitivity of the resulting wire electrodes in electrochemically detecting H_2O_2. The study also investigates the influence of precursor anions on the nanostructure's morphology and, consequently, the sensor's sensitivity. Essential electrochemical measurements have been performed to determine H_2O_2 concentrations in aqueous solutions using the developed sensor, and experiments have been conducted to detect H_2O_2 in real samples of UHT milk and contact lens storage liquid.

2. MATERIALS AND METHODS

2.1 Materials

Merck was the source of Cobalt(II) chloride hexahydrate (CAS number: 7791-13-1), cobalt(II) acetate tetrahydrate (CAS number: 6147-53-1), hexamethylenetetramine CH_4N_2O (CAS number: 100-97-0), sodium hydroxide (NaOH, CAS number: 1310-73-2), and 30% hydrogen peroxide solution (H_2O_2, CAS number: 7722-84-1). The reagents were of at least 99.8% purity. Ascorbic acid ($C6H_8O_6$, CAS number: 50-81-7), uric acid ($C_5H_4N_4O_3$, CAS number: 69-93-2), glucose ($C_6H_{12}O_6$, CAS number: 50-99-7), and sodium chloride (NaCl, CAS number: 7647-14-5) were procured from Sigma Aldrich and were also of at least 99.8% purity. The laboratory obtained distilled water. Iron wire (99.9% purity, 2 mm thickness) and Ag/AgCl wire were procured from Sigma Aldrich and A-M Systems, USA, respectively. Additionally, carbon rods (5 mm diameter) were purchased from Sigma Aldrich.

2.2 Co_3O_4 Layer Synthesis on Iron Wire

Iron wire was used as a base to obtain the nanostructured layer. Prior to the synthesis of the nanostructured coating, the wire was treated with fine sandpaper and immersed in 0.1 M HCl to increase the roughness of electrode surface and improve the adhesion of the nanostructures. An equimolar aqueous solution of 0.1 M $CoCl_2*6H_2O$ and CH_4N_2O was mixed in 80 mL distilled water to form

a red violet growth solution. The solution was stirred until the solid reagents dissolved completely and then moved with the pretreated iron wire together into a 100 mL glass beaker covered with a glass lid in the preheated oven. The growth took place at 5 h and 95 ºC, resulting in a dull pink $Co(OH)_2$ coating on the wire. Once cooled to room temperature, the substrate was rinsed with deionized water multiple times to eliminate any leftover reagents and subsequently dried at 80ºC overnight. The growth process was followed by thermal decomposition of $Co(OH)_2$ for 1 h at 450 ºC to obtain Co_3O_4. After annealing, a black, homogeneous Co_3O_4 coating was observed on the wire surface.

To investigate how the acetate anion affects the morphology of Co_3O_4 nanostructures, 0.1 M $(CH_3COO)_2Co*4H_2O$ was used. The rest of the synthesis process took place under the same parameters as in the case with the use of cobalt chloride.

The surface morphology of the nanostructured Co_3O_4 samples was examined using field-emission scanning electron microscopy (FESEM, Tescan MAIA 3), while energy-dispersive spectroscopy (EDS, Inca Synergy) was used to determine their chemical composition. The crystalline structure of the samples was determined using an X-ray diffractometer (RIGAKU Smart Lab, Cu Kα [λ = 1.543 Å]), which employed a parallel beam scanning geometry and an additional Ge(220) × 2 bounce monochromator.

3. ELECTROCHEMICAL MEASUREMENTS

To ensure an improved electrical contact with the equipment, wire samples coated with nanostructures were cut into 3 cm long pieces, and the end of one side was stripped to expose pure iron over a length of 1 cm. The measurements were conducted using an electrochemical station (Zanher, Germany), employing a three-electrode cell setup. The cobalt oxide-coated iron wire served as the working electrode, a 2 mm diameter Ag/AgCl wire acted as the reference electrode, and a 5 mm diameter carbon rod functioned as the counter electrode. Cyclic voltammetry (CV) was performed within the range of -1.3 V to 0.5 V vs Ag/AgCl, with an initial potential of 0 V and a scan rate of 100 $mV \cdot s^{-1}$. A buffer solution of 0.1 M NaOH was utilized. For the detection of H_2O_2, concentrations ranging from 0.2 mM to 5 mM were employed, including 0.2, 0.4, 0.6, 0.8, 1, 2, 3, 4, and 5 mM. Each concentration was tested five times, and the resulting graphs in subsequent sections represent the averaged data from all measurements. The relationship between the electrochemical current response and solution pH and scanning speed was analysed to achieve maximum sensitivity of the sensor. Impedance spectroscopy was performed across a frequency range of 1 Hz to 100 kHz, with an applied signal voltage of approximately 0.25 V. To investigate the current response, a fixed voltage of U = -1.23 V vs Ag/AgCl was applied to the cell, and the resulting current was measured. A buffer solution of 0.1 M NaOH was used for the experiment. Initially, the measurement was conducted in a buffer solution without hydrogen peroxide, allowing for a stabilization period of 120 s. Subsequently, 20 µM portions of H_2O_2 were added at intervals of 120 s. The concentration of H_2O_2 ranged

from 20 μM to 1300 μM, with increments of 20 μM in the range of 0–200 μM, 50 μM in the range of 250–700 μM, and 100 μM in the range of 800–1300 μM. The measurement was carried out with continuous stirring using a magnetic stirrer.

To examine the interference of commonly encountered substances, a constant voltage of U = -1.23 V vs Ag/AgCl was applied to the cell, and the resulting current was measured. A buffer solution of 0.1 M NaOH was used for the experiment. The measurement began with a pure buffer solution (0 μM H_2O_2), and every minute, H_2O_2 or an interferent was added to the solution at a concentration of 100 μM. The substances were added in the following order: H_2O_2, ascorbic acid, uric acid, glucose, and NaCl. This cycle was repeated three times, and the measurement was conducted with continuous stirring using a magnetic stirrer. To demonstrate the practical application potential of Co_3O_4 nanostructured electrodes in electrochemical sensor development, ultra-high temperature processed (UHT) milk and contact lens storage solution were investigated. These substances have complex compositions and were chosen to assess the impact of the sample matrix on the sensor's accuracy. Milk with 3.2% fat content was purchased from a local supermarket, and contact lens storage solution (Diviniti Ocean Moist multi-purpose contact lens care solution) was obtained from a local optical salon. To minimize the influence of the sample matrix, the milk and lens storage solution was diluted in a 1:2 ratio with a standard 0.1 M NaOH buffer solution. The amperometric response method was employed for the analysis, with U = -1.23 V vs Ag/AgCl.

4. RESULTS AND DISCUSSION

As a result of the hydrothermal synthesis, a homogeneous black coating with good adhesion to the surface has been obtained. High mechanical resistance allows for the pretreatment of samples necessary for the electrochemical measurements to be carried out and storage without loss of their quality.

SEM images of the Co_3O_4 nanostructures with nanoporous morphology obtained from the precursor of cobalt chloride and urea are shown in Fig. 1(a–b). The surface of the wire is covered with a homogeneous porous network of long nanofibers assembled into regular honeycomb-like formations.

The acetate anion has effectively changed the morphology of the Co_3O_4 nanostructures. A network of honeycomb formations is still observed on the surface; however, instead of nanostructured fibers, they consist of very thin petal-like structures. In addition, the honeycombs themselves are much smaller in size compared to the chloride anion-assisted ones.

The formation of the honeycomb-like nanoporous Co_3O_4 structures typically involves the following reactions: [65]:

$$CoCl_2 \rightarrow Co^{2+} + 2Cl^- \quad (1)$$

$$(H_2N)^{2-}CO + 2H_2O \rightarrow 2NH_3 + CO_2 \quad (2)$$

$$NH_3 + H_2O \rightarrow NH^{4+} + OH^- \quad (3)$$

$$Co^{2+} + 2OH^- \rightarrow Co(OH)_2 \quad (4)$$

$$3Co(OH)_2 \rightarrow Co_3O_4 + 2H_2O + H_2 \quad (5)$$

During annealing, the $Co(OH)_2$ compound undergoes a thermodynamically unstable state and transforms into the Co_3O_4 phase [66].

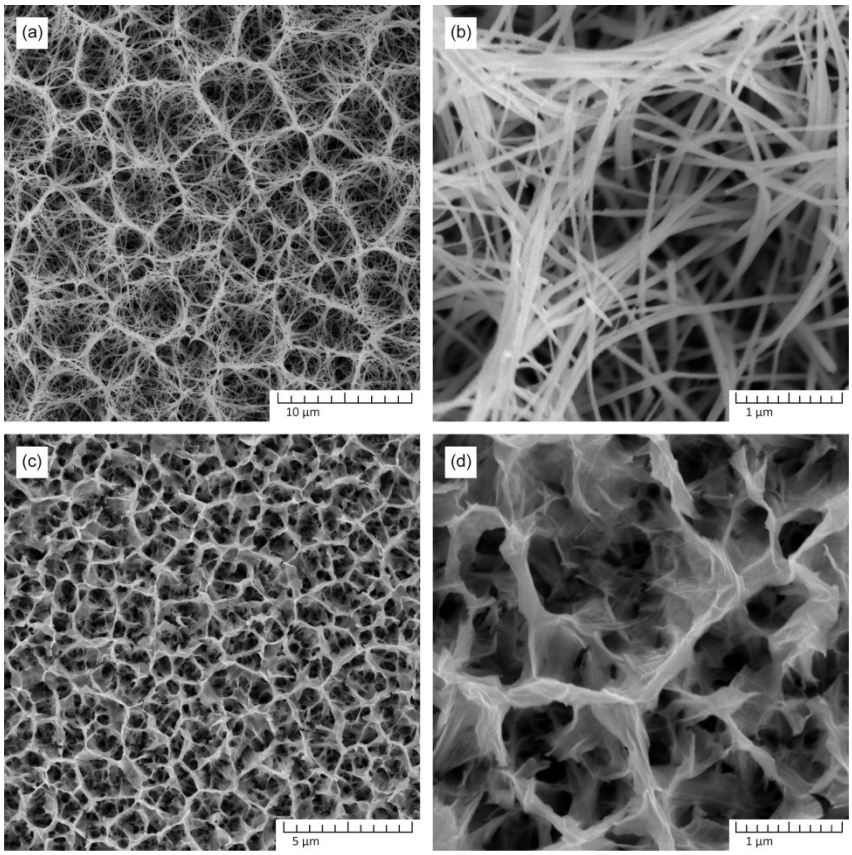

Fig. 1. The study of the anion effect on the morphology of the Co_3O_4 nanostructures. Co_3O_4 nanostructures obtained from the precursor of cobalt chloride and urea (a-b), Co_3O_4 nanostructures obtained from the precursor of cobalt acetate and urea (c–d).

According to [67], a proposed growth mechanism for Co_3O_4 nanowires involves the initial generation of Co nuclei, which gradually undergo a transformation into small nanoparticles. These nanoparticles then serve as nuclei for the growth of larger particles. This growth process is energetically favorable due to a decrease in surface energy as the nanoparticle size increases. To minimize surface energy, the small nanoparticles undergo an aggregation process, leading to the formation of larger nanoparticle aggregates.

The dynamic behavior of these aggregates enables them to move within the solution and come into contact with neighboring nanoparticles. As a result, they merge together, forming short chain structures that act as templates for the formation of elongated rod-like structures. During the later stages of growth, attaching new Co nuclei to existing nanoparticle agglomerates becomes more energetically favorable than creating individual nanoparticles. As a result, the chains formed during this stage further develop into complete nanofibers, exhibiting an increase in linear dimensions based on the growth anisotropy along various crystallographic planes.

Since the nanofibers are quite thin and long, they are not able to maintain a vertical position, so they tilt, meet

with neighboring structures, and continue growing in groups to form a cellular surface structure. The variation in the morphology of nanostructures achieved by using cobalt acetate as the precursor can be elucidated as follows. Acetate ions possess surfactant properties, functioning as capping agents during the growth of nanostructures. These ions contain charged regions that can selectively attach to specific crystallographic planes, impeding growth along those directions and stimulating growth in atypical directions.

In the case of cobalt acetate, the growth of nanofibers in length is hindered as acetate ions block this particular growth direction. Instead, the formation of 2D structures becomes prominent. Moreover, the extensive blocking of numerous crystallographic planes restricts the complete development and enlargement of the initial generation nanostructure. Consequently, recurrent renucleation and attachment occur, resulting in the formation of second-generation nanostructures. These nanostructures are often smaller in size and exhibit lower crystallinity.

As a result, a network of second-generation nanostructures is established, and the overall nanostructured coating possesses reduced crystallinity compared to the original process conducted without acetate ions. This observation is further supported by the X-ray diffraction pattern of the obtained samples (Fig. 2). Specifically, the nanostructures produced with the presence of acetate ions exhibit less prominent peak heights corresponding to crystallographic planes and demonstrate a higher amorphous background.

In addition, EDS microanalysis confirmed the high chemical purity of the obtained samples. The composition of the samples consists of cobalt (47.22 at. %) and oxygen (52.78 at. %) atoms, indicating the absence of any foreign impurities. This analysis further supports the quality and integrity of the Co_3O_4 nanostructures. Figure 2 displays the results of XRD analysis.

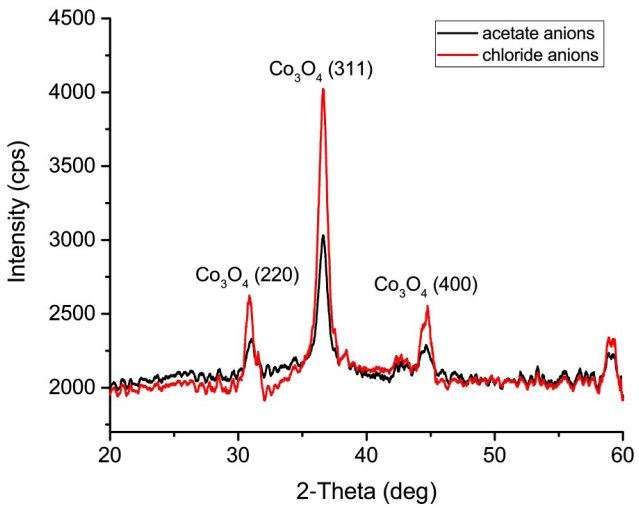

Fig. 2. X-ray diffraction pattern of CO_3O_4 nanostructured samples synthesized via the hydrothermal method. The red and black curves correspond to the chloride anion-assisted structures and the acetate anion-assisted samples, respectively.

The peaks shown in the graph correspond solely to Co_3O_4, indicating a high purity of both samples without any extraneous phase inclusions. While the presence of a background suggests the existence of an amorphous phase, the clear and distinct peaks demonstrate the crystalline nature of the obtained Co_3O_4 nanofibers. The X-ray diffraction pattern exhibits multiple crystallographic planes related to the Co_3O_4 lattice, with the dominant orientation perpendicular to the (3,1,1) planes. As illustrated in Fig. 2, the intensity of the peak for the (3,1,1) plane is higher for the chloride precursor sample than that for the acetate precursor sample, indicating a higher level of crystallinity in the former.

To assess the performance of the nanostructured electrode, cyclic voltammetry (CV) was employed at a scan rate of 100 $mV \cdot s^{-1}$ in a 0.1 M NaOH electrolyte for the detection of H_2O_2. Figure 3a presents the CV results obtained with and without the addition of H_2O_2 to a 0.1 M NaOH buffer solution, focusing on Co_3O_4 nanofibers derived from chloride anions. Notably, the Co_3O_4 modified electrode displayed two distinct pairs of clearly defined redox peaks [68].

In the presence of 0.1 M NaOH, the Co_3O_4 electrode exhibited anodic peaks at approximately -0.8 V (peak I) and -0.15 V (peak II), along with cathodic peaks at around -1.23 V (peak III) and 0.35 V (peak IV). These peaks corresponded to the oxidation and reduction processes of cobalt phases. The reversible transition between

Co_3O_4 and CoOOH was attributed to the redox peak pair I/III, while the further conversion between CoOOH and CoO_2 was ascribed to another redox peak pair II/IV [68]. These two reversible reactions can be described as follows [69]–[71]:

$$Co_3O_4 + OH^- + H_2O \rightarrow 3CoOOH + e^- \quad (6)$$

$$CoOOH + OH^- \rightarrow CoO_2 + H_2O + e^- \quad (7)$$

Upon the addition of 0.2 mM H_2O_2 into the buffer solution, the shape of the CV curve significantly changed with a significant increase in the peak current for the oxidation peak (I) and reduction peak (III).

The peak (III) current value increases linearly with an increase in the concentration of the added H_2O_2. Peak (I) increases less pronouncedly; moreover, with increasing concentration, its position along the x axis shifts, reaching -0.7 V for high concentrations. With the addition of H_2O_2, peak (II) shows no visible changes over the entire range of concentrations. Peak (IV) also changes slightly with the addition of various concentrations of H_2O_2.

The mechanism [68]–[70], [72]–[74] of the electrocatalysis of H_2O_2 is shown in Eq. (8):

$$6CoOOH + H_2O_2 \rightarrow 2Co_3O_4 + O_2 + 4H_2O \quad (8)$$

The CV results for the Co_3O_4 petal-shaped nanostructures obtained from the acetate precursor are shown in Fig. 3b. It can be seen that when peroxide is added, the height of peak (III) is significantly lower than for similar concentrations in the case when fiber-like samples are used (Fig. 3a). This indicates a lower sensitivity and, as a result, the effectiveness of this morphology for H_2O_2 detection. This may be due to the low crystallinity of this morphology and the blocking of active bonds by acetate ions. In addition, the resulting nanopetals are very thin and can stick together under the influence of the weight of the liquid, which significantly reduces the working surface area. Therefore, later in this article, fiber-like nanostructures are considered.

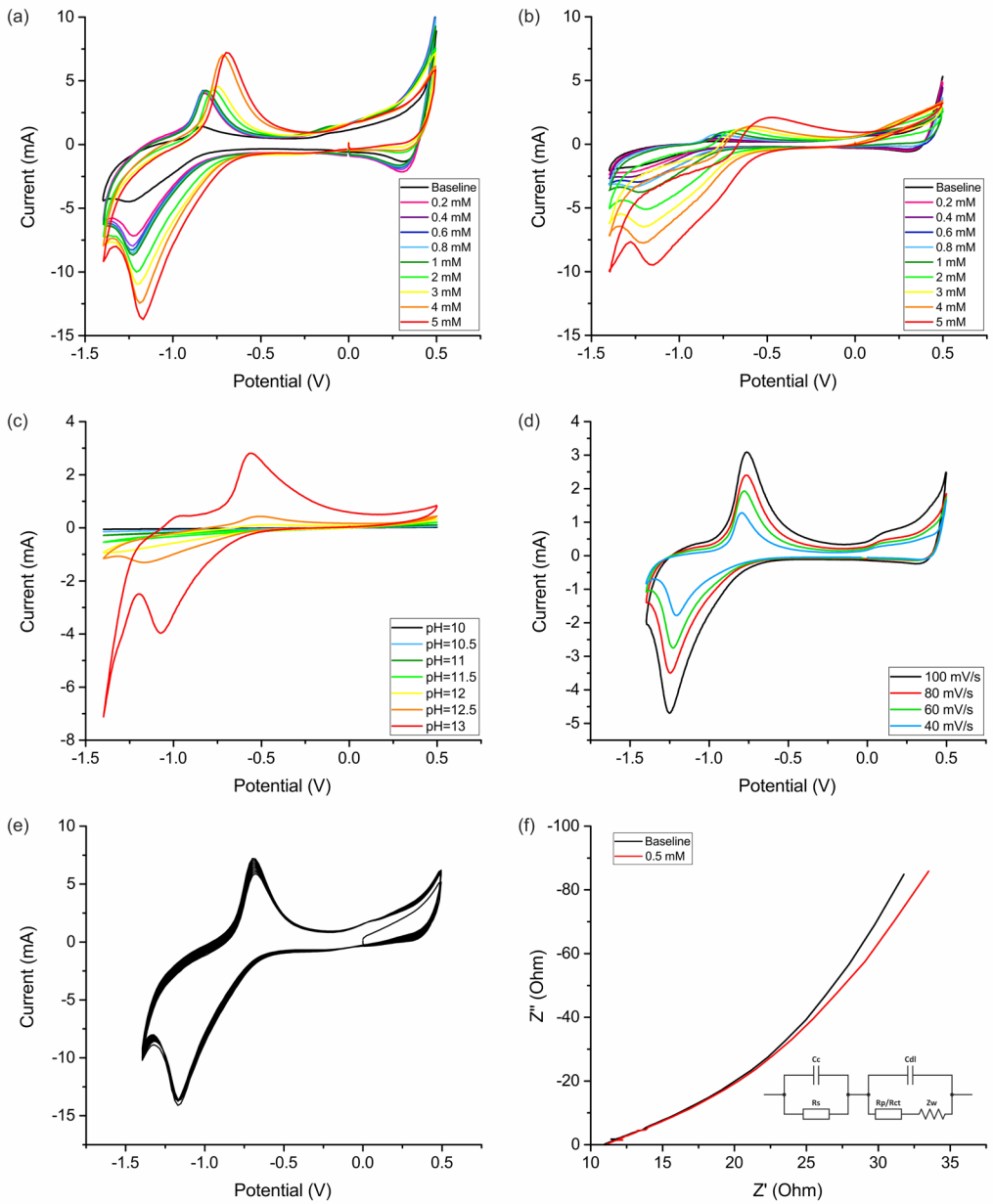

Fig. 3. (a) CV results of a nanostructured Co_3O_4 film derived from chloride anions. Measurements were performed at a scan speed of 100mV/s in a 0.1 M NaOH buffer solution (pH = 13) containing 0-5mM H_2O_2. (b) CV results of a nanostructured Co_3O_4 film derived from acetate anions at the same measurement conditions. (c) The results of CV measurements obtained at different pH values of the buffer solution. Measurements were conducted in NaOH solution containing 5 mM H_2O_2 at a scan rate of 100 mV/s. (d) The results of CV measurements obtained at different scan rates. Measurements were conducted in a 0.1 M NaOH solution containing 5 mM H_2O_2. (e) Working electrode stability study over multiple CV cycles (n = 50). Measurements were conducted in a 0.1 M NaOH solution containing 5 mM H_2O_2. (f) Electrode EIS analysis with a frequency range of 1 Hz to 100 kHz at an applied 0.25V signal voltage. Measurements were conducted in a 0.1 M NaOH solution before and after adding 0.5 mM H_2O_2.

The electrochemical response of Co_3O_4 nanofiber arrays towards 5 mM H_2O_2 was studied using CV at different scan rates ranging from 40 to 100 mV·s-1 (Fig. 3d). It was observed that the electrocatalytic reduction peak current towards H_2O_2 increased with the increase in scan rates. This indicates that the Co_3O_4 nanofiber electrode performs better for H_2O_2 detection at a scan rate of 100 $mV \cdot s^{-1}$.The CV responses of Co_3O_4 nanofiber arrays were examined at numerous concentrations of NaOH with the aim of determining the effect of pH levels of the buffer solution on the sensing effectiveness towards H_2O_2 (Fig. 3d). The absence of characteristic peaks in the pH range of 10 to 11.5 suggests that the electrocatalytic reduction of H_2O_2 is not efficient. The appearance of minimal peaks is observed at pH=12, while the best results with an intense reduction peak and a maximal current value are obtained at pH=13.

Several studies have emphasized the importance of a high pH level in the buffer solution for efficient catalysis of H_2O_2 by transition metal oxide catalysts during the electrochemical process. This leads to an increased cathodic peak current density [69], [75]. Typically, a 0.1 M NaOH or KOH solution suffices to ensure a favorable catalytic response. The presence of OH^- ions, generated from oxyhydroxide products, plays a crucial role in the diffusion process within the nanostructured layer. This enhances the conductivity of the oxyhydroxide, surpassing that of the hydroxide, and promotes a more efficient transfer of charge towards the wire substrate. Consequently, applying a negative potential activates the Co_3O_4 electrode in an alkaline solution, enabling successful detection of H_2O_2 [75].

The stability of the electrode was evaluated over multiple cyclic voltammetry (CV) cycles (n=50), as shown in Figure 3e. It can be observed that the cycles overlap, and the current peak value only undergoes slight changes over time. This indicates that the electrode stabilizes after the second scanning cycle. The minor differences observed during the first scanning cycle can be attributed to wetting processes occurring within the highly porous nanostructured layer.

Figure 3f depicts the electrochemical impedance spectroscopy (EIS) curve obtained before and after adding 0.5 mM H_2O_2, accompanied by the corresponding equivalent circuit. Notably, the absence of characteristic semicircles, formed by the circuit elements' RC components, can be explained by the low charge transfer resistance and the prevalence of Warburg diffusion over other processes within the electrochemical system. The diffusion coefficient, derived from the graph, was found to be $1.237 \cdot 10^{-7}$ $cm^2 \cdot s^{-1}$. The active surface area of the electrode can be determined using Equation (9) from the Randles–Sevcik equation [76]–[78].

$$I_p = (2.69 \cdot 10^5) n^{3/2} A C^* D^{1/2} v^{1/2}, \quad (9)$$

where Ip represents the redox peak current (in μA), n expresses the number of electrons transferred during the redox reaction, A is the effective surface of the working electrode (cm^2), C* is the concentration of NaOH in buffer solution ($mol \cdot cm^{-3}$), D is the solution diffusion coefficient (NaOH = $1.237 \cdot 10^{-7}$ $cm^2 \cdot s^{-1}$) and ν represents the scan rate (100 $mV \cdot s^{-1}$). The calculated electrochemically active surface area was found to be 4.684 cm^2, while the active surface area of the wire without considering the contribution of the nanostructures was 1.256 cm^2. The presence of porous honey-comb-like nanostructured arrays of Co_3O_4, coupled with the large specific surface area, allows for easy electrolyte access and H_2O_2 diffusion towards the

highly available active sites, leading to an improved electrocatalytic process. Typical graphs of the amperometric response for the nanostructured Co_3O_4 electrodes are presented in Figs. 4a and 4b.

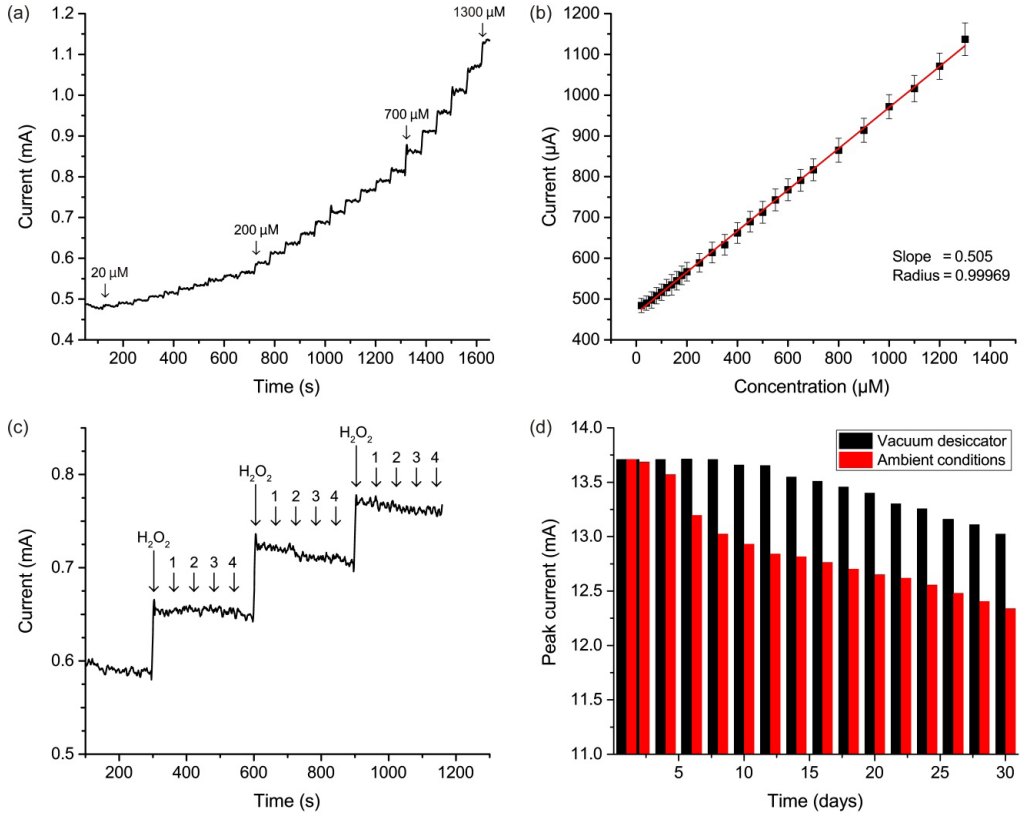

Fig. 4. The figure show (a) the i-t response of the nanostructured Co_3O_4 electrode in 0.1 M NaOH buffer solution with gradual addition of H_2O_2 at concentrations ranging from 20 to 1300 µM, and (b) the corresponding sensor calibration curve. Three steps for the interference study of the nanostructured Co_3O_4 electrode in 0.1 M NaOH is shown in (c) with stepwise addition of H_2O_2 at concentrations ranging from 100 to 300 µM, along with the most common interfering substances, such as (1) ascorbic acid, (2) uric acid, (3) glucose, and (4) NaCl. (d) The stability study is presented for the nanostructured Co_3O_4 samples stored under ambient conditions and in a vacuum desiccator.

Upon addition of H_2O_2, the amperometric response of the nanostructured Co_3O_4 electrode exhibits rapidity, stability, and high sensitivity. The current attains a steady-state value in a matter of seconds and remains relatively constant until the next dose of H_2O_2 is introduced, thereby generating a well-defined current step that is appropriate for determining the current response. The calibration curve depicting the correlation between the catalytic current values and the H_2O_2 concentration in the buffer solution is presented in Fig. 4b. A linear relationship between the current and the concentration of H_2O_2 was observed in a broad range of concentrations spanning from 20 to 1300 µM, with a correlation coefficient (R) of 0.99969. The sensitivity of the Co_3O_4 electrode was determined to be 505.11 $\mu A \cdot mM^{-1}$. By considering a signal-to-

noise ratio of 3, the calculated limit of detection (LOD) was found to be 1.05 μM.

According to publications [79]–[81], for effective milk antibacterial treatment, a minimal H_2O_2 concentration of 0.01 %, which is equivalent to 2.9 mM, is used. This value significantly exceeds the calculated LOD for our sensor. If we consider biomedicine as a potential application of our sensor, the likely range of H_2O_2 in biological fluids (in particular, in blood plasma) is in the range 1–5 μM [82, 83], which is also within the sensitivity of this sensor. This proves the significance of the sensor described in this article for food analysis and further potential applications in healthcare and diagnostics. This sensor can also be successfully used to determine concentrations that are obviously lower than calculated LOD value. In this case, a standard sample recovery test is performed and for this purpose the samples are spiked with different amounts of H_2O_2 above the detection threshold.

To ensure effective application in the analysis of complex analytes, it is crucial to establish high selectivity for the sensor. To achieve this, the selectivity of the Co_3O_4 wire electrode was assessed using four interferents: ascorbic acid, uric acid, glucose, and NaCl. These compounds are commonly present in biological fluids and food products, and are often encountered alongside H_2O_2 in clinical and pharmaceutical applications. They may potentially cause false increasing of amperometric response due to their oxidizing nature and ability to interact with Co_3O_4 nanostructures. Figure 4c shows the amperometric response after introducing 0.1 mM H_2O_2 and 0.1 mM interferent sequentially. The response does not surpass the background noise value, indicating that the nanostructures are not sensitive to these substances and thus confirming the high selectivity of the sensor towards H_2O_2 detection.

To evaluate the long-term stability of the nanostructures, the samples were stored under ambient conditions (20 °C, 40 % relative humidity) for one and four weeks, and CV measurements were taken every two days to assess the stability of the nanostructured electrode by measuring the degree of reduction of the current peak value. The results showed that the signal level remained not less than 95 % of the initial value for samples stored for one week, but decreased to 90 % of the initial value for samples stored for four weeks at ambient condition. Previous studies have suggested that storing CuO and ZnO nanostructures in a vacuum desiccator can significantly reduce sample degradation, so a similar experiment was conducted for Co_3O_4. After a week of storage in the desiccator, the samples did not lose their original electrochemical properties at all, and after a month of storage, they retained 95 % of the initial value of the signal (as shown in Fig. 4d). SEM was used to investigate the influence of storage time on the morphology of the samples, and the results showed no visual changes in the morphology of the nanostructures even after four weeks of storage under ambient conditions. Therefore, it can be concluded that the decrease in sensor sensitivity is mainly due to the adsorption and binding of atmospheric moisture by the developed surface of nanostructures, and this effect can be reduced by storing samples in a vacuum or by preliminary annealing at a temperature of about 100 ºC.

The exceptional stability of these electrodes enables their preparation for future use and the effective preservation of unused electrodes. It is worth emphasizing that the utilization of these electrodes is highly environmentally sustainable and does not contribute to additional waste generation, unlike plastic chips and polymer substrates. The employed electrodes can be easily cleansed of the nanostructured layer through chemical methods or grinding, while the underlying wire can be resurfaced with new nanostructures, enabling its reuse. The results of this study are comparable to those of several published studies where cobalt oxide nanostructures were used for electrode modification for H_2O_2 detection (as summarised in Table 1).

Table 1. Analytical Performance of the Obtained Co_3O_4 Compared to Other Reported Cobalt Oxide Based H_2O_2 Sensors

Electrode	Morphology of nanostructures	Linear range (μM)	Sensitivity ($\mu A \cdot mM^{-1}$)	LOD (μM)	Source
Co_3O_4/GCE	Hollow-sphere	0.4–2200	120.55	0.105	[68]
CoO-CoS/NF	Sheet-like	2–954	590	0.890	[69]
Co_3O_4–rGO/GCE	Wire-like	15–675	456	2.4	[72]
Co-MOF/GCE	Powder	5–9000	83.10	3.76	[73]
Co_3O_4/GCE	Nanocolumns	100–2000	-	0.28	[75]
Co_3O_4 SPCE	Nanourchins	0.1–50	24	0.145	[70]
Co_3O_4@CNBs/GCE	Nanoparticles	0.01–359	-	0.00232	[74]
Co_3O_4 NPs/GE	Nanoparticles	-	-	0.0217	[84]
Co_3O_4/FeWire	Nanowires	20–1300	505.11	1.05	This work

The comparison table reveals that the sensitivity of the electrode discussed in this study is among the highest when compared to other sources. Although the limit of detection (LOD) value is relatively low, there are sources with both higher and lower values than the one reported in this article. However, this is not a significant drawback as the high sensitivity of the material holds the potential for achieving a lower LOD by optimizing the design of a customized electrochemical cell, increasing the working surface area of the electrode, and implementing additional mathematical processing techniques. Furthermore, the spike method described earlier can be employed to determine concentrations below the detection limit.

It is important to emphasize that even with the current performance, the electrode is already suitable for its intended applications since the normal levels of hydrogen peroxide in biological and pharmaceutical samples generally exceed the detection threshold.

Another notable advantage of our electrode compared to others is its accessibility, low cost, and ease of manufacturing. The fabrication methodology eliminates the need for expensive conductive polymers, complex matrices, and costly glassy carbon electrodes (GCE). These factors make our approach highly attractive for potential mass production, promoting wider accessibility to this technology. Furthermore, it is worth emphasizing that most of the sources mentioned employ a surface nanostructuring method that involves applying pre-synthesized nanoparticles in powder form. However, this approach can lead to challenges in achieving repeat-

ability due to the uneven distribution of nanoparticles in the solution and weak adhesion to the electrode surface. In contrast, our novel approach eliminates these drawbacks by utilizing hydrothermal synthesis directly on the electrode surface. This results in a strong, orderly, and uniform epitaxial coating, ensuring enhanced performance and reliability.

The analysis of actual samples using amperometry is documented in Table 2. To account for potential H_2O_2 levels below the detectable range in milk and lens storage solution samples, various quantities of H_2O_2 within a concentration range above the detection threshold were added to each sample. A standard test for sample recovery was then carried out. The findings highlight the electrode's remarkable recovery rate, achieving over 95 % recovery in all instances. Furthermore, the relative standard deviation for the three samples of each spiked concentration remained below 5 %.

Table 2. Results of Determination of Hydrogen Peroxide in Real Milk and Lens Storage Samples

Milk				Contact lens storage solution			
Added (μM)	**Found (μM)**	**Recovery (%)**	**RSD (%) (n = 3)**	**Added (μM)**	**Found (μM)**	**Recovery (%)**	**RSD (%) (n = 3)**
0	-	-	-	0	-	-	-
10	9.51	95.1	5.5	10	9.67	96.7	5.3
25	24.08	96.3	5.1	25	23.89	95.6	5.5
50	47.91	95.8	4.7	50	47.88	95.8	4.4
100	96.25	96.3	4.3	100	97.65	97.7	4.8

If we compare the results obtained in this experiment for the Co_3O_4 nanostructures with the results of previous studies for the CuO nanostructures [85], we can see that cobalt oxide nanostructures show a slightly better sensitivity and long-term stability result; however, its characteristics largely coincide with the CuO coating and likely depend on the geometry and properties of the electrochemical cell. Wire electrodes coated with both oxides are resistant to mechanical and chemical influences and are also characterized by high repeatability in the manufacturing process. However, the position (voltage) of the characteristic peak responsible for the reaction of H_2O_2 with Co_3O_4 nanostructures differs from that for CuO, making it possible to use both oxides in the further development of a multisensor suitable for use in healthcare and food analysis. Multisensor will increase the sensitivity and accuracy of the meaurement compared to using a single working electrode due to cross sensitivity of various metal oxides, as well as expand the areas of application and the list of analyzed analytes supplementing the list of obtainable electrodes with other metal oxides (for example, NiO, TiO_2, ZnO, Fe_3O_4 and others). Applying cross sensitivity also make it possible to detect several analytes simultaneously and study their interactions in real samples with a complex composition.

5. CONCLUSIONS

This article presents the synthesis of a nanostructured coating composed of Co_3O_4, using the hydrothermal method directly on the surface of Fe wire electrode and its practical application as a working electrode for the electrochemical detection of H_2O_2 in real samples with a complex chemical composition. The resulting coating exhibits high homogeneity and excellent adhesion to the iron wire, ensuring its mechanical and chemical resistance during sample processing and electrochemical measurements. The nanostructured Co_3O_4 coating displays a honeycomb-shaped surface, which exhibits significant peroxidase-like electrocatalytic activity, enabling the detection of H_2O_2 with high sensitivity over a wide range of concentrations. The study demonstrates that the morphology of the nanostructures is strongly dependent on the precursor's chemical composition. Thus, the chloride anions provide the formation of fiber-like nanostructures, while the acetate anions under similar growth conditions provide the formation of thin petal-like nanostructures of Co_3O_4. It has been found that fiber-like nanostructures of Co_3O_4 have better sensory characteristics compared to petal-like samples and are more efficient for electrochemical detecting of H_2O_2. It has also been determined that the efficiency of this sensor increases with an increase in the scanning speed and an increase in the pH of the buffer solution.

The resulting electrode exhibits a linear current response over a wide concentration range of 20 to 1300 μM, with a sensitivity of 505.11 $\mu A \cdot mM^{-1}$ and a calculated LOD of 1.05 μM. The electrochemically active surface area is determined to be 4.684 cm^2. Interference tests reveal that the sensor is highly selective, with no electrochemical response to the most common interfering substances. The long-term stability study shows that the signal level remains at 95 % of the initial current value after one week and at 90 % after four weeks of storage under ambient conditions. However, the electrode lifespan can be significantly improved by storing it in a vacuum desiccator until they are needed. In this case, the signal level remains at 100 % of the initial value after one week and at 95 % after four weeks.

The milk and lens storage liquid analysis has demonstrated a high recovery rate of over 95 %, indicating that this sensor is suitable for quantitative and qualitative deermination of H_2O_2 in real samples with complex compositions.

Further research will be aimed at studying this sensor for healthcare applications to analyse changes in the concentration of H_2O_2 in biological fluids (in particular, in blood plasma). Since our research group has already had an experience in creating similar sensors based on other metal oxides (in particular, CuO, Fe_3O_4, NiO), the next promising application will be the integration of this sensor into a multisensor system. The use of a multisensor will increase the sensitivity compared to the use of each oxide separately due to cross-sensitivity and will also expand the range of possible analytes and will allow samples of a more complex composition to be studied. It will also be possible to target the detection of several analytes simultaneously, which is very important in the field of healthcare for monitoring certain diseases.

ACKNOWLEDGEMENTS

The research has been supported by ESF Project No. 8.2.2.0/20/I/003 "Strengthening of Professional Competence of Daugavpils University Academic Personnel of Strategic Specialization Branches 3rd Call".

REFERENCES

1. Dhara, K., & Mahapatra, D.R. (2019). Recent Advances in Electrochemical Nonenzymatic Hydrogen Peroxide Sensors Based on Nanomaterials: A Review. J. *Mater. Sci., 54*, 12319–12357. https://doi.org/10.1007/s10853-019-03750-y
2. Mohanan, P.V., Sangeetha, V., Sabareeswaran, A., Muraleedharan, V., Jithin, K., Vandana, U., & Varsha, S.B. (2021). Safety of 0.5% Hydrogen Peroxide Mist Used in the Disinfectiongateway for COVID-19. *Environ. Sci. Pollut. Res. Int., 28* (47), 66602–66612. https://doi.org/10.1007/s11356-021-15164-y
3. SCCP (Scientific Committee on Consumer Products). (2007). *Opinion on Hydrogen Peroxide, in its Free Form or when Released, in Oral Hygiene Products and Tooth Whitening Products.* Available at https://ec.europa.eu/health/ph_risk/committees/04_sccp/docs/sccp_o_122.pdf
4. National Center for Biotechnology Information. (2022). *PubChem Compound Summary for CID 784, Hydrogen Peroxide*. Available at https://pubchem.ncbi.nlm.nih.gov/compound/Hydrogen-Peroxide
5. Mahaseth, T., & Kuzminov, A. (2016). Potentiation of Hydrogen Peroxide Toxicity: From Catalase Inhibition to Stable DNA-Iron Complexes. *Mutat. Res.: Rev. Mutat. Res. 773*, 274–281. https://doi.org/10.1016/j.mrrev.2016.08.006
6. Schnabel, T., Mehling, S., Londong, J., & Springer, C. (2020). Hydrogen Peroxide-Assisted Photocatalytic Water Treatment for the Removal of Anthropogenic Trace Substances from the Effluent of Wastewater Treatment Plants. *Water Sci. Technol. 82* (10), 2019–2028. https://doi.org/ 10.2166/wst.2020.481
7. Ksibi, M. (2006). Chemical Oxidation with Hydrogen Peroxide for Domestic Wastewater Treatment. *Chem. Eng. J.*, *119* (2–3), 161–165. https://doi.org/10.1016/j.cej.2006.03.022
8. Xu, J., Zheng, X., Feng, Z., Lu, Z., Zhang, Z., Huang, W., ... & Cui, Y. (2021). Organic Wastewater Treatment by a Single-Atom Catalyst and Electrolytically Produced H_2O_2. *Nat. Sustain., 4*, 233–241. https://doi.org/10.1038/s41893-020-00635-w
9. Arefin, S., Sarker, M.A.H., Islam, M.A., Harun-ur-Rashid, M., & Islam, M.N. (2017). Use of Hydrogen Peroxide (H_2O_2) in Raw Cow's Milk Preservation. *J. Adv. Vet. Anim. Res. 4* (4), 371–377. https://doi.org/10.5455/javar.2017.d236
10. Silva, E., Oliveira, J., Silva, Y., Urbano, S., Sales, D., Moraes, E., … & Anaya, K. (2020). Lactoperoxidase System in the Dairy Industry: Challenges and Opportunities. *Czech J. Food Sci. 38*, 337–346. https://doi.org/ 10.17221/103/2020-CJFS
11. Gaikwad, R., Thangaraj, P.R., & Sen, A.K. (2021). Direct and Rapid Measurement of Hydrogen Peroxide in Human Blood Using a Microfluidic Device. *Sci. Rep. 11* (1), 112960 https://doi.org/10.1038/s41598-021-82623-4
12. Totsuka, K., Ueta, T., Uchida, T., Roggia, M.F., Nakagawa, S., Vavvas, D.G., ... & Aihara, M. (2019). Oxidative Stress Induces Ferroptotic Cell Death in Retinal Pigment Epithelial Cells. *Exp. Eye Res. 181*, 316–324. https://doi.org/10.1016/j.exer.2018.08.019
13. Whittemore, E.R., Loo, D.T., Watt, J.A., & Cotman, C.W. (1995). A Detailed Analysis of Hydrogen Peroxide-Inducded Cell Death in Primary Neuronal Culture. *Neurosci. 67* (4), 921–932. https://doi.org/10.1016/0306-4522(95)00108-u

14. Guesmi, F., Bellamine, H., & Landoulsi, A. (2018). H2O2-Induced Oxidative Stress, AChE Inhibition and Mediated Brain Injury Attenuated by *Thymus algeriensis*. *Appl. Physiol. Nutr. Metab.*, *43* (12), 1275–1281. https://doi.org/10.1139/apnm-2018-0107

15. Dev, S., Kumari, S., Singh, N., Bal, S.K., Seth, P., & Mukhopadhyay, C. K. (2015). Role of Extracellular Hydrogen Peroxide in Regulation of Iron Home- Ostasis Genes in Neuronal Cells: Implication in Iron Accumulation. *Free Radic. Biol. Med., 86,* 78–89. https://doi.org/10.1016/j.freeradbiomed.2015.05.025

16. Tabner, B.J., El-Agnaf, O.M.A., Turnbull, S., German, M.J., Paleologou, K.E., Hayashi, Y., … & Allsop, D. (2005). Hydrogen Peroxide Is Generated during the Very Early Stages of Aggregation of the Amyloid Peptides Implicated in Alzheimer Disease and Familial British Dementia. *J. Biol. Chem., 280* (43), 35789–35792. https://doi.org/10.1074/jbc.C500238200

17. Lee, S., Lee, Y.J., Kim, J.H., & Lee, G. (2020). Electrochemical Detection of H_2O_2 Released from Prostate Cancer Cells Using Pt Nanoparticle-Decorated rGO–CNT Nanocomposite-Modified Screen-Printed Carbon Electrodes. *Chemosensors 8* (3), 63. https://doi.org/10.3390/chemosensors8030063

18. Kolbasina, N.A., Gureev, A.P., Serzhantova, O.V., Mikhailov, A.A., Moshurov, I.P., Starkov, A.A., & Popov, V.N. (2020). Lung Cancer Increases H2O2 Concentration in the Exhaled Breath Condensate, Extent of mtDNA Damage, and mtDNA Copy Number in Buccal Mucosa. *Heliyon, 6* (6), e04303. https://doi.org/10.1016/j.heliyon.2020.e04303

19. Abdalla, A., Jones, W., Flint, M.S., & Patel, B.A. (2021). Bicomponent Composite Electrochemical Sensors for Sustained Monitoring of Hydrogen Peroxide in Breast Cancer Cells. *Electrochim. Acta, 398*, 139314. https://doi.org/10.1016/j.electacta.2021.139314

20. Tavakkoli, H., Akhond, M., Ghorbankhani, G.A., & Absalan, G. (2020). Electrochemical Sensing of Hydrogen Peroxide Using a Glassy Carbon Electrode Modified with Multiwalled Carbon Nanotubes and Zein Nanoparticle Composites: Application to HepG2 Cancer Cell Detection. *Microchim. Actam, 187*, 105. https://doi.org/10.1007/s00604-019-4064-7

21. Wu, Y., Guo, T., Qiu, Y., Lin, Y., Yao, Y., Lian, W., ... & Yang, H. (2019). An Inorganic Prodrug, Tellurium Nanowires with Enhanced ROS Generation and GSH Depletion for Selective Cancer Therapy. *Chem. Sci. 10* (29), 7068–7075. https://doi.org/10.1039/c9sc01070j

22. Ahmad, T., Iqbal, A., Halim, S.A., Uddin, J., Khan, A., El Deeb, S., & Al-Harrasi, A. (2022). Recent Advances in Electrochemical Sensing of Hydrogen Peroxide (H_2O_2) Released from Cancer Cells. *Nanomaterials, 12* (9), 1475. https://doi.org/10.3390/nano12091475

23. Maier, D., Laubender, E., Basavanna, A., Schumann, S., Güder, F., Urban, G.A., & Dincer, C. (2019). Toward Continuous Monitoring of Breath Biochemistry: A Paper-Based Wearable Sensor for Real-Time Hydrogen Peroxide Measurement in Simulated Breath. *ACS Sens., 4* (11), 2945–2951. https://doi.org/10.1021/acssensors.9b01403

24. Xie, J., Cheng, D., Zhou, Z., Pang, X., Liu, M., Yin, P., ... & Yao, S. (2020). Hydrogen Peroxide Sensing in Body Fluids and Tumor Cells via In situ Produced Redox couples on Two-dimensional Holey $CuCo_2O_4$ Nanosheets. *Microchim. Acta, 187* (8), 469. https://doi.org/10.1007/s00604-020-04389-2

25. Kakeshpour, T., Metaferia, B., Zare, R.N., & Bax, A. (2022). Quantitative Detection of Hydrogen Peroxide in Rain, Air, Exhaled Breath, and Biological Fluids by NMR Spectroscopy. *Proc. Natl. Acad. Sci. U.S.A. 119* (8), e2121542119. https://doi.org/10.1073/pnas.2121542119

26. Liu, H., Weng, L., & Yang, C. (2017). A Review on Nanomaterial-Based Electrochemical Sensors for H_2O_2, H_2S and NO inside Cells or Released by Cells. *Microchim. Acta, 1847,* 1267–1283. https://doi.org/10.1007/s00604-017-2179-2

27. Perini, J.A.d.L., Silva, B.C.e., Tonetti, A.L., & Nogueira, R.F.P. (2017). Photo-Fenton Degradation of the Pharmaceuticals Ciprofloxacin and Fluoxetine after Anaerobic Pre-treatment of Hospital Effluent. *Environ. Sci. Pollut. Res., 24,* 6233–6240. https://doi.org/10.1007/s11356-016-7416-4

28. Al-Awadie, N.S.T., & Khudhair, A.F. (2015). Determination of Hydrogen Peroxide in Some Local Pharmaceutical Disinfectants by Continuous Flow Injection Analysis via Turbidimetric (T_{180}^{o}) and Scattered Light Effect at Two Opposite Positions ($2N_{90}^{o}$) Using Ayah $4S_{W}$-3D-T_{180}^{o} -$2N_{90}^{o}$ -Solar - CFI Analyser. *Iraqi J. Sci.*, *56* (1C), 577–592.
29. Payal, A., Krishnamoorthy, S., Elumalai, A., Moses, J.A., & Anandharamakrishnan, C. (2021). A Review on Recent Developments and Applications of Nanozymes in Food Safety and Quality Analysis. *Food Anal. Methods*, *14,* 1537–1558. https://doi.org/10.1007/s12161-021-01983-9
30. Chen, Q., Lin, T., Huang, J., Chen, Y., Guo, L., & Fu, F. (2018). Colorimetric Detection of Residual Hydrogen Peroxide in Soaked Food Based on Au@Ag Nanorods. *Anal. Methods, 10,* 504–507. https://doi.org/10.1039/C7AY02819A
31. Navale, D., & Gupta, S. (2019). Detection of Adultered Formalin and Hydrogen Peroxide in Milk. *JLTEMAS*, *8* (8), 19–21.
32. Vasconcelos, H., Matias, A., Jorge, P., Saraiva, C., Mendes, J., Araújo, J., … & Coelho, L.C.C. (2021). Optical Biosensor for the Detection of Hydrogen Peroxide in Milk. *Chem. Proc., 5* (1), 55. https://doi.org/10.3390/CSAC2021-10466
33. Huang, Y., Wang, L., Chen, B., Zhang, Q., & Zhu, R. (2020). Detecting Hydrogen Peroxide Reliably in Water via Ion Chromatography: A Method Evaluation Update and Comparison in the Presence of Interfering Components. *Environ. Sci.: Water Res. Technol., 6,* 2396–2404. https://doi.org/10.1039/d0ew00234h
34. Su, J., Zhang, S., Wang, C., Li, M., Wang, J., Su, F., & Wang, Z. (2021). A Fast and Efficient Method for Detecting H_2O_2 by a Dual-Locked Model Chemosensor. *ACS Omega, 6* (23), 14819–14823. https://doi.org/10.1021/acsomega.1c00384
35. Fong, D., & Swager, T.M. (2021). Trace Detection of Hydrogen Peroxide via Dynamic Double Emulsions. *J. Am. Chem. Soc., 143* (11), 4397–4404. https://doi.org/10.1021/jacs.1c00683
36. Ito, E., Watabe, S., Morikawa, M., Kodama, H., Okada, R., & Miura, T. (2013). Detection of H_2O_2 by fluorescence correlation spectroscopy. In E. Cadenas, L. Packer (eds.), *Hydrogen Peroxide and Cell Signaling, Part A* (pp 135–143). Academic Press: Cambridge, Massachusetts. https://doi.org/10.1016/B978-0-12-405883-5.00008-9
37. Rezende, F., Brandes, R.P., & Schröder, K. (2018). Detection of H_2O_2 with Fluorescent Dyes. *Antioxid. Redox Signal.*, *29* (6), 585–602. https://doi.org/10.1089/ars.2017.7401
38. Teodoro, K.B.R., Migliorini, F.L., Christinelli, W.A., & Correa, D.S. (2019). Detection of Hydrogen Peroxide (H_2O_2) Using a Colorimetric Sensor Based on Cellulose Nanowhiskers and Silver Nanoparticles. *Carbohydrate Polymers, 212*, 235–241. https://doi.org/10.1016/j.carbpol.2019.02.053
39. Zhu, P., Xu, Z., Cai, L., & Chen, J. (2021). Porphyrin Iron-Grafted Mesoporous Silica Composites for Drug Delivery, Dye Degradation and Colorimetric Detection of Hydrogen Peroxide. *Nanoscale Res. Lett., 16* (1), 41. https://doi.org/10.1186/s11671-021-03501-6
40. Moßhammer, M., Kühl, M., & Koren, K. (2017). Possibilities and Challenges for Quantitative Optical Sensing of Hydrogen Peroxide. *Chemosensors*, *5*, 28. https://doi.org/10.3390/chemosensors5040028
41. Gričar, E., Kalcher, K., Genorio, B., & Kolar, M. (2021). Highly Sensitive Amperometric Detection of Hydrogen Peroxide in Saliva Based on N-Doped Graphene Nanoribbons and MnO_2 Modified Carbon Paste Electrodes. *Sensors, 21*, 8301. https://doi.org/10.3390/s21248301
42. Gorduk, O., Gorduk, S., & Sahin, Y. (2020). Fabrication of Tetra-Substituted Copper(II) Phthalocyanine-Graphene Modified Pencil Graphite Electrode for Amperometric Detection of Hydrogen Peroxide. *ECS J. Solid State Sci. Technol., 9,* 06103. https://doi.org/10.1149/2162-8777/ab9c7a
43. Wang, Q., Zhang, X., Chai, X., Wang, T., Cao, T., Li, Y., & Qi, W. (2021). An Electrochemical Sensor for H_2O_2 Based on Au Nanoparticles Embedded in UiO-66 Metal−Organic Framework Films. *ACS Appl. Nano Mater.*, *4* (6), 6103–6110. https://doi.org/10.1021/acsanm.1c00915

44. Bao-Kai, M., Mian, L., Ling-Zhi, C., Xin-Chu, W., Cai, S., & Qing, H. (2020). Enzyme-MXene Nanosheets: Fabrication and Application in Electrochemical Detection of H_2O_2. *J. Inorg. Mater., 35* (1), 131–138. https://doi.org/10.15541/jim20190139

45. Yu, Y., Pan, M., Peng, J., Hu, D., Hao, Y., & Qian, Z. (2020). A Review on Recent Advances in Hydrogen Peroxide Electrochemical Sensors for Applications in Cell Detection. *Chin. Chem. Lett., 33,* (9), 4133–4145. https://doi.org/10.1016/j.cclet.2022.02.045

46. Portorreal-Bottier, A., Gutiérrez-Tarriño, S., Calventea, J.J., Andreu, R., Roldán, E., Oña-Burgos, P., & Olloqui-Sariego, J.L. (2022). Enzyme-like Activity of Cobalt-MOF Nanosheets for Hydrogen Peroxide Electrochemical Sensing. *Sens. Actuat. B Chem., 368,* 132129. https://doi.org/10.1016/j.snb.2022.132129

47. Bollella, P., & Gorton, L. (2018). Enzyme Based Amperometric Biosensors. *Curr. Opin. Electrochem., 10,* 157–173. https://doi.org/10.1016/j.coelec.2018.06.003

48. Olloqui-Sariego, J.L., Calvente, J.J., & Andreu, R. (2021). Immobilizing Redox Enzymes at Mesoporous and Nanostructured Electrodes. *Curr. Opin. Electrochem., 26,* 100658. https://doi.org/10.1016/j.coelec.2020.100658

49. Nestor, U., Frodouard, H., & Theoneste, M. (2021). A Brief Review of How to Construct an Enzyme-Based H_2O_2 Sensor Involved in Nanomaterials. *Adv. Nanopart., 10*, 1–25. https://doi.org/10.4236/anp.2021.101001

50. Sardaremelli, S., Hasanzadeh, M., & Seidi, F. (2021). Enzymatic Recognition of Hydrogen Peroxide (H_2O_2) in Human Plasma Samples Using HRP Immobilized on the Surface of Poly(arginine-toluidine blue)- Fe_3O_4 Nanoparticles Modified Polydopamine; A Novel Biosensor. *J. Mol. Recognit., 34* (11), e2928. https://doi.org/10.1002/jmr.2928

51. Wu, Z., Sun, L.P., Zhou, Z., Li, Q., Huo, L.H., & Zhao, H. (2018). Efficient Nonenzymatic H_2O_2 Biosensor Based on ZIF-67 MOF Derived Co Nanoparticles Embedded N-doped Mesoporous Carbon Composites. *Sens. Actuat. B Chem., 276*, 142–149. https://doi.org/10.1016/j.snb.2018.08.100

52. Heydaryan, K., Kashi, M.A., Sarifi, N., & Ranjbar-Azada, M. (2020). Efficiency Improvement in Non-enzymatic H_2O_2 Detection Induced by the Simultaneous Synthesis of Au and Ag Nanoparticles in an RGO/Au/Fe_3O_4/Ag Nanocomposite. *New J. Chem., 44*, 9037–9045. https://doi.org/10.1039/d0nj00526f

53. Rashed, M.A., Faisal, M., Harraz, F.A., Jalalah, M., Alsaiari, M., & Alsareii, S.A. (2021). A Highly Efficient Nonenzymatic Hydrogen Peroxide Electrochemical Sensor Using Mesoporous Carbon Doped ZnO Nanocomposite. *J. Electrochem. Soc., 168* (2), 027512. https://doi.org/10.1149/1945-7111/abe44b

54. Nishan, U., Niaz, A., Muhammad, N., Asad, M., Shah, A.-u.-H.A., Khan, N., … & Rahim, A. (2021). Non-enzymatic Colorimetric Biosensor for Hydrogen Peroxide Using Lignin-Based Silver Nanoparticles Tuned with Ionic Liquid as a Peroxidase Mimic. *Arabian J. Chem., 14* (6), 103164. https://doi.org/10.1016/j.arabjc.2021.103164

55. Bukkitgar, S.D., Kumar, P.S., Singh, S., Singh, V., Reddy, K.R., Sadhu, V., … & Naveen, S. (2020). Functional Nanostructured Metal Oxides and its Hybrid Electrodes – Recent Advancements in Electrochemical Biosensing Applications. *Microchem. J.*, *159*, 105522. https://doi.org/10.1016/j.microc.2020.105522

56. Chang, Y.S., Li, J.H., Chen, Y.C., Ho, W.H., Song, Y.D., & Kung, C.W. (2020). Electrodeposition of Pore-Confined Cobalt in Metaleorganic Framework Thin Films toward Electrochemical H_2O_2 Detection. *Electrochim. Acta, 347*, 136276. https://doi.org/10.1016/j.electacta.2020.136276

57. Agnihotri, A. S., Varghese, A., & Nidhin, M. (2021). Transition Metal Oxides in Electrochemical and Bio Sensing: A State-of-Art Review. *Appl. Surf. Sci. Adv., 4,* 100072. https://doi.org/10.1016/j.apsadv.2021.100072

58. Tammineni, V.S., Espenti, C.S., Mutyala, S., & Arunachalam, S.V. (2021). Metal oxide-modified electrochemical sensors for toxic chemicals. In A. Pandikumar & P. Rameshkumar (eds.), *Metal Oxides in Nanocomposite-Based Electrochemical Sensors for Toxic Chemicals* (pp. 19–49). Elsevier Science: Amsterdam. https://doi.org/10.1016/B978-0-12-820727-7.00009-4

59. Trujillo, R.M., Barraza, D.E., Zamora, M.L., Cattani-Scholz, A., & Madrid, R.E. (2021). Nanostructures in Hydrogen Peroxide Sensing. *Sensors, 21* (6), 2204. https://doi.org/10.3390/s21062204

60. Alsaiari, M., Younus, A.R., Rahim, A., Alsaiari, R., & Muhammad, N. (2021). An Electrochemical Sensing Platform of Cobalt Oxide@SiO_2/C Mesoporous Composite for the Selective Determination of Hydrazine in Environmental Samples. *Microchem. J., 165,* 106171. https://doi.org/10.1016/j.microc.2021.106171

61. Kogularasu, S., Govindasamy, M., Chen, S.M., Akilarasan, M., & Mania, V. (2017). 3D Graphene Oxide-Cobalt Oxide Polyhedrons for Highly Sensitive Non-Enzymatic Electrochemical Determination of Hydrogen Peroxide. *Sens. Actuat. B Chem., 253,* 773–783. https://doi.org/10.1016/j.snb.2017.06.172

62. Kumarage, G.W.C., & Comini, E. (2021). Low-Dimensional Nanostructures Based on Cobalt Oxide (Co_3O_4) in Chemical-Gas Sensing. *Chemosensors, 9* (8), 197. https://doi.org/10.3390/chemosensors9080197

63. Rabani, I., Yoo, J., Kim, H.S., Lam, D.V., Hussain, S., Karuppasamy, K., & Seo, Y.S. (2021). Highly Dispersive Co_3O_4 Nanoparticles Incorporated into a Cellulose Nanofiber for a High-performance Flexible Supercapacitor. *Nanoscale 13,* 355–370. https://doi.org/doi.org/10.1039/d0nr06982e

64. Fan, Y., Chen, H., Li, Y., Zheng, D.C., & Xue, F.C. (2021). PANI-Co_3O_4 with Excellent Specific Capacitance as an Electrode for Supercapacitors. *Ceram. Int., 47* (6), 8433–8440. https://doi.org/10.1016/j.ceramint.2020.11.208

65. Ibupoto, Z.H., Elhag, S., AlSalhi, M.S., Nur, O., & Willander, M. (2014). Effect of Urea on the Morphology of Co_3O_4 Nanostructures and Their Application for Potentiometric Glucose Biosensor. *Electroanalysis, 26* (8), 1773–1781. https://doi.org/10.1002/elan.201400116

66. Hussain, M., Ibupoto, Z.H., Abbasi, M.A., Nur, O., & Willander, M. (2014). Effect of Anions on the Morphology of Co_3O_4 Nanostructures Grown by Hydrothermal Method and their pH Sensing Application. *J. Electroanal. Chem., 717–718*, 78–82. https://doi.org/10.1016/j.jelechem.2014.01.011

67. Kannan, P., Maiyalagan, T., Marsili, E., Ghosh, S., Guo, L., Huang, Y., … & Jönsson-Niedziolka, M. (2017). Highly Active 3-Dimensional Cobalt Oxide Nanostructures on the Flexible Carbon Substrates for Enzymeless Glucose Sensing. *Analyst, 142*, 4299–4307. https://doi.org/10.1039/c7an01084b

68. Wang, M., Jiang, X., Liu, J., Guo, H., & Liu, C. (2015). Highly Sensitive H_2O_2 Sensor Based on Co_3O_4 Hollow Sphere Prepared via a Template-Free Method. *Electrochim. Acta, 182,* 613–620. https://doi.org/10.1016/j.electacta.2015.08.116

69. Mai, L.N.T., Bui, Q.B., Bachc, L.G., & Nhac-Vu, H.-T. (2020). A Novel Nanohybrid of Cobalt Oxide-Sulfide Nanosheets Deposited Three-Dimensional Foam as Efficient Sensor for Hydrogen Peroxide Detection. *J. Electroanal.l Chem., 857*, 113757. https://doi.org/10.1016/j.jelechem.2019.113757

70. Barkaoui, S., Haddaoui, M., Dhaouadi, H., Raouafi, N., & Touati, F. (2015). Hydrothermal Synthesis of Urchin-like Co_3O_4 Nanostructures and their Electrochemical Sensing Performance of H_2O_2. *J. Solid State Chem., 228*, 226–231. https://doi.org/10.1016/j.jssc.2015.04.043

71. Shahid, M.M., Rameshkumar, P., & Huang, N.M. (2015). Morphology Dependent Electrocatalytic Properties of Hydrothermally Synthesized Cobalt Oxide Nanostructures. *Ceram. Int. 41* (10), 13210–13217. https://doi.org/ 10.1016/j.ceramint.2015.07.098

72. Kong, L., Ren, Z., Zheng, N., Du, S., Wu, J., Tang, J., & Fu, H. (2014). Interconnected 1D Co_3O_4 Nanowires on Reduced Grapheme Oxide for Enzymeless H_2O_2 Detection. *Nano Res., 8* (2), 469–480. https://doi.org/10.1007/s12274-014-0617-6

73. Yang, L., Xu, C., Ye, W., & Liu, W. (2015). An Electrochemical Sensor for H_2O_2 Based on a New Co-Metal-Organic Framework Modified Electrode. *Sens. Actuat. B Chem., 215*, 489–496. https://doi.org/10.1016/j.snb.2015.03.104

74. Xiong, L., Zhang, Y., Wu, S., Chen, F., Lei, L., Yu, L., & Li, C. Co_3O_4 Nanoparticles Uniformly Dispersed in Rational Porous Carbon Nano-Boxes for Significantly Enhanced Electrocatalytic Detection of H_2O_2 Released from Living Cells. *Int. J. Mol. Sci., 23* (7), 3799. https://doi.org/10.3390/ijms23073799

75. Kannan, P., Maiyalagan, T., Pandikumar, A., Guo, L., Veerakumar, P., & Rameshkumar, P. (2019). Highly Sensitive Enzyme-free Amperometric Sensing of Hydrogen Peroxide in Real Samples Based on Co_3O_4 Nanocolumn Structures. *Anal. Methods, 11*, 2292–2302. https://doi.org/10.1039/c9ay00230h

76. Atacan, K.J. (2019). $CuFe_2O_4$/Reduced Graphene Oxide Nanocomposite Decorated with Gold Nanoparticles as a New Electrochemical Sensor Material for L-cysteine Detection. *Alloys Compd., 791*, 391–401. https://doi.org/10.1016/j.jallcom.2019.03.303

77. Demir, N., Atacan, K., Ozmen, M., & Bas, S.Z. (2020). Design of a New Electrochemical Sensing System Based on MoS_2-TiO_2/Reduced Graphene Oxide Nanocomposite for Paracetamol Detection. *New J. Chem., 44* (27), 11759–11767. https://doi.org/10.1039/d0nj02298e

78. Dhulkefl, A.J., Atacan, K., Bas, S.Z., & Ozmen, M. (2020). Ag-TiO_2-Reduced Graphene Oxide Hybrid Film for Electrochemical Detection of 8-hydroxy-2'-Deoxyguanosine as an Oxidative DNA Damage Biomarker. *Anal. Methods, 12* (4), 499–506. https://doi.org/10.1039/c9ay02175b

79. Arefin, S., Sarker, M.A.H., Islam, M.A., Harun-ur-Rashid, M., & Islam, M.N. (2017). Use of Hydrogen Peroxide (H_2O_2) in Raw Cow's Milk Preservation. *J. Adv. Vet. Anim. Res., 4* (4), 371–377. https://doi.org/10.5455/javar.2017.d236

80. Saha, B.K., Ali, M.Y., Chakraborty, M., Islam, Z., & Hira, A.K. (2003). Study of the Preservation of Raw Milk with Hydrogen Peroxide (H_2O_2) for Rural Dairy Farmers. *Pakistan J. Nutrition, 2* (1), 36–42. https://doi.org/ 10.3923/pjn.2003.36.42

81. Dashe, D., Hansen, E.B., Kurtu, M.Y., Berhe, T., Eshetu, M., Hailu, Y., … & Shegaw, A. (2020). Preservation of Raw Camel Milk by Lactoperoxidase System Using Hydrogen Peroxide Producing Lactic Acid Bacteria. *Open J. Anim. Sci., 10,* 387–401. https://doi.org/10.4236/ojas.2020.103024

82. Forman, H.J., Bernardo, A., & Davies, K.J.A. (2016). Corrigendum to "What is the Concentration of Hydrogen Peroxide in Blood and Plasma?". *Arch. Biochem. Biophys., 603*, 48–53. https://doi.org/10.1016/j.abb.2016.05.005

83. Atta, N.F., Gawad, S.A.A., Galal, A., Razik, A.A., & El-Gohary, A.R.M. (2021). Efficient Electrochemical Sensor for Determination of H_2O_2 in Human Serum Based on Nano Iron/Nickel Alloy/Carbon Nanotubes/Ionic Liquid Crystal Composite. *J. Electroanal. Chem., 881*, 114953. https://doi.org/10.1016/j.jelechem.2020.114953

84. Das, R.K., & Golder, A.K. (2017). Co_3O_4 Spinel Nanoparticles Decorated Graphite Electrode: Bio-mediated Synthesis and Electrochemical H_2O_2 Sensing. *Electrochim. Acta, 251,* 415–426. https://doi.org/10.1016/j.electacta.2017.08.122

85. Mihailova, I., Gerbreders, V., Krasovska, M., Sledevskis, E., Mizers, V., Bulanovs, A., & Ogurcovs, A. (2022). A Non-enzymatic Electrochemical Hydrogen Peroxide Sensor Based on Copper Oxide Nanostructures. *Beilstein J. Nanotechnol., 13,* 424–436. https://doi.org/10.3762/bjnano.13.35

sciendo

LATVIAN JOURNAL OF PHYSICS
AND TECHNICAL SCIENCES
2023, N 6

DOI: 10.2478/lpts-2023-0038

GAS DISTRIBUTION SYSTEM OF LATVIA AND ITS TRANSITIONAL CHALLENGES

L. Jansons[1*], I. Bode[2], A. Koposovs[2], N. Zeltins[2], S. Lapuke[1]

[1]Riga Technical University,
Faculty of Engineering Economics and Management,
Institute of the Civil Engineering and Real Estate Economics,
6 Kalnciema Str. 210, Riga, LV-1048, LATVIA
[2]Riga Technical University, Faculty of Civil Engineering,
Institute of Heat, Gas and Water Technologies
6a Kipsalas Str., Riga, LV-1048, LATVIA
*e-mail: leo.jansons@rtu.lv

The future of the European Union's (EU) gas sector and gas distribution systems in particular is under review as a necessity to move away from conventional natural gas is strictly outlined in its strategical energy framework. The main questions of future gas sector layout are largely related to gas decarbonization paths – whether they will include simultaneous transportation, distribution and storage of methane-based and non-methane based renewable gases or not. In general, this question is left for different Member States to decide, because as alternatives to it there are two options – decommissioning of all gas distribution and partially gas transportation and storage systems on the one hand and total replacement of existing gas transportation system with brand new hydrogen transportation and distribution system on the other. The first option leaves only liquified renewable gases (including, hydrogen) that are transported via truck and the second – pipeline transportation and distribution only for hydrogen, limiting methane-based renewable gases to road transportation solutions only.

The Latvian gas distribution system is also facing imminent transformation in foreseeable future; thus, at the moment its sustainability priority is the maintenance of the existing system in a safe and secure manner by improving it in accordance with technical necessities and immediate customer requests. The current research shows two sides of gas distribution system priorities in Latvia – its maintenance and development trends prior to fundamental transformations of gaseous fuel transition and general transitional challenges laying ahead.

Keywords: *Gas distribution, renewable gases, sustainable development, transition challenges.*

1. INTRODUCTION

The European efforts to mitigate climate change will impact every industry, but the speed and direction of that impact are clearer for some industries than others. One of such industries facing the greatest amount of uncertainty is gas transmission, storage and distribution; distribution system operators are the ones maintaining direct communication with the customers. Once considered the providers of a much appreciated environmentally friendly energy source, these companies are now facing challenges and reduced pathways through them. Gas has long been considered a transition fuel, a bridge to a less carbon-intensive future [1], but not always these expectations are fulfilled as expected [2].

There are challenging times ahead for gas distribution as the European Union (EU) progresses towards carbon neutrality in 2050. However, network operators have options available to them – they can divest their assets, run them down safely and profitably, or convert to cleaner gaseous fuels partially or completely. The biggest risk for gas distribution system operators in the EU is that they do not decide which direction to choose in the closest future. Not having a plan in this instance is a plan for inefficient capital allocation and a tougher transition than necessary. In any case, gas distribution networks should be maintained and kept in good working order, and further decisions regarding their reconstruction and sustainability enhancement should be taken for at least short- and mid-term periods [3].

2. THE SITUATION IN THE LATVIAN GAS DISTRIBUTION SYSTEM

Since late 2017, the joint stock company "Gaso" (GASO) has been the only natural gas distribution system operator in Latvia, which ensures the maintenance of the natural gas system, the accounting of natural gas, emergency service activities, development of distribution infrastructure and planning and construction of new distribution gas pipeline networks, as well as attraction of new consumers. GASO operates only in the territory of Latvia; its workforce is made up of 900 qualified employees, and it ensures the supply of gas to 370 thousand consumers in Latvia.

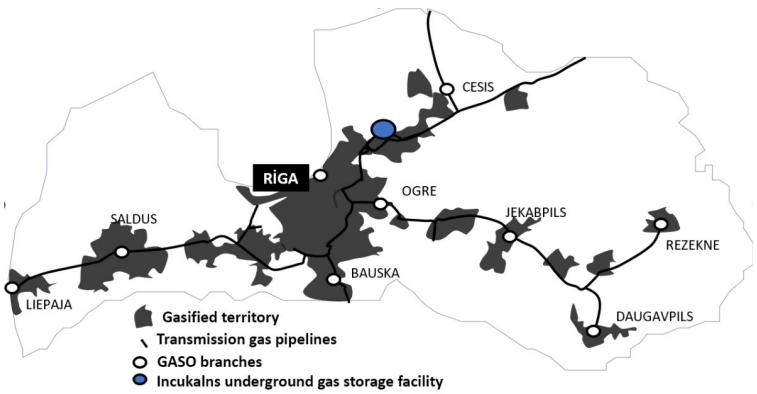

Source: Gaso

Fig. 1. Principal scheme of the Latvian gas distribution system.

The distribution system operator maintains 5442 km of distribution gas pipeline, 163 gas regulating points (GRP) and 1145 cabinet gas regulating points (SGRP). Most of the gas pipelines owned by GASO are located in Riga and its vicinity. In the Latvian gas distribution system, 19 % are high-pressure gas pipelines, 43 % are medium-pressure gas pipelines and 38 % are low-pressure gas pipelines [4]. Their actual lengths by pressure regime are summarised in Table 1.

Table 1. The Length, Pressure Regimes and Materials of the Latvian Distribution Gas Pipelines

Pressure regime	Material	Total length of pipelines, km
High pressure I (<=6 bar)	Polyethylene	172
	Steel	495
High pressure II (<=12 bar)	Steel	190
High pressure III (<=16 bar)	Steel	147
Medium pressure (<=0.1 bar)	Polyethylene	349
	Steel	9
Medium pressure (<=4 bar)	Polyethylene	1294
	Steel	688
Low pressure (<=0.05 bar)	Polyethylene	336
	Steel	1761
TOTAL	**5442**	

Source: GASO

2.1 The Introduction of Biomethane into the System

Given that energy systems in the EU and Latvia will undergo significant changes in the coming years, the share of conventional natural gas in the energy supply of the region will decrease gradually and over a long period of time, while the use of renewable or "green gases" (RG) will increase. The most well-known of these gases is biomethane, which can be produced from local raw materials in every country, including Latvia, and used in the same way as natural gas. The technical solutions and requirements for introduction of biomethane into the distribution system have been approved by the GASO Technical Council in cooperation with the designers and manufacturers of technological equipment, participating in the development of an optimal technical solution.

In 2022, there were 47 biogas production plants in Latvia [5]. Their distribution throughout territories close to gas distribution system networks are even [6], but only several biogas producers have requested technical regulations and plan to invest in biomethane production and subsequent injection of biomethane into the distribution system networks.

There is an assumption that in each of the plant size groups, at least a half of biogas plants will choose to switch their business from the cogeneration of electric power to biomethane production within the coming years. In Latvia, the transitioning of the current biogas power plants to making biomethane can be an important process for those biogas plants whose mandatory procurement period has run out, as well as all for other biogas plants, in view of the expected rise in energy price [5].

Table 2. Latvian Biogas Plants Broken Down by Installed Capacity and Biomethane Potential (01/ 2022)

Installed capacity, MW	Number of biogas plants, 01/ 2022	Biogas for generation of 1 MW of electricity, m^3	Biogas quantity, Nm^3h^{-1}	Theoretical biomethane quantity, Nm^3h^{-1}	Theoretical biomethane energy value, MWh^{-1}
<0.5	6	450	388.8	205.14	2.162
0.5–1.0	19	450	3528.0	1861.5	19.62
1.0–1.5	5	450	1759.5	928.4	9.785
1.5–2.0	8	450	5800.5	3060.6	32.258
2.0–6.5	2	450	2925.0	1543.3	16.266
TOTAL	**40**	**-**	**14401.8**	**7598.94**	**80.091**

Meanwhile, if after withdrawing from the mandatory procurement system, the biogas plant operator decides to continue operating as a producer of biomethane, the nature of the plant cogeneration activities could change. A reduction in operating costs is expected for the biogas plants that transition from selling cogenerated electric power and heat to producing biomethane and selling it, but this requires an initial investment in biomethane purification facilities. As part of manufacturing biomethane, one can add a carbon dioxide (CO_2) collection system to the biomethane purification facility, thus making it possible to efficiently use CO_2 for another purpose before it is returned to nature. Selling the CO_2 could be a source of additional income for biogas plants.

The most active biomethane producers are located in the vicinity of Bauska, where construction projects already have been developed, or their development is at the final stages of construction. Creation of biomethane injection points for gas distribution system is a technically complex and time-consuming undertaking. Its implementation requires an assessment of the potential of biomethane and the distribution gas pipeline system in a particular territory, the development of economic justification, the purchase or rental of immovable property for the construction of injection points and access roads. Currently, GASO does not operate biomethane injection points into the gas distribution system, but, according to its 10-year development plan (Plan), construction of the first such point is planned to be completed in November 2023 [7].

Natural gas systems should be a facilitator of the introduction of biomethane for grid injections and transport sector alike, but the sustainability problems associated with natural gas sometimes negatively affects the perception of biomethane. This is where arguments amongst the renewable sector actors can hinder progress. Biomethane can utilize the existing gas grid and accelerate progress to decarbonization of the overall energy sector beyond just electricity and also decarbonize chemical, such as ammonia and methanol, and steel production. This should be advantageous especially when realizing that in the EU more energy is procured from the natural gas grid than the electricity grid; however, suggestions that biomethane is only greenwashing the natural gas industry, and in doing so extending the lifetime of natural gas, greatly impedes this progress [8].

The Plan also includes distribution system development projects that simultaneously increase security for the continuity of gas supply and combine the loop of a technically separate, local gas supply system, increasing the potential for biomethane to be introduced into the distribution gas pipeline system in regions where such demand exists.

The Energy and Climate Plan is not focused on the development of the hydrogen transmission and distribution infrastructure yet, and before this decision is made, technical assessment of the existing gas distribution system and its suitability for hydrogen transport is required. For this reason, the focus is also on technologies and research related to the use of hydrogen in methane-based gas distribution networks.

2.2 Assessment of Capital Investment Needs

The security of the gas distribution is the highest priority and requires continuous maintenance and restoration of the system, as a result of which GASO invests on average between 8 and 11 million euros (EUR) annually in the development and maintenance of the gas distribution system infrastructure. In 2022, planned investments were reduced due to a significant increase in costs for gas losses, driven by the high natural gas price, resulting in investments falling to EUR 7.16 million. The dynamics of capital investments in gas distribution system between 2018 and 2022 is shown in Fig. 2.

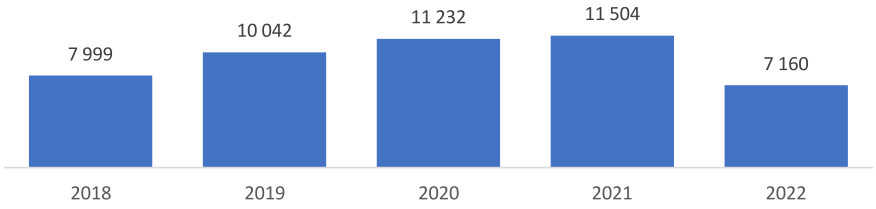

Fig. 2 Capital investments in the natural gas distribution system (2018–2022, EUR).

Given the age of the Latvian gas distribution system, continuous implementation of reconstruction works is an integral part of measures to mitigate appearance of dangerous situations. The exploitation period for individual networks and network equipment may reach up to 55 years and, in order to avoid possible emergencies due to the physical and technical ageing of gas distribution networks, its reconstructions and modernizations are carried out continuously.

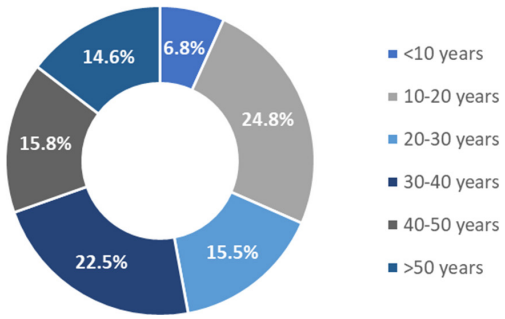

Fig. 3. The gas distribution pipeline breakdown (in %, by age).

GASO is drawing up a capital investment programme for each calendar year, taking into account both exploitation defects and damage detected in distribution networks. While planning the reconstruction investments, the plans of relevant local

and municipal authorities – for instance, reconstruction of the roads and pavement, are also taken into account, which is an economically justified and sustainable action. The necessity to perform repair or restoration of gas pipelines, as well as the amount of necessary reconstruction work is determined on the basis of assessment of the technical condition of the gas pipeline, as well as other factors.

However, currently, not only reconstruction or replacement of existing physical components of distribution gas networks take up a significant portion of investment, also information technology (IT) projects initiated by GASO might be quite resource and labour intensive. The amount of necessary investment in establishment or development of IT systems is determined by carrying out an extensive economic assessment. In certain cases, when IT systems to be put in place are large and complex, a feasibility study is performed, involving, where necessary, a consultancy service provider with expertise in the field in question.

2.3 Dynamics of the Gas Distribution System and IT Solutions

In order to promote development of the Latvian gas distribution system, possible territories of new connections are determined, taking into account location of industrial objects, dynamics of building density, and the planned amount of gas consumption in newly connected objects. Currently, the highest density of distribution gas pipelines and connections is located in Riga and its surroundings; however, some of the populated areas around Riga are still not gasified.

In capital investment projects, the efficiency of investments is decisive. Construction of new distribution gas pipelines in a particular territory is possible if there is customer demand for construction of connections and it is planned to achieve investment efficiency. On average, it is planned to invest about EUR 1 million per year in the development of the system. As a priority, GASO would implement capital investment projects with the highest return on investment, the main condition being a choice of an economically justified technical solution for the development of a new distribution system connections.

Most new consumers of gas are concentrated in Riga and around it, in municipalities such as Marupe, Adazi, Kekava and Ropazi.

The actual breakdown of new connections by cities and their vicinity in recent years has been as follows:

- Riga and its vicinity: 60–65 %;
- Jurmala and its vicinity: 8–10 %;
- Jelgava and its vicinity: 5–8 %;
- Cesis, Liepaja, Ogre, Daugavpils, Jekabpils, Bauska and their vicinity: 3–7 %.

Table 3. The Dynamics of the Latvian Distribution Gas Pipelines (by length (km), pressure regime)

	2018	**2019**	**2020**	**2021**	**2022**
Pressure till 0.05 bar	2064	2069	2089	2095	2097
Pressure 0.05–4 bar	2181	2204	2247	2285	2321
Pressure 4–6 bar	657	661	663	663	666
Pressure 6–12 bar	194	191	191	191	190
Pressure 12–16 bar	147	147	147	147	147
TOTAL	**5243**	**5272**	**5337**	**5381**	**5420**

Source: GASO

Based on the geopolitical situation and support for renewables, the number of new connections fell by 35 % in 2022 in comparison to previous years, with their total installed load reaching 9700 cubic meters per hour (m^3/h). The required load in the technical regulations is 30 % to 40 % higher than that actually installed. According to the Plan, the proportional distribution of new connections by cities and their vicinities is planned to be similar to the number of the previously implemented connections.

The loads of new connections per year is estimated under three development scenarios:

- in the baseline scenario: from 7000 to 8000 m^3/h;
- in the optimistic scenario: from 9000 to 10 000 m^3/h;
- in a crisis scenario: from 5000 to 6000 m^3/h.

The baseline scenario for new connections has been calculated on the basis of actual total load of new connections in 2022 and the dynamics of new connections in previous five years. In the crisis scenario, however, new connection loads are forecast taking into account overall trends in reduction of gas consumption and, consequently, demand for new connections. The optimistic scenario predicts an increase in the load of new connections, based on possible demand for new connections in special economic zones such as Valmiera, Jekabpils, Jelgava and Bauska, as GASO has participated in the planning of territories of these economic zones and evaluation of the maximum permissible loads have been performed there.

Based on the issued technical regulations, the largest new connection capacities in 2024 and 2025 are planned in Riga and its vicinity (Adazi, Ropazi and Marupe), in Bauska and its vicinity (Iecava), Ogre and its vicinity (Salaspils), Daugavpils and its vicinity (Daugavpils) and Liepaja and its vicinity (Liepaja). Construction of new entry points of a system in the next two to five years is possible in the vicinity of Bauska, Riga, Daugavpils and Ogre.

Overcoming some energy transition barriers in gas distribution sector requires new system capacity, but not necessarily new ideas. Scaling success in this category is akin to a physical form of IT system integration. Examples include digital tools that help optimize energy grid storage and dispatch, or better connecting supply and demand in industrial clusters. This is happening at a macro level, such as initiatives integrating consortia and supply chains to provide hydrogen to multi-industry business clusters, as well as at a smaller – distribution system operator scale, building *energy-as-a-service* platforms for different categories of customers [9].

Today IT systems and solutions play an important role in ensuring efficient operation of any enterprise; therefore, it is planned to continue to promote introduction of digital solutions for ensuring operational and business needs of gas distribution operator in Latvia as well. IT capital investments are based on investments in information systems development projects and their licenses, the modernization of the catholic protection and SCADA system, as well as on smart development. The introduction of digital solutions into the distribution system has historically been the lowest priority, which still requires significant investments for the development of new and enhancement of existing IT systems. The exchange of information within systems is not always automated, human resources are often used where IT solutions can be a valid substitute for them [10].

Continuing to improve and automate gas distribution system processes can not

only improve customer service, but also overall company's efficiency. The IT investment provisions for gas distribution system operator have been prepared with the following key priorities in mind:

- improvement and modernization of a controller management system and smart metering;
- development and modernization of a customer service system;
- development and modernization of internal process management systems.

The modernization of the controller management system, including the equipping of gas distribution technological objects with telemetry, contributes significantly to increasing operational safety of the distribution network as a whole. It is intended to optimize accessibility of gas equipment remote operating parameters and rapid detection of non-standard situations.

The introduction of smart meters for the accounting and control of household gas consumption can also help provide accurate information on gas consumption for households, detection of non-standard situations, and provide information on actual gas losses.

In accordance with Directive 2009/73/EC of the European Parliament and of the Council of 13 July 2009 concerning common rules for the internal market in natural gas and repealing Directive 2003/55/EC, the EU members are required to ensure the deployment of smart metering systems in order to promote the active participation of consumers in the electricity and gas markets [11]. In comparison with electricity, there is no deadline for gas to provide all consumers with smart metering systems. The number of smart gas meters installed in Europe reached 45.9 million units in 2021. It is also expected for it to continue to grow at a compound annual growth rate of about 8.7 % between 2021 and 2027, reaching 75.9 million units at the end of the period [12].

Taking into account a fact that the installation of smart meters can significantly improve energy efficiency and also ensure more efficient operation of gas distribution systems, GASO also is continuing replacement of existing gas meters with smart metering equipment. Currently, the distribution system operator is providing installation of smart meters for households with projected maximum hourly consumption above 10 m^3/h. For household consumers with lower maximum hourly consumption using gas for heating and hot water preparations, smart meters have so far only been installed as part of pilot projects and technical trials. Even if accurate and timely information on the natural gas consumed is essential for the distribution system operator, such solutions have not been widely implemented in this customer segment because of significant associated capital costs. Basically, this is due to the problem of ensuring a power supply of the communication equipment built into smart meters. The alternative is to create own data transmission infrastructure or provide a powerful power source (battery) to keep communication modem running for at least several years [7].

With a rapid development of mobile operator infrastructure, data transmission technologies like NB-IoT are becoming increasingly available and ensuring that the meter communication battery has a sufficient lifespan. Gas distribution system operator has launched a broader project on the introduction of smart meters for households using gas in heating and hot water preparation through GPRS and NB-IoT (where it is provided) data transmission infrastructures. For implementation of the project, the infrastructure has been estab-

lished for secure data transmission, processing, as well as work is being carried out so that consumption information is available at GASO customer portal to all consumers for whom a smart meter has been installed, thus ensuring more accurate information regarding the gas consumed. From 2024 till 2033, 5720 smart meters are planned to be installed for the largest household gas customers every year [7].

Accuracy of data provided by the smart metering systems is also a point of particular importance. By introducing smart meters to the largest household customers, it will be possible to maintain accuracy of information throughout the lifecycle of the metering equipment, to ensure higher quality of data and to prevent potential security risks in a timely manner. At the same time, it will help eliminate excessive administrative burden by receiving consumption-related information remotely.

Last but not least, the introduction of smart meters to a wider range of customers would solve the problem of unauthorized entry of gas distribution system operator employees into the gasified site for sole purpose of meter reading [13].

Expected benefits of smart metering in households with the biggest gas consumption are the following:

- time savings (performing less manual control; processing customers' meter readings);
- more accurate consumption balance calculations;
- providing consumers with precise data that can help analyse their gas consumption habits;
- in emergency situations, a possibility to collect and predict consumption-related information timely and accurately;
- a possibility to detect gas theft;
- avoiding the receipt of inaccurate readings caused by human error [14].

3. TRANSITION CHALLENGES FASED BY GAS DISTRIBUTION NETWORKS

Governments around the EU are implementing policies that could shorten the runway for gas distribution networks. There is a growing movement to ban gas connections in new premises and electrify the existing ones. The Netherlands is ahead of this trend; new houses there have not been allowed to connect to the gas network since 2018 and all homes will be completely natural gas free by 2050. However, the Dutch government plans to ban new installations of fossil fuel-based heating systems from 2026 and mandate the use of heat pumps or connections to heat networks instead. With more than 70 % of households in the Netherlands relying on gas for heating, plus extensive use of gas in agriculture for greenhouses, the government will have a challenging task of supporting suppliers, installers and homeowners to adjust to the new requirements [15]. The British government also plans to ban gas boilers in new homes, which are responsible for the majority of residential gas consumption in the UK. To be more precise, under the government's current plans, there is a gas and oil boiler ban in new build homes from 2025 [16]. However, by giving up conventional gas heating, customers first and foremost give up the comfort, environmental friendliness and security of supply provided by conventional gas heating equipment – one of the most modern, if not the most modern, individual heating equipment available. In

addition, giving up conventional gas today also means giving up RGs – biomethane and hydrogen – in the future.

The worst-case scenario of this trend for gas distribution networks is a total decline – once a fear for electricity distribution networks. It was believed that consumers would disconnect the grid after installing solar PV, raising the fixed cost for other households, increasing the incentive for them to install solar and batteries and disconnect as well. As number of households that use gas is considerably lower than households of electricity consumers, gradual reduction in connection number would impact the gas distribution system more severely than electricity distribution grids.

If enough households electrify and disconnect from gas networks, the cost for the remaining households would need to be increased to cover the fixed cost of the network. Potentially combined with a carbon price or other disincentives to use fossil fuels, this would increase the cost of connected households, who, at the same time, will be incentivized to disconnect. Eventually, there could be too few households and businesses on the network to make it viable. Whether fixed costs could be increased depends on local regulation, but either way declining connections would be bad news for gas distribution networks operators.

3.1 Biomethane Availability and Long Lead-Time for Hydrogen Conversion

Ungraded and purified biogas, otherwise known as biomethane, could be regarded as an ideal solution to save existing gas networks and enhance their usability in the future. It can be produced from different sources, including organic waste, and is a direct substitute for natural gas. The gas distribution networks can continue operating as normal by adding different gas injection points, and consumers will be supplied with RGs instead of conventional natural gas.

As for April 2023, Europe reached a total of 1322 biomethane-producing facilities. 299 new biomethane plants were added in Europe, which was 30 % more than in 2021. In comparison with 2021, the number of biomethane plants in Europe steeply increased: from 483 plants in 2018, 729 – in 2020 to 1023 – in 2021. Europe is already producing over 3.5 BCM of biomethane. This represents a production increase rate of 20 % in 2021. An even bigger increase is expected for 2023 where, despite consolidated data not being disclosed, estimations confirm a significant rise in the number of plants and production shares. Additionally, the data show that over 75 % of the current plants are already connected to the transport or distribution networks. Regarding feedstock use, a clear trend towards agricultural residues, organic municipal solid waste, and sewage sludge is visible. From 2017 onwards, almost no new plants were established to run on monocrops [17].

Unfortunately, sustainable biogas and biomethane sources within reasonable proximity of gas networks are often limited. Also, the organic feedstocks needed for their production are likely to be in increasing demand as all sectors decarbonize. For example, airlines and mining companies may start competing for organic feedstocks to produce their own sustainable drop-in replacement fuels. Methane capture from landfills is another option, but it may be more economical for landfill operators to use methane onsite to produce electricity and heat than to sell it into gas distribution networks. Consequently, biomethane is limited in its potential to decarbonize gas sector and gas distribution networks. How-

ever, a degree of biomethane blending can reduce the carbon intensity of gas distribution networks while longer-term solutions like hydrogen switching are implemented [18].

Hydrogen – a supposed future of all decarbonized gas networks, including gas distribution systems, is a specific RG gas due to its low ignition energy, wide flammability range, promotion of the embrittlement of steel, and its high coefficient of permeation for polymers. The fracture toughness and failure elongation of pipe steels are strongly impacted by hydrogen embrittlement, whereas yield stress and ultimate strength are moderately impacted [19]. As structural defects are always present in solid materials, metallic imperfections such as gaps, dislocations, grain boundaries, pores, and inclusions serve as trapping sites for hydrogen. Alloying elements form hydrides with carbon and sulfur, which can act as trapping sites. They interact with hydrogen to form gases such as hydrogen sulfide, which generate blisters in the material. The transport rate of hydrogen through the material is decreased by hydrogen trapping. Therefore, in these trapping sites, further diffusion of hydrogen becomes difficult. In a metallic system, hydrogen transport can become extremely complex [20], [21].

Even if hydrogen could be the most viable solution for gas distribution system survival well beyond the EU energy and economy decarbonization date of 2050, there would be several major challenges with exchanging methane-based RGs for hydrogen in distribution networks.

The first issue relates to pipelines and associated infrastructure. In the Eastern European countries such as Latvia, historically distribution pipelines are made from steel, but in recent thirty years more than a third is replaced by polyethylene, which can transport hydrogen without obvious problems at the maximum pressure of 16 bar in the Latvian gas distribution networks [22]. There may be hydrogen leakage issues at joints and valves, but that can be resolved with modest investment [20].

Recent studies carried out by GASO specialists and scientists address the steel pipeline sustainability and exploitation period prolongation possibilities, bearing in mind gaseous fuel diversification reality, when not only methane-based RGs will be introduced into the gas distribution system [3], [4].

Gas transportation networks are a larger and more uncertain problem. Their pipelines are typically made of steel, which is subject to embrittlement if used to transport hydrogen. Early pilots show that this may be less of an issue than initially suspected, except for older pipes, but more research needs to be conducted to prove or disprove the primary acquired data. Anyway, significant investment will be needed to increase compressor capacity to accommodate hydrogen, where partial solution to the problem might be hydrogen production located maximally close to major consumption points – even more, close to locations, where the transmission network connects to the distribution network. Hydrogen can also be transported via truck or pipelines that have been retrofitted or newly built [23].

A larger problem is that the equipment and appliances connected to the gas distribution network were not built to handle hydrogen. One can mix in about 20 % hydrogen by volume without issue, but that is only 6 % by energy content. Cadent in the UK ran a 20 % hydrogen mix trial over 18 months with 100 houses and 30 university buildings on a private gas network without incident [24], [25].

To accelerate hydrogen transportation in gas networks till 100 %, everything connected to the network needs to be made

hydrogen-ready before the actual transition takes place. As gas appliances typically are exploited for 10–25 years, the actual transition cannot be made until a couple of decades after a legally binding hydrogen-ready regulation is introduced, unless assets are to be stranded. If such a wide-ranging transition is to occur, strong government leadership is needed, and gas distribution operators should be acting quickly to work with the relevant governments to introduce necessary legislation and make the necessary technical adjustments of the system.

If hydrogen usage has rather long, yet sporadic history in industrial processes, there is practically no use of it in the household sector. It is yet to be seen whether households will be comfortable using hydrogen at a regular basis. This should be addressed from the safety and communication perspectives [26].

Perhaps the largest challenge facing gas distribution networks is a lack of incentives for timely transformation. Gas networks are typically heavily regulated businesses with very specific incentives in place. These incentives are typically designed to manage critical assets efficiently and safely over very long periods, not to act pre-emptively on disruptions facing the entire industry [27].

3.2 Other Development Options of Gas Distribution Networks

Gas distribution networks have three main developmental options, which are divesting, running down the assets, or converting to RGs, eventually hydrogen. There is also the option to do nothing, but that increases a stranded asset risk.

Divestment is a common approach taken to fossil fuel assets. For instance, between 2016 and 2019, the British national grid divested its gas distribution network and reinvested the proceeds into other areas. They have since continued to shift away from gas and towards lower-carbon assets [28]. However, divesting fossil fuel assets is increasingly being looked upon as an unsustainable solution, as divesting from entire sectors – passing carbon-intensive assets from public markets to private markets – will not get the energy sector to carbon neutrality. The possibility is that assets might be sold to companies with poorer governance, ultimately increasing the amount of greenhouse gases they emit over their lifetime. Divestment is the reasonable option only in case if the gas distribution in certain regions is about to be ceased to exist as such, and no investment needs into keeping it for RGs are foreseen.

To some extent, existing gas distribution networks could be treated as a cash source, reinvesting profits into green growth – both related and non-related to gaseous fuel sector. Doing this well requires taking a different approach to standard asset management. Safety standards and regulatory requirements still need to be met, but all investment decisions need to be made with a shorter and more uncertain asset lifetime in mind. For example, where a pipeline with a 40 or 50-year asset life might have previously been used, an alternative, cheaper material with a 20-year lifetime might be used instead. Most companies struggle to take such an approach, as it is not particularly motivating to lead or work for a company that is being run down. If a company is going to choose this option it needs to think carefully about culture, incentives and organisational structure to ensure it is effective. If an asset manager has an electricity distribution network overlapping their gas network, they might proactively electrify customers to retain the revenue.

However, if gas distribution networks are to be used in the future, retaining their assets in a decarbonized economy, all RGs,

and hydrogen in particular, is likely the best option. Biomethane would be even better if it could be reliably and economically sourced, but that is unlikely to be the case for most networks [29].

As stated above, a network cannot convert to 100 % hydrogen until everything connected to that network is ready for the actual transition. Therefore, it is at the utmost importance to mandate that all appliances and equipment installed on the network are hydrogen-ready well before a network is converted.

Then it will take a couple of decades for all appliances to naturally turn over. During that time, it will become increasingly untenable for businesses to continue to sell and consume conventional gas. Therefore, it is important that gas distribution operators start working with regulators immediately to prepare for RG centred future. Only when governments do not see gas sector and, particularly, gas distribution sector decarbonization as meaningful, they may try to reduce emissions through complete gas bans or further electrification incentives.

However, proactive gas distribution operators may reduce the pressure on governments to take such a drastic action and buy themselves time to set to choose further development path: offsets, biomethane (methane-based RGs) blending/hydrogen blending or complete transition to hydrogen distribution.

4. CONCLUSIONS

The only possibility for gas distribution networks not only to survive energy transition, but also to make themselves viable and necessary in a new energy policy reality, is to serve diversified gas flows and deliver as big percentage of RG as possible.

In order to do so, a necessity to maintain and, to some extent, expand the existing gas distribution infrastructure is one of the most important issues. To make sure that maintenance is carried out in a timely manner and with up-to-date and technically sound solutions for changing a gaseous fuel landscape, gas distribution system investment needs to be planned for at least short or mid-time periods. As historical dominance of methane-based gaseous fuels, including RGs, might be seriously challenged by the new forms of gaseous fuels – first and foremost, hydrogen, the upgrade of gas distribution systems should be in line with general and local gas grid decarbonization trends.

The Latvian gas distribution system is being developed strictly in line with urgent necessities and technical realities of the day in order to ensure a safe, secure and affordable delivery of gas to final consumers, as well as to ensure system longevity in a changing gas delivery landscape.

Transitional challenges of the Latvian gas distribution system are centred on its future function in the national economy and energy system, as only three options for any gas distribution company remain in a long run to follow: namely, assets divestment, assets safe and profitable run down, and transition to cleaner methane and non-methane based gaseous fuels.

Currently, Latvia is not exploiting its biomethane injection into gas distribution grid potential, as at the moment none of biogas plants are equipped with biomethane production facilities and connections to a gas distribution grid. The possibility remains that the first such project will finalize in late 2023.

At the same time, bearing in mind that biomethane is not the last transitional step in the gas sector, the Latvian gas distribution operator, as many its EU counterparts, must be prepared to gradual transition from methane-based gaseous fuels to methane-based gaseous fuels and hydrogen mix with currently unknown percentage of hydrogen in it.

ACKNOWLEDGEMENTS

This research has been funded by the Latvian Science Council's fundamental and applied research programme project "Development of Model for Implementation of Sustainable and Environmentally Friendly Last-Mile Distribution Transportation Services in Latvia" (TRANS4ECO), project No. lzp-2022/1-0306, 01.01.2023.- 31.12.2025.

REFERENCES

1. Gürsan, C., & de Gooyert, V. (2021). The Systemic Impact of a Transition Fuel: Does Natural Gas Help or Hinder the Energy Transition? *Renewable and Sustainable Energy Reviews, 138*. https://doi.org/10.1016/j.rser.2020.110552
2. IEA. (2020). *The Oil and Gas Industry in Energy Transitions.* Available at https://iea.blob.core.windows.net/assets/4315f4ed-5cb2-4264-b0ee-2054fd34c118/The_Oil_and_Gas_Industry_in_Energy_Transitions.pdf
3. Koposovs, A., Jansons, L., Bode, I., Zemite, L., & Dzelzitis, E. (2023). Technical condition assessment framework for steel underground gas distribution pipelines in Latvia. In *Proceeding of 2023 IEEE 64rd International Scientific Conference on Power and Electrical Engineering of Riga Technical University (RTUCON).* Riga, Latvia.
4. Koposovs, A. (2023). *Sadales gāzesvadu sistēmu tehniskā stāvokļa novērtēšanas metodoloģija diversificētam gāzes sastāvam*. Promocijas darba projekts.
5. Plume, L., & Plume, I. (2023). *Analysis of Factors Influencing Energy Efficiency of Biogas Plants.* Available at https://www.tf.lbtu.lv/conference/proceedings2023/Papers/TF150.pdf
6. Savickis, J., Zemite, L., Zeltins, N., Bode, I., Jansons, L., Dzelzitis, E., … & Ansone, A. (2020). The Biomethane Injection into the Natural Gas Networks: The EU's Gas Synergy Path. *Latvian Journal of Physics and Technical Sciences, 57* (4), 34–50. DOI: 10.2478/lpts-2020-0020
7. Gaso. (2023). *Dabasgāzes sadales sistēmas attīstības plāns 2024-2033*.
8. IEA Bioenergy. (2021). *Perspectives on Biomethane as a Transport Fuel within a Circular Economy, Energy, and Environmental System*. Available at https://task37.ieabioenergy.com/wp-content/uploads/sites/32/2022/02/IEA_transport_T37_END_HIGH.pdf
9. Bain&Company. (2023). *Energy and Natural Resources Report 2023*. Available at https://www.bain.com/globalassets/noindex/2023/bain_report_energy_and_natural_resources_2023.pdf
10. Savickis, J., Zemite, L., Jansons, L., Bode, I., Dzelzitis, E., Broks, A., & Vempere, L. (2020). The Development of the Smart Gas Distribution: General Trends and the Latvian Context. *Latvian Journal of Physics and Technical Sciences, 57* (6), 23–39. DOI: 10.2478/lpts-2020-0031
11. Directive 2009/73/EC of the European Parliament and of the Council of 13 July 2009 concerning common rules for the internal market in natural gas and repealing Directive 2003/55/EC. Available at https://eur-lex.europa.eu/legal-content/EN/ALL/?uri=celex%3A32009L0073

12. Spencer, J. J. (2020). *Europe's Smart Gas Meter Penetration Reached 38% in 2021*. Available at https://www.smart-energy.com/industry-sectors/smart-meters/europes-smart-gas-meter-penetration-reached-38-in-2021/
13. La.lv. (2020). *Kāpēc "Gaso", izbūvējot dabasgāzes pieslēgumu, prasa uzstādīt patēriņa skatītājus* ēku ārpusē*? 33.* Available at https://www.la.lv/kapec-gaso-izbuvejot-dabasgazes-pieslegumu-prasa-uzstadit-paterina-skatitajus-eku-arpuse
14. Savickis, J., Zemite, L., Bode, I., & Jansons, L. (2020). Natural Gas Metering and its Accuracy in the Smart Gas Supply Systems. *Latvian Journal of Physics and Technical Sciences, 57* (5), 39–50. DOI: 10.2478/lpts-2020-0026
15. EiBI. (n.d.). *The Netherlands to Ban Fossil Fuel Installations from 2026*. Available at https://eibi.co.uk/news/the-netherlands-to-ban-fossil-fuel-heating-from-2026/
16. EDF. (n.d.). *UK Gas Boiler Ban – Everything You Need to Know*. Available at https://www.edfenergy.com/heating/advice/uk-boiler-ban
17. EBA. (2022). *Statistical Report 2022. Tracking Biogas and Biomethane Deployment across Europe*. Available at https://www.europeanbiogas.eu/wp-content/uploads/2022/12/EBA-Statistical-Report-2022_-Short-version.pdf
18. Zemite, L. Jansons, L., Zeltins, N., Lappuke, S., & Bode, I. (2023). Blending Hydrogen with Natural gas/biomethane and Transportation in Existing Gas Networks. *Latvian Journal of Physics and Technical Sciences, 60* (5), 43–55. DOI: 10.2478/lpts-2023-0030
19. Pluvinage, G., & Capelle, J. (2022). Risks Associated with the Use of Hydrogen as an Energy Carrier or Source. *Journal of Energy and Power Technology, 4* (3). doi:10.21926/jept.2203029
20. Thompson, A.W., & Bernstein, I.M. (1983). Stress Corrosion Cracking and Hydrogen Embrittlement. Metallurgical Treatises. *Metallurgical Society of AIME – 1983*
21. Jansons, L., Bode, I.,Zemite, L., Zeltins, N., Geipele, I., & Kiesners, K. (2022). Securing Sustainable Energy Future: Green Hydrogen as a Part of Gaseous Fuel Diversification Risk Management Strategy. *Latvian Journal of Physics and Technical Sciences, 59* (4), 53–70. DOI: 10.2478/lpts-2022-0033
22. Latvijas Standarts. (2011). *Dabasgāzes sadales sistēmas un lietotāja dabasgāzes apgādes sistēmas ar maksimālo darba spiedienu līdz 1,6 MPa (16 bar) ekspluatācija un tehniskā apkope. 1. daļa: Vispārīgās prasības (LVS 445-1:2011).* https://www.lvs.lv/lv/products/29043
23. Orlova, S., Mezeckis, N., & Vasudev, V. P. K. (2023). *Compression of Hydrogen Gas for Energy Storage: A Review. Latvian Journal of Physics and Technical Sciences, 60* (2), 4–16. DOI: 10.2478/lpts-2023-0007
24. The Guardian. (2023). *Cheshire Villagers will not be Forced to Join Hydrogen Energy Trial*. Available at https://www.theguardian.com/business/2023/mar/30/people-cheshire-village-not-forced-join-hydrogen-energy-trial-whitby
25. Zemite, L. Backurs, A., Starikovs, A., Laizans, A., Jansons, L., Vempere, L., … & Broks, A. (2023). A Comprehensive Overview of the European and Baltic Landscape for Hydrogen Applications and Innovations. *Latvian Journal of Physics and Technical Sciences, 61* (3), 33–54. DOI: 10.2478/lpts-2023-0016
26. British Gas. (2023). *Hydrogen Boilers: Everything You Need to Know.* Available at https://www.britishgas.co.uk/the-source/greener-living/hydrogen-boilers.html
27. Energy Ireland. (2023). *Transforming the Gas Network with Renewable Gases*. Available at https://www.energyireland.ie/transforming-the-gas-network-with-renewable-gases/
28. Reuters. (2023). *UK's National Grid to Sell Further 20% Stake in Gas Unit.* Available at https://www.reuters.com/business/energy/uks-national-grid-sell-further-20-stake-gas-unit-2023-07-19/
29. Eker, S., & van Daalen, E. (2015). A Model-Based Analysis of Biomethane Production in the Netherlands and the Effectiveness of the Subsidization Policy under Uncertainty. *Energy Policy, 82*. https://doi.org/10.1016/j.enpol.2015.03.019

sciendo

LATVIAN JOURNAL OF PHYSICS
AND TECHNICAL SCIENCES
2023, N 6

DOI: 10.2478/lpts-2023-0039

ADDITIVE MANUFACTURING OF TI-6AL-4V WITH CARBON NANOTUBE COMPOSITE MATERIAL

A. Vevers*, A. Kromanis

SIA "Metal 3d"
15 a Mukusalas Str., Riga, LV-1004, LATVIA
*e-mail: info@metal3d.lv

This research is dedicated to investigating whether mechanical properties of Ti-6Al-4V (Titanium Grade 5) base material for additive manufacturing processes can be improved by addition of carbon nanotubes in the base material. Based on other research results with other materials, the assumption was made that reinforcing Ti-6Al-4V material with carbon nanotubes should improve mechanical properties of the base material by 15–20 % in the additive manufacturing process. The research was divided in two steps, the first one was to investigate pure Ti-6Al-4V material and find optimal additive manufacturing processing parameters, which could maintain necessary quality standards and achieve material density levels higher than 98 % and tensile strength higher than 1000 MPa. The second part was to mix base powder with carbon nanotubes and using previously obtained processing parameters print test samples to investigate how a carbon nanotube concentration in a base powder would influence mechanical properties of the base material.

Keywords: *3D printing, additive manufacturing, carbon nanotubes (CNTs), grade 5, tensile strength, Ti-6Al-4V, titanium.*

1. INTRODUCTION

Titanium alloys are characterised by low density, high strength-to-mass ratio, good corrosion resistance and excellent fracture toughness [1]–[3]. Titanium alloys also show exceptional biocompatibility finding their use in medicine, especially in biomedical materials [4], [5]. From all titanium alloys, Ti-6Al-4V is the most widely used titanium alloy for manufacturing of parts used in aerospace, marine, biomedical, chemical and even automotive industries because of aforementioned properties [6], [7]. The Ti-6Al-4V is marked differently depending on the standard. The European standard ISO 5832 defines the marking of titanium alloy with the Ti6Al4V. The Ger-

man standard DIN 17851 means the same alloy as TiAl6V4, while the French standard BS 7252-3 defines it as TA6V4. In the US standard ASTM B 265, titanium alloy is described as R56400 or in the US standart AMS 4928, titanium alloy is described as Grade 5 [8].

Aerospace, biomedical and automotive industries require complex components, manufacturing of which using conventional methods is challenging. Hence, additive manufacturing (AM) or technology of 3D printing is finding its way as an advanced manufacturing method allowing to produce complex shaped components with little or almost zero waste [9]–[11].

Additive manufacturing (AM) is an advanced manufacturing process in which parts are fabricated by adding materials layer by layer. It has great potential in revolutionising the manufacturing industry by allowing rapid prototyping, customised production, flexible design, complicated parts, and simplified supply chain [12]–[17]. When mechanical properties are essential, powder bed fusion (PBF) process utilising direct metal laser melting (DMLS) or selective laser melting (SLM) is one of the most suitable AM processes to produce functional components [18]–[23]. In PBF utilising DMLS or SLM, a powder dose is distributed horizontally by a spreader to form a powder layer, then a region in the powder layer is scanned selectively by a laser beam and the powder layer of loose particles is selectively sintered or melted forming a thin solid layer. By repeating the powder spreading and layer sintering or melting, a solid part is manufactured from the powder.

Even with utilisation of AM, the industry demands not only more complex parts but also demands more advanced materials. AM similar to a powder metallurgy offers a possibility to create various powder composites – various metal compositions or various metal-nonmetal compositions. But development of such composites poses various challenges. The mechanical properties of composites are functions of the manufacturing processes. Mainly, correctly chosen manufacturing parameters and manufacturing methods will influence the properties of the final product – carbon nanotube metal matrix composite [24]. Hence, it is very important to search for correct techniques in order to develop composites with necessary requirements.

Carbon nanotubes are currently considered to be the most promising material admixture in additive production. Carbon nanotubes are cylindrical structures made up of carbon atoms. The carbon atoms in nanotubes are interconnected in the same way as in hexagonal graphite planes of one atomic thickness, but these planes are “curled” into extremely miniature (1 nanometre to a few tens of nanometres in diameter) tubes that can reach a few centimetres in length. The ends of the tubes are usually closed by hemispherical “heads”. At present, there are some studies in the additive manufacturing in the addition of carbon nanotubes to the base material, but most studies have been carried out using aluminium as the base material.

One study on additive manufacturing of carbon nanotubes reinforced metal matrix composites was performed at Nanjing University [25]. In this study, a selective laser melting process (SLM) was used to fabricate an aluminium material reinforced with carbon nanotubes. The microstructure and mechanical properties of the material were considered in this study. The results showed that the importance of the selected parameters in the AM was very important. Aluminium – AlSi10Mg – was chosen as the base material. Composite was built by addition 0.5 % of the total mass of carbon nano-

tubes. The highest material density was achieved with 350 W laser power and 2.0 m/s laser feed speed. Comparing the results, which included comparison of the mechanical properties of the same base material without the addition of carbon nanotubes, it was concluded that the samples with the addition of carbon nanotubes showed an increase in tensile strength of about 20 %. Samples without the addition of nanotubes reached a tensile strength of 350 MPa, while samples with an increase in carbon nanotubes reached a tensile strength of 420 MPa. The elongation increased from 5.5 % to 8.5 %. At the same time, the research points out that the laser speed may influence the tensile strength and elongation as well [25]. Another large-scale study developed in this field was the study on composite materials for metal and carbon nanotubes conducted at the University of Dayton [26]. The study examined various base or matrix materials – aluminium, copper, stainless steel. The study considered different methods of mixing metal powder and carbon nanotubes, as well as the benefits of carbon nanotubes. The results showed an interesting trend that some materials required heat treatment after the additive production process to obtain an effect from carbon nanotubes. For example, for stainless steel 17-4, the composite material of powder and nanotubes showed the same mechanical properties as the standard base material, but a 20 % increase was obtained during heat treatment, which was similar to the study with aluminium material discussed above.

The study also points out that the key to success is a dispersion of the carbon nanotube within the metal matrix, which is complicated to achieve with existing technologies. The study indicates that dry mixing or wet mixing techniques were best in achieving dispersion of the carbon nanotube. Use of ionic processes or surfactants was not successful in achieving dispersion. The study also includes economics of manufacturing research concluding that the use of carbon nanotubes does not produce significant cost increase. The study motivates to proceed with further research and development from achieved Technological Readiness Level (TRL) 3 and to utilise commercial raw materials and additive manufacturing processing equipment as well as to develop the entire process industrially scalable [26]. When embedding carbon structures in metals using a laser, e.g., for surface cladding or additive manufacturing, a number of aspects needs to be considered to prevent thermal degradation. One of such aspects is that C-structures quickly thermally degrades (e.g., sublimate or fly off as a gas) when illuminated by the processing laser. Therefore, indirect melting of the metal surrounding the C-structures is required. Another aspect is that the density of C-structures is low and has high buoyancy in liquid metals, thereby requiring proper fixation during processing. C-structures have poor wetting properties, which can either lead to exposure to processing light or alternatively be surrounded by solidified melt after processing. The metal coating of C-structures prevented the C-structures from direct laser irradiation and, hence, sublimation [27]. Another publication discusses processing of graphene as well as carbon nanotubes, including their use in design of carbon nanotube metal matrix [28]. It does not disclose information on carbon nanotube titanium matrix composites, but does address common difficulties in manufacturing such matrix composites. The primary challenge is obtaining a uniform and homogeneous dispersion. Carbon nanotubes always tend to agglomerate cluster formation due to a large surface area and a tubular structure. Also, it exhibits a non-wetting property with the molten

metal, which leads to agglomeration.

Another challenge of carbon nanotube is retaining its structure along with the chemical stability when processed at high temperature and stressed condition. The publication states that uniform distribution of carbon nanotubes in the metal matrix is the main criteria for the suc- cessful processing and it includes minimal damage to carbon nanotube physical structure. It also notes that mechanical properties deteriorate at higher concentrations of carbon nanotubes due to agglomeration [28].

2. EXPERIMENTAL PROCEDURE

2.1. Ti-6Al-4V Powder for Ti-6Al-4V-CNT Composite

Ti-6Al-4V powder was used for experiments was Sandvik Osprey® Ti-6Al-4V powder for additive manufacturing. Chemical composition of Ti6Al4V according to ASTM F2924-14 is given in Table 1 [29]. Powder size is 20–50 micrometres, which is the average diameter of the powder particle within the powder.

Table 1. Chemical Composition (Nominal), wt%, for Ti6Al4V (Grade 5) according to ASTM F2924-14

Ti	Al	V	Fe	O	C	N	H	Y	Others, each	Other, total
Balance	5.50-6.75	3.5-4.5	<0.3	<0.20	<0.08	<0.05	<0.015	<0.005	<0.10	<0.40

2.2. Carbon Nanotubes for Ti-6Al-4V-CNT Composite

Ti-6Al-4V powder was supplemented by carbon nanotube (CNT) powder resulting in Ti-6Al-4V-CNT composite. CNT powder used in this research consisted of single wall nanotubes. The CNT powder was produced by OcSiAl Europe – TUBALL SWCNT 01RW02M0005 80 % in a powder form. Graphene nanotubes, or single wall carbon nanotubes, are graphene sheets rolled into a tube. Their unique physical properties make them a universal additive that can be used in 70 % of all base materials to improve their specific properties. Despite the similarity in their names, single wall and multi wall carbon nanotubes differ in their properties and in the effects they have on materials, just like graphene (a single layer of carbon atoms) differs from graphite (multiple layers of carbon atoms).

2.3. Mixing of Ti-6Al-4V-CNT Composite

Two mixing methods were investigated in this research. The first method to mix Ti-6Al-4V powder with carbon nanotube powder was the ultrasonic mixing method. In the beginning, the testing was performed with dry powder material, but the ultrasonic mixer could not mix dry materials sufficiently well. Suspension was produced using isopropyl. In the beginning, mixing was done using small CNT concentration - 0.1 %, then concentration was increased to 0.5 %. After mixing, an additional step was to evaporate isopropyl so that dry Ti-6Al-4V-CNT composite was obtained. This

mixing method did not provide acceptable results because even with mixing time longer than 30 min, powder was not homogenous. It was possible to see that CNTs were layering in Ti-6Al-4V base powder (See Fig. 1).

Fig. 1. Ultrasonic mixer (left) and uneven distribution of CNT within Ti-6Al-4V powder (right).

The second method of mixing included Ti-6Al-4V-CNT powder mixing with the three-dimensional or centrifugal powder mixing machine XIAMEN TMAX-SWH-2000 as seen in Fig. 2. This powder mixing machine is mainly designed for mixing of different density and different particle size powder materials to high uniformity. It can also be used for mixing solid with liquid. It has a three dimensional mixing motion, which ensures homogeneous mixing of materials with different density. Machine has a two-litre tank and it can maintain a maximum of 60 revolutions per minute.

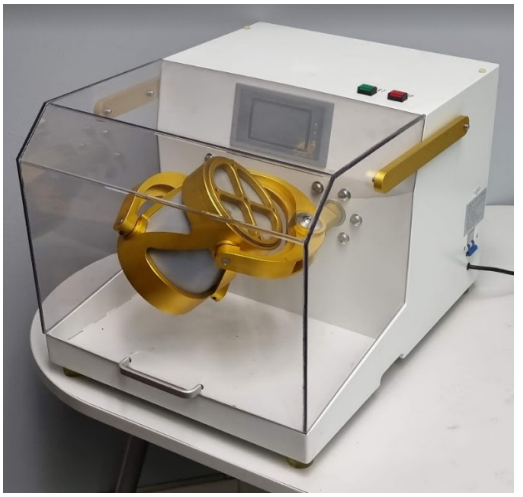

Fig. 2. Centrifugal mixing machine.

The best results were achieved by the second mixing method using a mechanical centrifugal mixer. Tank is moved in infinite motion, which helps evenly distribute or mix the powder. Program which proved the best results was 15 min mixing in one direction

and 15 min mixing in the opposite direction. Machine has a two-litre tank, which was optimal for mixing 2 kg of Ti-6Al-4V-CNT composite powder. Additionally two steel balls were added in the mixing container, which helped fuse carbon nanotubes with Ti-6Al-4 powder (see Fig. 3). To protect the powder during the mixing process, the mixing tank was filled with argon inert gas. Even with CNT concentrations higher than 0.5 weight%, powder was mixed very homogenous and it was almost impossible visually to spot the difference between pure base Ti-6Al-4V material and CNT mix.

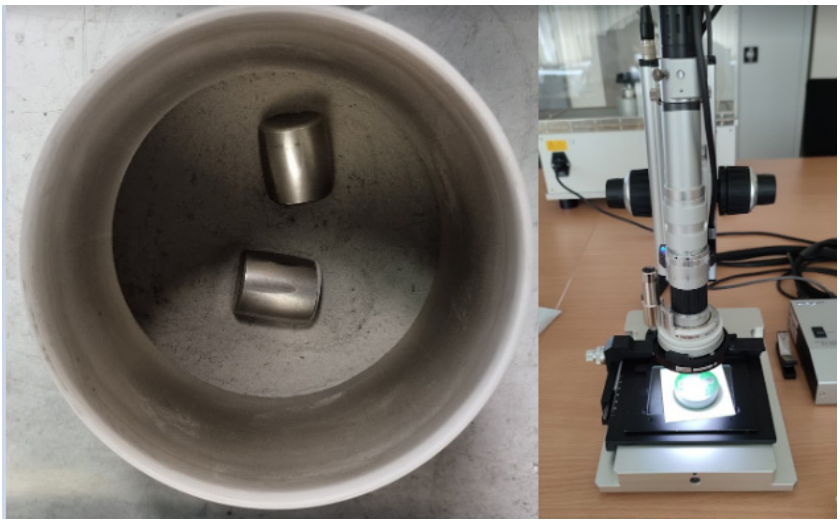

Fig. 3. Centrifugal mixer tank with additional steel cylinders (left) and Mytotoyo microscope for microstructure analysis (right).

In centrifugal mixing, the following mixing parameters were tested – mixing speed and mixing time. Testing was done with one CNT mix concentration (2 grams on 1500 grams of Ti-6Al-4V powder), but with different mixing parameters (mixing speed from 10 to 60 RPM, and mixing time from 10 to 30 minutes) – see Table 2. Initially, the mixing speed was set to 10 RPM and mixing time was set to 10 min. After investigation, the same mix proceeded to mix for additional 10 min, checked for quality, and again mixed for the next 10 min. Then the next mix was made and mixing was done following the same procedure, but with higher mixing speed, which was set to 30 RPM. Since there is no objective way to describe mixing quality, then two main aspects for quality were scattering and homogeneity. Scattering was inspected in the whole mixing tank to identify whether CNTs were dispersed in the whole volume and not concentrated in one point or region and homogeneity was inspected to observe how evenly CNTs were dispersed. With a small mixing speed it was observed that CNT did not reach the whole volume of metal powder and with small mixing time it was possible to observe that CNTs tangled with each other and there were some bigger bundles which did not disperse in metal powder. The best results were achieved with maximum mixing speed 60 RPM and mixing time of 30 min. With these parameters CNTs were evenly dispersed in the whole mixing tank and there were not any tangled CNTs which could be observed after sieving.

Table 2. Mixing Parameters for Centrifugal Mixing Method to Obtain Optimal Mixing Regime

CNT (g)	Ti6Al4V (g)	Mixing speed (RPM)	Mixing Time (min)	CNT weight%
2	1500	10	10	0.1
2	1500	10	20	0.1
2	1500	10	30	0.1
2	1500	30	10	0.1
2	1500	30	20	0.1
2	1500	30	30	0.1
2	1500	60	10	0.1
2	1500	60	20	0.1
2	1500	60	30	0.1

Upon finding an optimal mixingregime – mixing speed of 60 RPM for 30 min – various CNT concentrations were tested starting from 0.1 weight% till 3.3 weight% as seen in Table 3. After each mixing, a qualitative analysis was performed similar to the one, which was used for identifying mixing regimes. In addition, each Ti-6Al-4V-CNT composite powder was not only visually tested but it was also tested on the 3D printer bed for its recoating properties. As a result, it was concluded that the CNT concentration that was suitable for 3D printing, especially for the powder recoating, was in a range of 0.1 to 0.5 weight%.

Table 3. Mixing Parameters for Centrifugal Mixing and Testing Results for Each CNT Concentration

MIX No.	CNT (g)	Ti6Al4V (g)	Mixing speed (RPM)	Mixing Time (min)	CNT weight %	Notes
1	50	1500	60	30	3.3	Impossible to use in additive manufacturing
2	2	1500	60	30	0.1	Suitable for powder recoating
3	3	1500	60	30	0.2	Suitable for powder recoating
4	4	1500	60	30	0.3	Suitable for powder recoating
5	6	1500	60	30	0.4	Suitable for powder recoating
6	8	1500	60	30	0.5	Suitable for powder recoating
7	9	1500	60	30	0.6	Problems with powder recoating
8	10	1500	60	30	0.7	Problems with powder recoating
9	12	1500	60	30	0.8	Problems with powder recoating
10	15	1500	60	30	1.0	Problems with powder recoating

2.4. 3D Printing Using Selective Laser Melting

The 3D printer used for AM was Aurora Labs Titanium Pro S1 machine. This 3D printer utilises powder bed fusion-laser process. Moreover, this Aurora Labs Titanium Pro S1 machine was modified from its original design by replacement of the laser. Aurora Labs Titanium Pro S1 laser system was replaced with a MaxPhotonics 200W-300L fibre laser. Maximum laser power of the system is 250W. Focal distance is 75 mm. Laser spot size is 90 micrometres. Build envelope is 200x200x500 mm. Layer thickness can be varied from 30 to 100 micrometres. Laser travel speed can be adjusted in the range of 0–100 mm/s.

The main goal of this research was

to investigate how CNT could improve Ti-6Al-4V material mechanical properties. CNT concentration was increased step by step and specimens were printed with each level of CNT concentration for tensile strength tests. Based on the first stage of the research [30], specimens were printed with the following processing parameters – layer thickness of 0.07 mm, laser travel speed of 80 mm/s, hatch spacing of 0.15 mm and laser power of 90W. From each batch with different CNT concentration, 3D printed specimens were tensile strength tested straight after the 3D printing process and after the heat treatment process. Microstructure of printed specimens was analysed using Mytotoyo microscope for microstructure analysis (see Fig. 3). Microstructure analysis allowed observing CNT inclusions (Fig. 4) fully enclosed or fused within the base material.

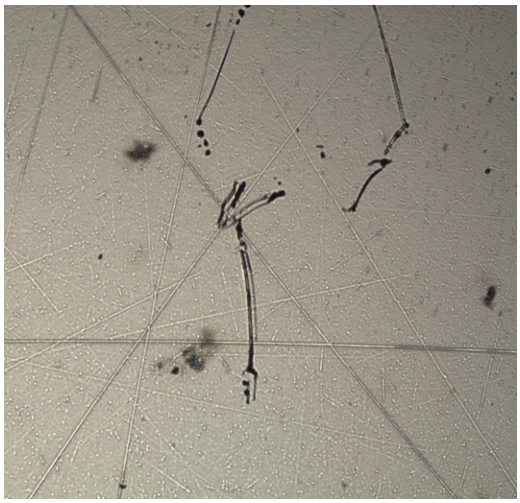

Fig. 4. Polished specimen with CNT inclusions.

2.5. Heat Treatment of 3D Printed Specimens

Heat treatment of 3D printed specimens was performed in the Nabertherm RHTC 80-710/15 heat treatment furnace. It is a compact tube furnace with SiC rod heating and integrated switchgear and controller. Maximum temperature range is 1500 °C. The furnace is designed to perform a heat treatment process in an inert gas or vacuum environment, which is advisable for heat treatment of titanium alloys. Temperature for heat treatment was set to 1000 °C for a period of 1 hour, which was followed by cooling down in the same furnace. Heating gradient was set to 5 °C/minute. The aim of the heat treatment was to analyse how the heat treatment influnced tensile strenght of the specimens. The results are discussed in the next section.

2.6. Tensile Strength Testing of 3D Printed Specimens

Tensile strength tests were performed on Zwick/Roell Z150 testing machine under displacement control at a rate of 1.5 mm/min. This speed approximately corresponds to a strain rate of 2.7 %/min. Optical extensometer from Zwick was used for strain measurement as seen in Fig. 5. The gauge length of the extensometer was set to 17 mm.

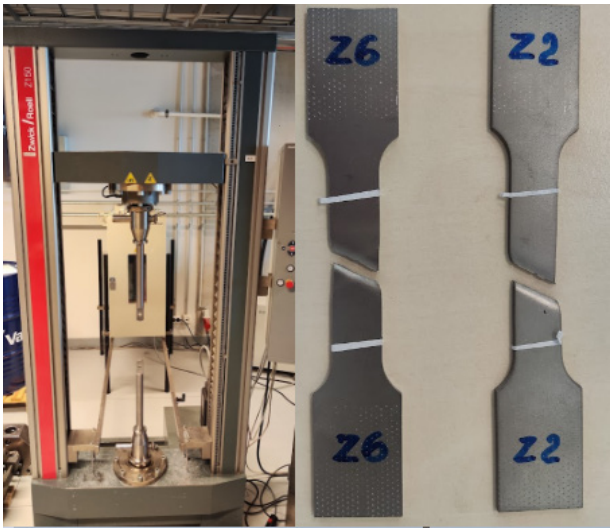

Fig. 5. Tensile strength testing machine and tested specimens with white lines for optical extensometer.

Table 4. Average Tensile Strength Results for Each CNT Concentration

No.	CNT concentration (weight%)	Heat treatment process	Average tensile strength (MPa)	Average Elongation (A%)
1	0 – base material	No	985	3.0
2	0 – base material	Yes	990	7.0
3	0.1	No	1017	2.9
4	0.1	Yes	1031	6.5
5	0.2	No	1011	2.8
6	0.2	Yes	1010	6.6
7	0.3	No	1009	2.9
8	0.3	Yes	1020	5.5
9	0.4	No	1010	3.0
10	0.4	Yes	1019	5.5
11	0.5	No	1228	3.1
12	0.5	Yes	1233	6.0

The best results were reached with the material having 0.5 weigh% CNT concentration – it reached tensile strength of 1245 MPa and elongation of 6.5 %. This tensile strength is more than a 20 % improvement compared to the best batch with base material (no CNT) which accordingly reached tensile strength of 1035 MPa and elongation of 7 %. It should be noted that results indicate that a presence of CNT improves maximum tensile strength, but does not provide much improvement over elasticity because average elongation is still around 3 % for non-heat-treated material and 6 % for heat-treated material.

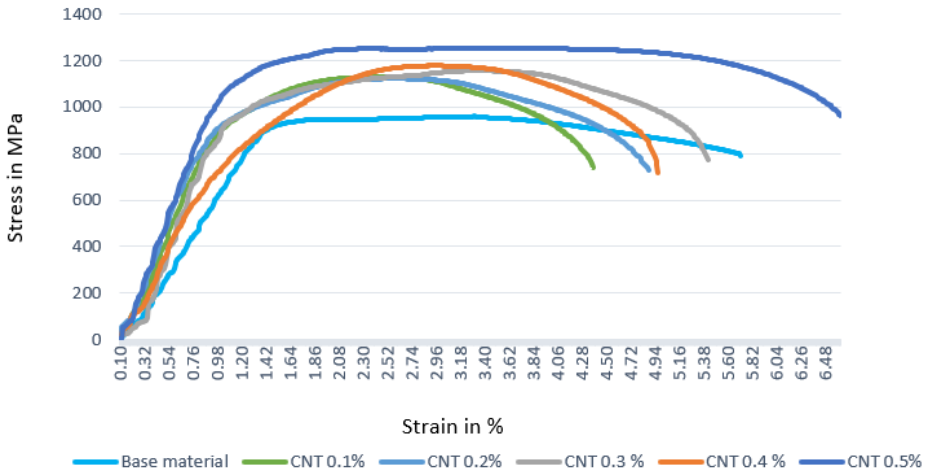

Fig. 6. Graphics of average tensile strength results.

3. CHALLENGES WITH MATERIAL DISTRIBUTION IN A METAL 3D PRINTER

Aurora Labs 3D printer utilises a powder bed fusion-laser proces and powder delivery is provided with three extruders. Extruders extract powder from three hoopers and by argon flow powder is injected on the build platform. When concentration of CNT was increased above 0.6 weight%, there were problems with powder extrusion through the powder extrusion pipes. To solve this problem, argon flow was increased from 10 to 20 l/min. When CNT concentration was increased above 0.5 weight%, it was observed that it was almost impossible to evenly distribute a layer of composite powder. Carbon nanotubes started to stick out from the composite powder layer and the recoater blade left traces with lines in the powder layer (see Fig. 7a). Additional upgrade was done for the recoater arm to improve powder layer quality and CNT compacting. Original rectangular silicon rubber was changed to a rounded triangle form which did not scrape out so much CNTs from metal powder (see Fig. 7b and c). Schematic representation of an uneven powder layer with CNT concentrations higher than 0.5 weight% is illustrated in Fig. 8. This also created a problem that in the next layer recoater arm hitched on CNTs and a powder pocket was created behind the carbon nanotube. Sometimes it created porosity because there was no material, but in some cases powder fell into this pocket after 2 or 3 layers, which increased a layer thickness in this spot to a level which was much higher than it was possible to properly melt with pre-set laser power. This led to high scrap percentage and we had to produce samples without support structures and with added material which was later removed by machining. This was the only solution to successfully produce samples without surface defects.

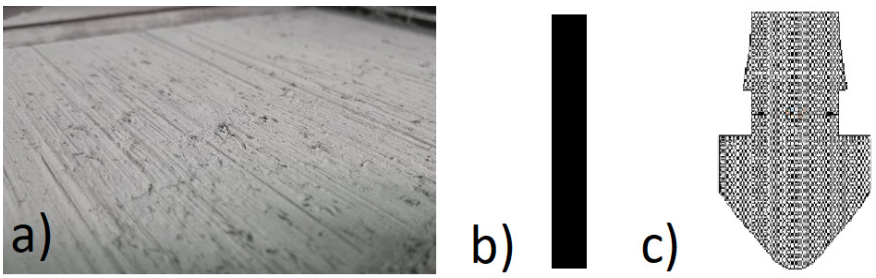

Fig. 7. a) Rough recoated layer with CNT concentration higher than 0.5 weight%, b) cross-section of standard rectangular form silicone rubber of recoater arm, and c) cross-section of rounded triangle form silicone rubber of recoater arm.

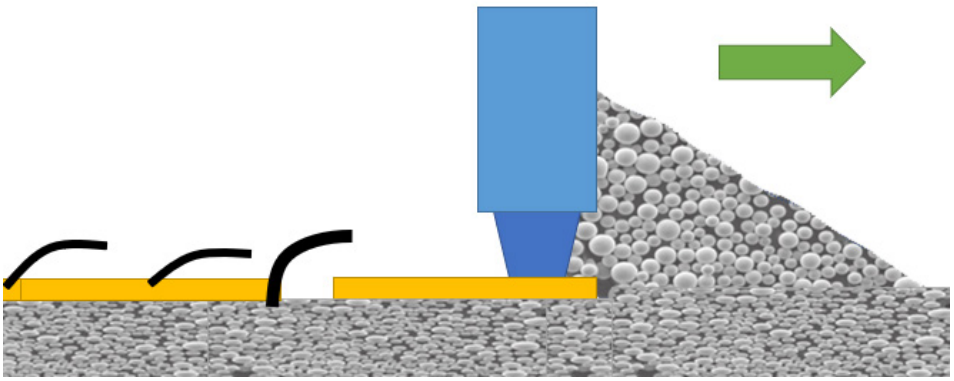

Fig. 8. Schematic representation of an uneven powder layer with CNT concentrations higher than 0.5 weight%.

Experiments also showed that it was challenging to maintain stable mechanical properties through entire batch of printed specimens. Due to non-cosistent recoating, a certain amount of printed specimens was not suitable for further tests – tensile strength testings. Figure 9 illustrates a typical defect – delayering of printed layers. This defect was especially evident when printing specimens having CNT concentration above 0.5 weight%. Visual control of specimens allowed concluding that a surface quality of printed composites was decreased compared to non-CNT printed specimens.

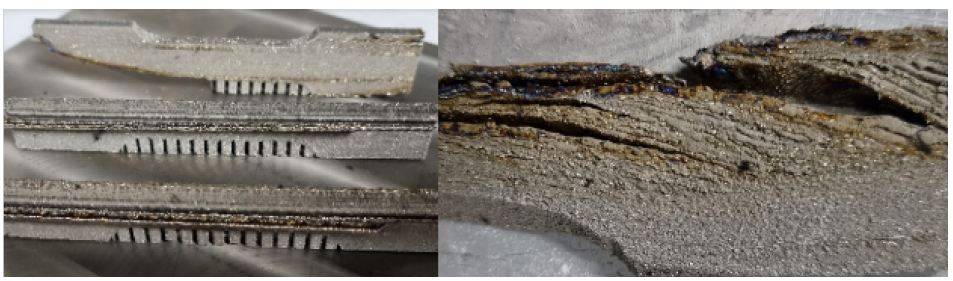

Fig. 9. Defects with layering for a composite with high CNT concentrations.

4. CONCLUSIONS AND FURTHER RESEARCH

The aim of the research was to improve Ti-6Al-4V base material mechanical properties by adding carbon nanotube (CNT) additives. Results indicated very promising improvements – a tensile strength was increased by 20 %. In the best case, the batch of specimens with pure Ti-6Al-4V material reached a tensile strength of 1050 MPa, but Ti-6Al-4V mixed with 0.5 weight% CNTs reached tensile strength of 1250 MPa. The aim of the research was achieved; however, newly designed material – Ti-6Al-4V-CNT composite – could be problematic to use in the metal additive manufacturing process, especially in the 3D printers utilising a powder bed fusion. Experiments also showed that it was challenging to maintain stable mechanical properties through the entire batch of printed specimens, as well as surface quality was decreased compared to non-CNT printed materials. Composite material research should be continued with additional experiments on the powder recoater arm to find a more suitable powder distribution process for the new composite material, which could improve the repeatability of the results and exploit new material full potential.

ACKNOWLEDGEMENTS

The research has been developed within Project 1.1.1.1/19/A/058 "Development and Testing of New Additive Manufacturing Material" using the ERAF foundation.

REFERENCES

1. Baudana, G., Biamino, S., Ugues, D., Lombardi, M., Fino, P. Pavese, (2016). *Metal Powder Report, 193-199.*
2. Y. Hao, S. Li, R. Yang (2016*). Effects of Rare Metals*, (35)
3. M.F.F.A. Hamidi, W.S.W. Harun, M. Samykano, S.A.C. Ghani, Z. Ghazalli, F. Ahmad (2017). *A review of powder additive manufacturing processes formetallic biomaterials (C78)*
4. N. Soro, et.al. (2019). *Investigation of the structure and me- chanical properties of additively manufactured Ti−6Al−4V biomedical scaffolds designed with a schwartz primitive unit-cell*, (A 745),195–202.
5. S. Ehtemam-Haghighi, et.al. (2019). *Microstructure, phase composition and mechanical properties of new, low cost Ti−Mn−Nb alloys for biomedical applications, J. Alloy. Comp,* (787, 570-577)
6. Donachie MJ (2000). *Titanium: a technical guide. 2nd ed. Materials Park, OH: ASM International*
7. Cui C, Hu B, Zhao L, Liu S (2011). Titanium alloy production technology, market prospects and industry development, (32), 1684–91
8. Karolina Karolewska, et.al. (2020*). Strength analysis of Ti6Al4V titanium alloy produced by the use of additive manufacturing method under static load conditions, Journal of Materials Research and Technology*, (Volume 9, Issue 2), 1365-1379
9. Lütjering G, Williams JC. (2007). *Titanium. 2nd ed. New York: Springer*
10. Uhlmann E, Kersting R, Klein TB, Cruz MF, Borille AV. (2015). *Additive manufacturing of titanium alloy for aircraft components. Procedia Cirp* (35), 55–60

11. Huang R, Riddle M, Graziano D, Warren J, Das S, Nimbalkar S, et al. (2016). *Energy and emissions saving potential of additive manufacturing: the case of lightweight aircraft components. J Clean Prod* (135:1559), 70
12. I.Campbell, D.Bourell,I.Gibson (2012). *Additive manufacturing: rapid prototyping comes of age, Rapid Prototyp*, (18), 255–258
13. I. Gibson, D.W. Rosen, B. Stucker (2014). *Additive Manufacturing Technologies, Springer*
14. M. Attaran (2017*). The rise of 3-D printing: the advantages of additive manufacturing over traditional manufacturing*. *Business Horizons*, (60), 677–688
15. B.Berman, (2012). *3-Dprinting:the new industrial revolution, Business Horizons,* (55), 155–162
16. S.H.Huang,P.Liu,A.Mokasdar,L.Hou (2013). *Additive manufacturing and its societal impact: a literature review, Int. J. Adv. Manuf. Technol*, (67), 1191–1203.
17. D.W.Rosen (2016). *A review of synthesis methods for additive manufacturing, VirtualPhys. Prototyp.* (11), 305–317.
18. L.E. Murr, S.M. Gaytan, D.A. Ramirez, E. Martinez, J. Hernandez, K.N. Amato, P.W. Shindo, F.R. Medina, R.B. Wicker, Metal fabrication by additive manufacturing using laser and electron beam melting technologies, J. Mater. Sci. Technol. 28 (2012) 1–14.
19. W.E. Frazier (2014), *Metal additive manufacturing: a review, J. Mater. Eng. Perform.*, (23), 1917–1928
20. S.L.Sing,J.An,W.Y.Yeong,F.E.Wiria (2016). *Laser and electron-beam powder-bed additive manufacturing of metallic implants: a review on processes, materials and designs, J. Orthop. Res.*, (34), 369–385
21. J.J. Lewandowski, M. Seifi (2016). *Metal additive manufacturing: a review of mechanical properties, Annu. Rev. Mater. Res.,* (46), 151–186
22. W.Harun, M.Kamariah, N.Muhamad, S.Ghani, F.Ahmad, Z.Mohamed (2018*). A review of powder additive manufacturing processes for metallic biomaterials, Powder Technol,* (327), 128–151
23. Y. Zhang, L. Wu, X. Guo, S. Kane, Y. Deng, Y.-G. Jung, J.-H. Lee, J. Zhang (2018). *Additive manufacturing of metallic materials: a review, J. Mater. Eng. Perform*., (27), 1–13
24. Muhammad D. Hayatb, Harshpreet Singhb, Zhen Hea, Peng Cao. (2019), *Titanium metal matrix composites: An overview. Composites Part A*, (121), 418–438
25. Dongdong Gu, Xiangwei Rao, Donghua Dai, Chenglong Ma, Lixia Xi, Kaijie Lin (2019). *Laser additive manufacturing of carbon nanotubes (CNTs) reinforced aluminum matrix nanocomposites: Processing optimization, microstructure evolution and mechanical properties, Additive Manufacturing*, (Volume 29)
26. Robyn L. Bradford-Viala, Fred Herman (2018). *Additive Manufacturing of Carbon Nanotube Metal matrix Composites, NAVAIR Public Release 2017-848, Army Research Lab Public Release, SHERPA, Inc.*
27. Jan Frostevarg, Stephanie Robertson, Vicente Benavides, Alexander Soldatov (2017). *Embedding carbon fibre structures in metal matrixes for additive manufacturing. Physics Procedia 89*, 39 – 48
28. Prashantha Kumar HG, Anthony Xavior M. (2018). *Processing of Graphene/CNT-Metal Powder. Powder Technology, Edited by Alberto Adriano Cavalheiro, IntechOpen*
29. *Sandvik Datasheet Osprey® Ti-6Al-4V Powder for additive manufacturing* [https://www.metalpowder.sandvik/siteassets/metal-powder/datasheets/osprey-ti-6al-4v-grade-5-and-grade-23.pdf]
30. A.Vevers, A.Kromanis (2022). *TECHNOLOGICAL ASSURANCE OF Ti-6Al-4V PARTS PRODUCED BY ADDITIVE MANUFACTURING USING SELECTIVE METAL LASER SINTERING. Latvian Journal of Sciences*

sciendo

LATVIAN JOURNAL OF PHYSICS
AND TECHNICAL SCIENCES
2023, N 6

DOI: 10.2478/lpts-2023-0040

NUMERICAL MODELLING OF A TURBINE FLOW METER USED AS PART OF THE HYDROGEN COMPRESSOR SYSTEM

S. Orlova[1*], T. N. Devdas[1], V. P. K. Vasudev[1], S. Upnere[2]

[1]Institute of Physical Energetics,
14, Dzerbenes Str., Riga, LV-1006, LATVIA
[2]Institute of Mechanics and Mechanical Engineering,
Riga Technical University
6B, Kipsala Str., Riga, LV-1048 LATVIA
*e-mail: sorlova@edi.lv

This study analyses a turbine flow meter in the context of a hydrogen compressor system. Basic concepts of turbine flow meter, accuracy and linearity, as well as calibration are described. Physical experimental testing scheme is presented in the paper. The viscosity of the fluid is one of the major factors that affects the performance of turbine flow meters. Numerical modelling experiments for different fluids with different viscosities are performed. Performed numerical modelling experiments give a possibility to continue research into the hydrogen compression system.

Keywords: *Calibration, CFD modelling, linearity, turbine flow meter, viscosity.*

1. INTRODUCTION

The need for an accurate and cost-effective liquid flow rate metering method is increasing every day, especially when it is necessary to estimate the cost of a certain amount of liquid or gas transferred through a pipeline. Industrial technological processes require flow measurement for the needs of the process control. Certain flow rates are required for optimum performance of the equipment. Therefore, accurate flow rate measurement is very important for industrial processes. There are two main ways to measure the flow: by volume and by weight. Liquids can be measured either in terms of weight or volume velocity, e.g., tonnes per hour, kilograms per minute, litres per hour, litres per minute, cubic meters per hour, etc.

In this study, a flow meter is considered as an integral part of the hydrogen com-

pression system. The system is patented and consists of hydrogen hydraulic compressors, where liquid and gaseous media are simultaneously supplied to the working chamber [1]. In this system, hydrogen is compressed by supplying a pressure fluid to a hydrogen cylinder. The use of a flow meter in this system provides the ability to control the level of hydrogen compression, enhancing the performance and reliability of the hydraulic hydrogen compression set.

A hydrogen compressor system is used to compress hydrogen gas to a higher pressure for storage or transportation. Hydrogen compressors are typically used in applications such as hydrogen fuelling stations, chemical processing plants, and hydrogen-powered vehicles. The compression process can involve one or more stages, using either positive displacement or dynamic compressors. The choice of compressor type and system configuration depends on various factors such as the required flow rate, inlet pressure, outlet pressure, and discharge temperature. The hydrogen compressor system may also include components such as intercoolers, aftercoolers, filters, and pressure regulators to ensure safe and efficient operation.

There are three main types of speed flow or rate meters:

- Flow meters using a propeller or turbine mounted in the flow space, the rotation speed being the measure of the flow rate. The main flow meters in this category are as follows: Turbine, Propeller and Pelton wheel flow meters.
- Flow meters with the flow rate indication derived from the measurement of a pressure drop across a reduction in the flow area: Pressure Drop flow meters.
- Flow meters using more recent measuring concept such as: Ultrasonic; Electro-magnetic; Vortex shedding, Fluidic; and Swirl flow meter [2].

Different types of flow meters and their characteristics are presented in Table 1.

Table 1. Types of Flow Meters

Type of flowmeter	Flow range [l/min]	Accuracy	Maximum pressure [kg/m^2]	Temperature range
Turbine	–2700000	0.25 %	4535	-240 °C to +1380 °C
Magnetic	0.2–1900000	1 %	1644	-240 °C to +177 °C
Ultrasonic	0.2–75000	1 %	1360	-200 °C to +200 °C
Orifice - fixed	0–1900000	1 %	2721	-40 °C to +400 °C
Orifice - variable	150–1500	1 %	2721	-200 °C to +500 °C
Positive displacement	0.1–12000	0.25 %	653	-40 °C to +250 °C

The choice of the flow meter for a particular application will depend on the physical-chemical nature of the fluid, the pipe diameter and levels of pressure and temperature of the fluid, whose flow rate is to be measured. For our study purposes, a turbine flow meter was selected. As the main concern is the process pressure, the obvious choice among all the types of meters is the turbine flow meter, as it has the highest maximum pressure value. Applicable measurement standards and recommendations are stated by the International Organization of Legal Metrology [3] and the European Association of National Metrology Institutes [4].

2. THEORETICAL BACKGROUND

The first turbine flow meter was invented in 1790 by Reinhard Woltman. The turbine flow meter is reliable for use with both liquids and gases. A turbine flow meter is constructed with a rotor and blades that use the mechanical energy of the fluid to rotate the rotor in the flow stream. The turbine flow meter design is presented in Fig. 1. Blades on the rotor are angled to transform the energy of the flow stream into rotational energy. The rotor shaft spins on bearings: when the fluid moves faster, the rotor spins proportionally faster. A turbine flow meter rotor with a pick-up sensor is presented in Fig. 2. Rotor movement is often detected magnetically when movement of the rotor generates pulsation. When the fluid moves faster, more pulses are generated. Turbine flow meter sensors detecting the pulse are typically located externally to the flowing stream to avoid material of construction constraints that would result if wetted sensors were used. The RPM of the turbine wheel is directly proportional to the mean flow velocity within the tube diameter and corresponds to the wide range of the volume flow. A flow transmitter processes the pulse signal to determine the flow of the fluid. The flow transmitter and sensing systems are available to sense the flow in both forward and reverse flow directions.

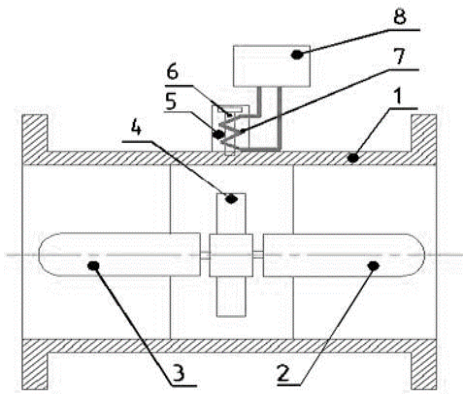

Fig. 1. Turbine flow meter design: 1 – body; 2 – upstream flow conditioner; 3 – downstream flow conditioner; 4 – rotor; 5 – magnetic induction sensor; 6 – core; 7 – coil.

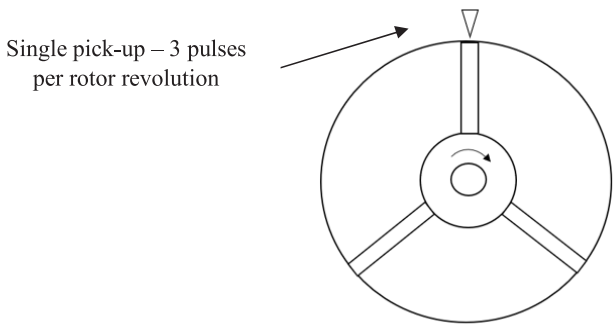

Fig. 2. Turbine flow meter rotor with a pick-up sensor.

The K-factor is used to describe the performance of meters to output of which is the form of electrical pulses (1):

$$K = \frac{n}{V_t}, \quad (1)$$

where n is a number of pulses per unit time. V_t is the volume passed in that time.

Advantages of turbine flow meters are the following:

- Wide flow range, including low flow rates.
- Good accuracy. For liquids it is usually ±0.25 %~±0.5 %, for gas turbine flow it is mostly ±1.5 %. Turbine flow meters are relatively high accuracy flow meters compared to other types of meters.
- Simple and durable construction.
- Easy installation and maintenance.
- Flexible connection to flow instruments for flow control.
- Wide range of operational temperature and pressure.
- Low pressure drops in the turbine.
- Convenient signal output.

Disadvantages of turbine flow meters are the following:

- Constant back pressure is required to prevent cavitation.
- Accuracy is adversely affected by liquid bubbles.
- Can only be used for measuring clean liquids and gases (a filtering screen may be required upstream the flow to prevent the damage caused by particles and inclusions).
- Not applicable for measuring corrosive liquids.
- A turbulent flow (constant fluid velocity throughout the complete pipe diameter) is required for measurement accuracy.
- Affected by changes in fluid viscosity.
- A straight pipe upstream and downstream the turbine meter is required to allow for dissipation of vortex paths in the flow.
- May not work accurately with high viscosity fluids if the flow pattern is laminar.
- The performance of a small size meter (2 inch or less) is critically affected by physical properties, and it is difficult to improve the flow meter capacity for a small size sensor.
- A turbine flow meter cannot retain its original calibration for a very long time as it will gradually change owing to surface wear or presence of dirt, requiring periodic recalibration to maintain high accuracy.

When the fluid passes through the turbine flow sensor rotor, it begins to spin due to the applied force. Simultaneously, there are certain opposing forces acting on the rotor. The turbine flow meter performance equation in stable condition is the following:

$$T_d - T_b - T_h - T_m - T_t - T_w = J\frac{d\omega}{dt} = 0, \quad (2)$$

where T_d is the rotor driving torque, T_b is journal bearing retarding torque, T_h is rotor hub retarding torque due to fluid drag, T_m is retarding torque due to mechanical friction in journal bearings and attractive force of magnetoelectricity detector, T_t is blade tip clearance drag torque, T_w both hub disk retarding torque due to fluid drag; T_r is a sum of drag torques; J is rotational inertia of the rotational system; ω is the turn speed of the rotor. The torques acting on the rotor of the turbine flow sensor are depicted in Fig. 3.

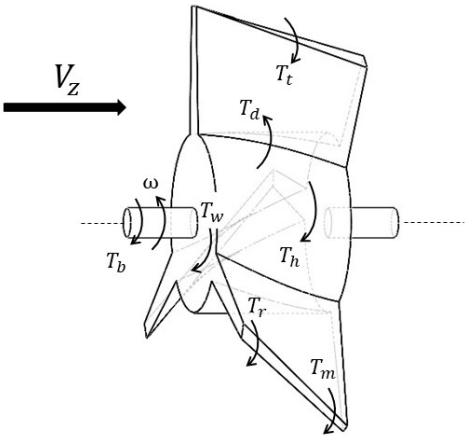

Fig. 3. Conceptual representation of the forces acting on the rotor (V_z is a direction of the axial velocity component).

The viscosity of the fluid is one of the major factors that affects the performance of turbine flow meters. For fluids with low viscosity (water: 1 mm2/s and below), the meter response is linearly dependent on the flow rate. However, for fluids with high viscosity (hydraulic fluid: 50 mm2/s to 100 mm2/s) the meter response is highly nonlinear [5]. The coefficient of viscosity, usually termed as viscosity, is a figure that indicates the amount of resistance a particular fluid offers to a shearing force under a laminar flow condition.

There are studies that analyse a viscosity effect on turbine flowmeter performance based on experiments and CFD simulation [5]–[8]. In research [5], results demonstrated that increasing viscosity led to a reduced meter factor and a rise in a linearity error. This is attributed to changes in wake flow and pressure distributions on the rotor blades, as detailed in CFD simulations. Similarly, the research outlined in [6] underscored viscosity influence on the turbine flow sensor, particularly affecting the impeller inlet velocity profile and fluid leakage. Through strategies like modifying the sensor hub radius in relation to the housing inner radius and fine-tuning impeller length, the study achieved enhanced accuracy across diverse viscosity levels. This optimization brought down the discrepancy in the average meter factor between the extremes of viscosity from 22 % to a mere 2.2 %. Additionally, the newly introduced performance metric demonstrated a marked improvement from values exceeding 20 % to figures below 5 %. Further research indicates that the impeller blade shape of DN10 turbine flow sensor, defined by the structural parameter η (incorporating aspects like the blade axial length and the blade tip axial length), is a key determinant of fluid dynamics, wake flow patterns, velocity distribution, and, in turn, the sensor overarching performance. To elevate a sensor efficacy, modifications in the rotor architecture, contour, and dimensions are pivotal. Specific studies [9]–[13] have focused on rotor optimization, pinpointing essential geometric facets of the rotor, such as blade count, blade tip radius, rotor hub radius, helical blade lead, blade thickness, blade bevel edge angle, and rotor hub length, as critical contributors to flow meter performance. Comparative evaluations between CFD simulations and empirical results, as cited in [14], [15], suggest a close correlation, endorsing the feasibility of predicting turbine flow meter efficiency via simulations.

The accuracy of turbine flow meter is expressed in terms of linearity and repeatability. The linearity is calculated as follows (3):

$$\delta_1 = \frac{K_{Max}-K}{K} \cdot 100\%, K = \frac{K_{Max}+K_{Min}}{2}, K_{Max} = Max\{K_i\}, K_{Min} = Min\{K_i\}. \quad (3)$$

Thus, K_{Max} and K_{Min} are crucial parameters when evaluating sensor performance indicators. Previous research [2] indicates that the highest meter factor K_{Max} emerges at peak flow rates, while the lowest meter factor K_{Min} is seen at the lowest flow rates, especially at elevated viscosities. Therefore, to enhance the sensor efficiency across a broad viscosity spectrum, the meter factor at low flow rates should be raised, or the meter factor at high flow rates should be lowered.

Repeatability is the flow meter ability to give exactly the same output when measuring exactly the same flow rate. The output of some flow meters drifted with time, after a period of operation it would still give good repeatability but about in different point.

Repeatability (4) is calculated as follows:

$$\delta_2 = MAX\left[\frac{1}{K_i}\left[\frac{1}{n-1}\sum_{j=1}^{n}(K_{ij}-K_i)^2\right]^{1/2}\cdot 100\%\right]. \quad (4)$$

3. METER STRUCTURE AND GEOMETRICAL PARAMETERS

For the numerical and physical experiment in a laboratory, water as working liquid was used. The object of investigation is a turbine flow meter KF500 used for the precise measurement of instantaneous flow rates and flow equities of low-viscosity fluids. It can be widely used in the fields of industry, metallurgy, scientific research for measuring or control. Several output parameters and other options can be applied, the device is completed with instantaneous flow rate and totalizer. Technical features of KF500 are presented in Table 2.

Table 2. Turbine Flow Meter Technical Parameters

Parameter	Value
Measure range	0.01 to 800 m3/h
Accuracy	±1% in measure scale 1:10 & ±2% in measure scale 1:25
Temperature	20 to 100 °C (Medium) / -25 to 55 °C (Environment)
Body material	Stainless Steel
Wetted part material	Alloy Steel
Power supply	-24 V DC
Output signal	4–20mA and pulse output

Figure 4 illustrates the structure and key geometric dimensions of the turbine flow sensor. The sensor is equipped with both upstream and downstream flow conditioners. The conditioners, located on both ends of the sensor, ensure that the fluid flow is uniform and conditioned before it interacts with the rotor. The rotor, being the central component, has blades that respond to the fluid flow, and its dimensions are critical to the sensor performance.

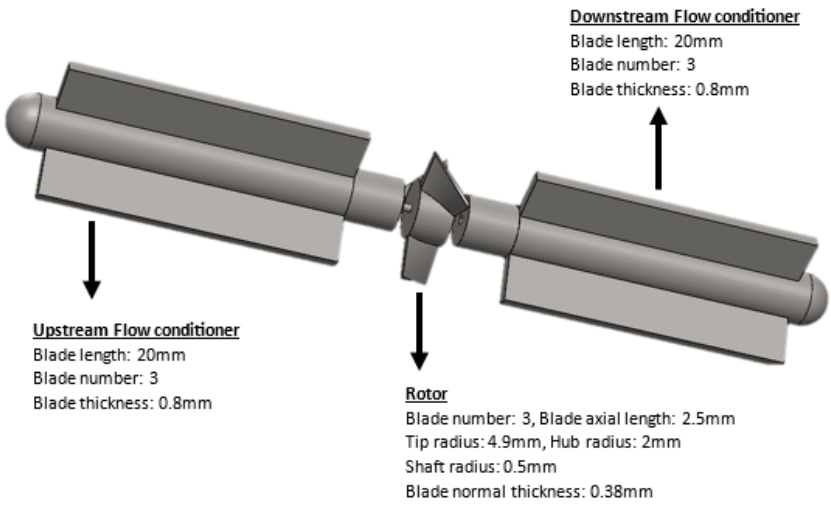

Fig. 4. The internal structure of a turbine flow meter.

4. NUMERICAL EXPERIMENT OF A TURBINE FLOW METER

The three-dimensional model of the DN10 rotor flow meter is constructed with the ANSYS Design Modeller function within the ANSYS Workbench platform. The dimensions were maintained with a high level of accuracy in accordance with the physical model. To ensure a more accurate representation of real-world conditions, straight pipes located upstream and downstream of the flow meter were extended by a length equivalent to 2.5 times their diameter in the simulation. The model was subsequently partitioned into three components, with the rotating region situated in the central portion and the surrounding portions positioned in the anterior and posterior sections, respectively.

The experiment involved the removal of the flow conditioner and blades using a Boolean command. This resulted in the division of the regions into three parts: a spinning region containing the turbine cavity, and a surrounding area containing the conditioner cavity. This approach has the potential to decrease the duration of the simulation process. The tetrahedron mesh method is employed in the procedure to enhance the quality of the mesh. The computational domain was partitioned into three distinct regions: the upstream straight pipe and flow conditioner, the rotor region, and the downstream straight pipe and flow conditioner. Ensuring that the skewness of the model remains below 0.9 is done in order to improve the quality of the results.

The simulation was conducted using the ANSYS Fluent software. The turbulence model was chosen for this study. The standard k-ω model was derived from the Wilcox k-ω model, with modifications made to account for low Reynolds number, compressibility, and shear flow propagation. In contrast to the traditional k-ω model, the SST k-ω model exhibits superior accuracy and algorithmic stability in the vicinity of the wall, as well as enhanced accuracy and credibility throughout a broader range of flow fields. The turbulence model chosen for this investigation was the SST k-ω model because of the low Reynolds num-

ber exhibited by the fluid flow in the pipeline. In the initial experiment, water was employed as the working fluid; however, for subsequent trials, a low-viscosity silicone oil was utilized. The cells that rotate and surround were allocated with their corresponding working fluid. The inlet boundary condition was specified as a velocity inlet, whereas the output boundary condition was specified as a pressure outlet. This study employed a passive method, specifically the 6DOF model and dynamic mesh, to simulate the internal flow field of the turbine flow sensor. This approach was chosen based on the operating principle of the turbine flow sensor. The simulation was initiated using a hybrid method, employing a straightforward approach. The simulation was executed for a duration of 10 seconds. The resolution of the grid was vital for the simulation effectiveness.

The integrity of the grid cells profoundly influences the rate of convergence and the precision of the simulation. An example of grid resolutions is depicted in Fig. 5, aimed at ensuring the grid quality and minimizing the model grid count. The method used for meshing was Tetrahedrons with size of 0.4 mm for the whole body and 0.3mm for rotor walls. The number of nodes was 81115 and that of the elements was 368134. The maximum skewness was 0.88. Inflation was provided on the rotating region for better simulation.

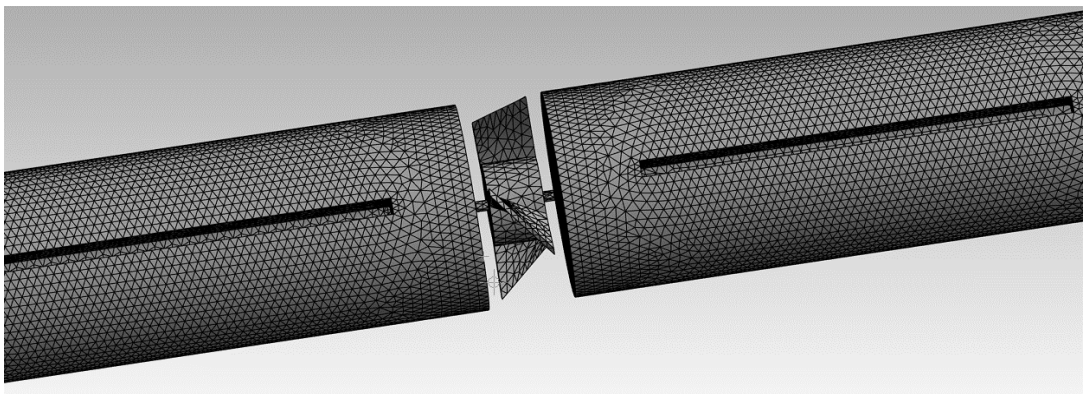

Fig. 5. An informative visualization of the grid structure used in the simulation model of a turbine flow sensor.

5. NUMERICAL SIMULATION RESULTS & DISCUSSION

During the testing process, water was the medium used. Specific flow rates were employed for this testing, including 0.2 m3/h, 0.3 m3/h, 0.48 m3/h, 0.84 m3/h, to evaluate the performance of the flow meter under these conditions. The variation of angular velocity with time for average fluid velocity of 0.54 m/s is shown in Fig. 6. Initially, ω ascends swiftly and then enters a phase of periodic fluctuation upon attaining a particular value. It is inferred that the impeller achieves consistent rotational motion at this juncture. The fluctuation in ω is predominantly attributed to the angle at which the liquid strikes the blade. The mean velocity, ω, is determined by averaging the spinning speeds recorded at each time increment within a complete cycle.

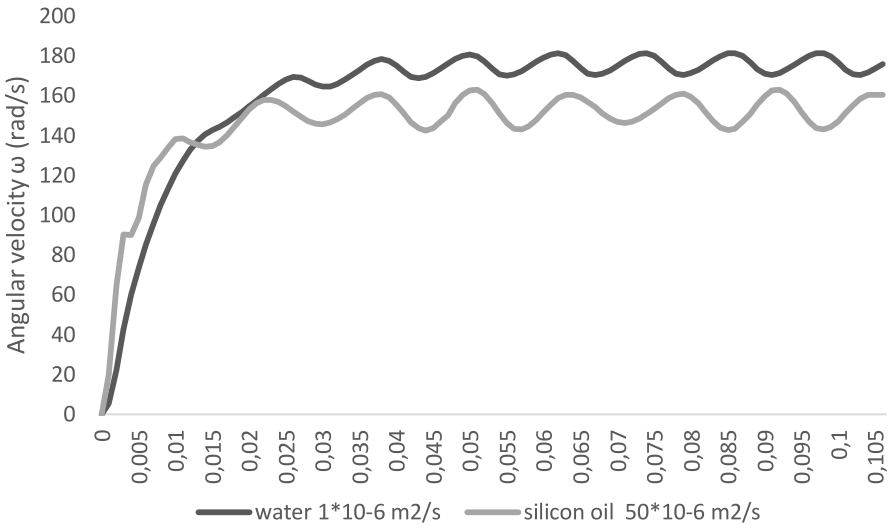

Fig. 6. The change in the angular velocity with time for average velocity of fluid equals to 0.54 m/s.

The primary goal of simulation was to study the turbine response to fluids of varying viscosities. The turbine angular velocity was evaluated as it interacted with these fluids. In the simulation, it was noted that with an increase in viscosity, the torque also increased, which was consistent with the principles of hydrodynamics. This increase in torque due to higher viscosity directly affected the angular velocity of the turbine. Specifically, for a given input power, a higher torque would mean a reduced angular velocity. Therefore, as the viscosity of the fluid increases, the turbine angular velocity tends to decrease, unless additional power is supplied to counteract the increased drag and maintain the same rotational speed. Viscosity defines a fluid ability to resist deformation. In the context of the simulation, fluids with higher viscosity show greater internal resistance, complicating the movement of fluid layers over one another. When the fluid passes through the turbine blades, this increased resistance results in heightened aerodynamic drag on the blades, leading to an increased torque on the turbine. This drag is a key factor in the observed changes in angular velocity.

Using water as our reference measurement, it is evident that as viscosity increases, the torque exerted on the turbine surface also increases. Consequently, the angular velocity of the turbine is affected. Based on our prior observations, variations in viscosity lead to differing rotational speeds of the turbine, thereby influencing the K-Factor of the turbine.

Figure 7 represents the relationship between flow rate and meter factor for two different fluids: water and silicon oil.

The shape of the curve depends on the viscosity of the liquid which varies with temperature and from liquid to liquid, as well as on the flow range over which the flow meter is used. The turbine can be designed that is less sensitive to one of those two factors. This can be done by varying the tip clearance of the impeller, by correct design of the rotor blades or by altering the hub/rotor ration. The effect of increasing the tip clearance is twofold, it frees the rotor from the high drag area at the tips, and also places the rotor in the region of higher velocity.

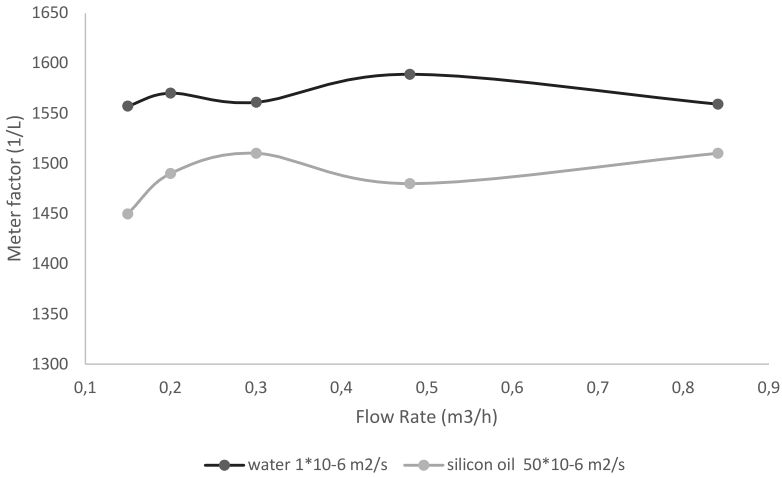

Fig. 7. Comparison of meter factor vs. flow rate for water and silicon oil.

The meter factor K varies across different viscosity levels, Fig. 8 showcases the relationship between K factor and the kinematic viscosity of the fluid for average velocity of fluid being equal to 0.54 m/s. It is evident from the graph that as the viscosity rises, the meter factor K consistently drops throughout the entire range of viscosities.

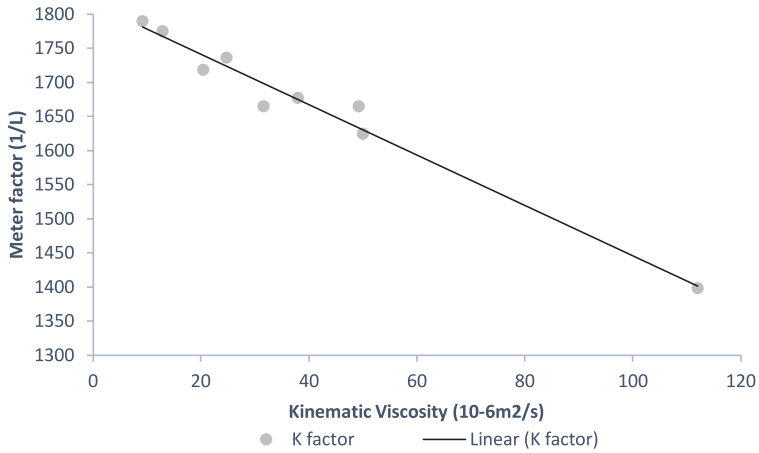

Fig. 8. Viscosity effect on K factor of turbine flow meter.

Viscosity greatly impacts the performance of turbine flow meters. High-viscosity fluids create more drag on turbine blades, requiring more torque for rotation. They also present a pronounced laminar flow profile, reducing effective flow velocity. Additionally, viscous fluids can increase start-up torque due to greater resistance to initial movement, affect bearing friction, and alter the meter operational flow range. Thus, fluid viscosity is a crucial factor in the design and calibration of turbine flow meters for accurate measurements. Flow velocity distribution between the rotor blades is shown in Fig. 9.

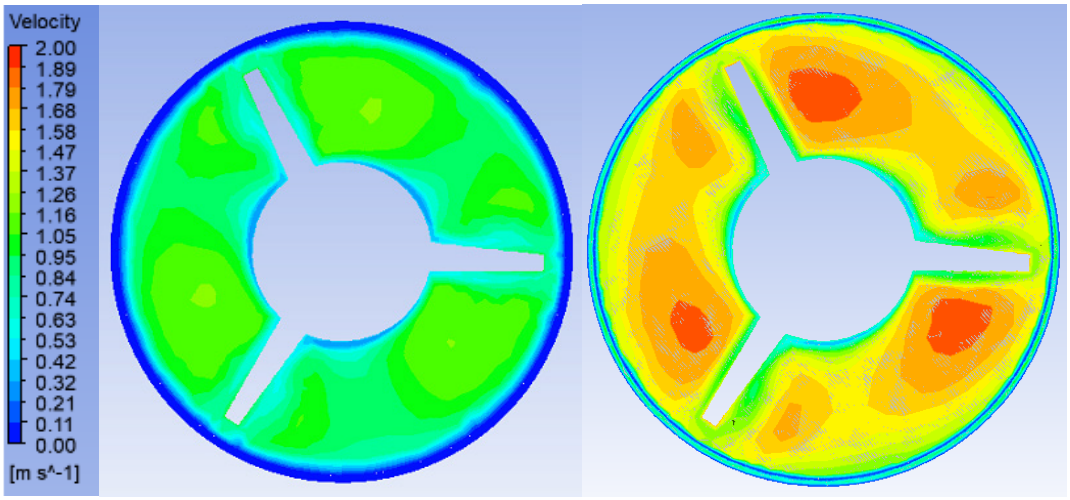

Fig. 9. Flow velocity distribution at the rotor inlet for water:
on the left – a flow rate of 0.2 m^3/h;
on the right – a flow rate of 0.84 m^3/h.

As accuracy of flow metering is important, turbine flow meters should be calibrated using exactly the same fluids which are to be measured. The calibration should also be carried out using the same upstream and downstream pipework as would be used in a particular installation. It means that calibration has to be carried out on site using a meter prover. To calibrate means to standardize (as a measuring instrument) by determining the deviation from a standard so as to determine the proper correction factors. There are two key elements to this definition: determining the deviation from a standard and ascertaining the proper correction factors. The calibration of the flow meters needs to be carried out on a regular basis. The procedure can be performed by using another calibrated meter as a reference or by applying a known flow rate. The accuracy can vary over the range of the instrument and with temperature and specific weight changes in the fluid, so all these factors have to be considered. Thus, the meter should be calibrated over temperature as well as over the range, so that the appropriate corrections can be made to the readings. A turbine meter should be calibrated at the same kinematic viscosity at which it will be operated when in service.

The laboratory provers generally operate with a gravimetric calibration system. They can apply water/oil as the operational fluid. The gravimetric method is the weight method, where the flow of liquid through the meter being calibrated is diverted into a vessel that can be weighed either continuously or after a predetermined time.

The weight is usually measured with the help of load cells. The weight of the liquid is then compared with the registered reading of the flow meter being calibrated. Volumetric method is a technique, where a flow of liquid through the meter being calibrated is diverted into a tank of known volume. The time to displace the known volume is recorded to get the volumetric flow rate, e.g., gallons per minute. This flow rate can then be compared to the turbine flow meter readings.

6. EXPERIMENTAL EVALUATION

A controlled physical experiment was carried out in a laboratory setting to study the behaviour of a turbine flow meter when used with water at a working temperature of 20 °C. For the study purposes, a physical experiment diagram was developed (Fig. 10), and the process algorithm was described (Table 3).

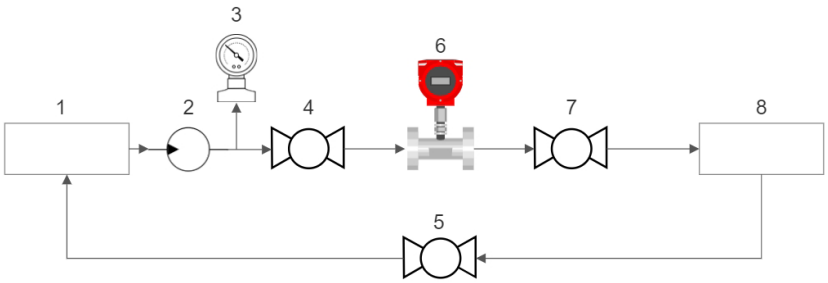

Fig. 10. The diagram of the experiment involving the pump: Closed inlet tank (1), pump (2), manometer (3), isolating ball valve (4), bypass ball valve (5), flow meter (6), flow regulation ball valve (7), outlet tank (8).

Table 3. The Experiment Process Algorithm

Number	Action
1	The liquid is poured into the inlet tank, the volume/mass of the liquid is recorded
2	Valves 5, 4, 7 are shut
3	Pump activation, waiting for the operational pressure on the manometer (3)
4	Opening of valves 4, 7
5	Liquid transfer from tank 1 to tank 8
6	Recording of the meter readings upon completion of the liquid transfer
7	Shutting of valves 4,7
8	Liquid volume/mass metering in tank 8
9	Recording and comparison of the meter readings and actual measurement figures, correction of the operation of the metering system
10	Opening of bypass valve 5, pump 2 activates the back flow
11	Transfer of the liquid into the inlet tank to check for steady state readings

Table 4 presents a side-by-side comparison of simulation and experimental results focusing on the average meter factor and linearity error.

Table 4. Comparison of Experimental and Simulation Results

Simulation		Experiment		Error, %
Average meter factor	Linearity error, %	Average meter factor	Linearity error, %	
1573	0.01	1555.86	0.0089	1.09

The simulation predicted an average meter factor of 1573, while the experimental result was 1555.86, a minor deviation of 1.09 %. Additionally, both methods exhibited incredibly low linearity errors, with the physical experiment being slightly

more consistent at 0.0089 % compared to 0.01% achieved in the simulation. Overall, the simulation closely mirrored the experimental results, demonstrating its reliability and precision.

7. CONCLUSIONS

The study outlined in this document provides a comprehensive investigation into the performance characteristics of a DN10 rotor flow meter using ANSYS simulation tools and subsequent physical experimental validation. The meticulous construction of the three-dimensional model and the subsequent partitioning into distinct components allowed for the evaluation of the flow meter behaviour under various conditions, including alterations in fluid viscosity and flow rates. The use of the SST k-ω turbulence model and the dynamic mesh technique for simulating the internal flow field of the turbine flow sensor have been proven to be effective approaches, as evidenced by the close correlation between simulation and experimental results.

The investigation underscored the considerable influence of fluid viscosity on the performance of turbine flow meters. It was observed that as viscosity increased, there was a notable decrease in the turbine angular velocity due to the increased drag force.

In the comparison between water and silicone oil, it becomes apparent that the fluid kinematic viscosity plays a pivotal role in determining the meter factor (K), with a higher viscosity correlating to a decreased K-factor. This can have significant implications for industrial processes where precise flow measurements are essential for optimal operation.

Moreover, the experimental evaluation of the flow meter performance through a carefully designed laboratory setup provided tangible evidence that supported the accuracy of the numerical simulations. The slight discrepancies observed between the experimental data and the simulated results, in terms of the average meter factor and linearity error, fall within an acceptable range that validates the simulation model efficacy. The negligible error percentage of 1.09 % in the average meter factor is indicative of an exceptionally reliable simulation process.

ACKNOWLEDGEMENT

The study has been financed by ERDF project "Experimental Studies and Development of Technology on Hydraulic Compression of Hydrogen" No 1.1.1.1/20/A/185. We acknowledge Riga Technical University's HPC Centre for providing access to their computing infrastructure.

REFERENCES

1. Bezrukovs, V., Bezrukovs, Vl., Bezrukovs, D., Konuhova, M., & Berzins, A. (2022). *Hydrogen Hydraulic Compression Device*. LVP2022000071, 31.08.2022.
2. Benard, Ing C. J. (1988). *Handbook of fluid flowmetering* (1st ed.). UK: Trade & Technical Press.

3. International Organization of Legal Metrology. (n.d.). *OIML Website*. Available at https://www.oiml.org
4. European Association of National Metrology Institutes. (n.d.) *Metrology for Regulation Event.* Available at https://www.euramet.org
5. Guo, S., Sun, L., Zhang, T., Yang, W., & Yang, Z. (2013). Analysis of Viscosity Effect on Turbine Flowmeter Performance Based on Experiments and CFD Simulations. *Flow Meas. Instrum., 34,* 42–52. doi: 10.1016/j.flowmeasinst.2013.07.016.
6. Tegtmeier, C. (2015). *CFD Analysis of Viscosity Effects on Turbine Flow Meter Performance and Calibration.* Master Thesis, University of Tennessee. https://trace.tennessee.edu/utk_gradthes/3415
7. Ruiz, V., Pereira, M.T., & Taira, N.M. (2013). Turbine flowmeter and viscosity effects of liquid hydrocarbons. In *16th Int. Flow Meas. Conf. 2013*, *FLOMEKO 2013*, (pp. 479–483).
8. Guo, S., Yang, Z., Wang, F., Zhao, N., & Li, X. (2021). Optimal Design of Wide Viscosity Range Turbine Flow Sensor Based on Flow Field Analysis. *Flow Meas. Instrum., 79*, 101909. doi: 10.1016/j.flowmeasinst.2021.101909.
9. Guo, S., Wang, S., Zheng, X., Zhao, N., Fang, L., & Li, X. (2019). Optimization of turbine flow sensor structure based on the velocity distribution inlet. In *I2MTC 2019 – 2019 IEEE Int. Instrum. Meas. Technol. Conf. Proc*. doi: 10.1109/I2MTC.2019.8827083.
10. Wang, Z., & Zhang, T. (2010). Optimization of geometric parameters of the rotor in the turbine flowmeter. In *15th Int. Flow Meas. Conf. 2010, FLOMEKO 2010,* (pp. 896–906).
11. Ren, Z., Zhou, W., & Li, D. (2022). Response and Flow Characteristics of a Dual-Rotor Turbine Flowmeter. *Flow Meas. Instrum., 83*, 102120. doi: 10.1016/j.flowmeasinst.2022.102120.
12. Lijun, S., Zhaoying, Z., & Tao, Z. (2007). Quantitative Optimization Method for Rotor Geometric Parameters of Liquid Turbine Flow Sensor. *Chin. J. Sci. Instrum., 28* (3), 493.
13. Saboohi, Z., Sorkhkhah, S., & Shakeri, H. (2015). Developing a Model for Prediction of Helical Turbine Flowmeter Performance Using CFD. *Flow Meas. Instrum., 42*, 47–57.
14. Lavante, E.V., Kettner, T., & Lazaroski, N. (2003). Numerical simulation of unsteady three-dimensional flow fields in a turbine flowmeter. In *Proceedings of the International Conference on Flow Measurement*. 12–14 May 2003, Groningen, the Netherlands.
15. Lavante, E.V., Banaszak, U., & Kettner, T. (2004). Numerical simulation of Reynolds number effects in a turbine flowmeter. In *Proceedings of the International Conference on Flow Measurement*, (pp. 575–582). Guilin, Chine.